Towards Inert Cores for Investment Casting

by

Martin Riley

A thesis submitted to the University of Birmingham
for the degree of Master of Research in Chemical Engineering Science

School of Chemical Engineering

University of Birmingham

Edgbaston

Abstract

Improvements in material technology allow gas turbines to be run at ever increasing temperatures and speeds. As a consequence, blades in the high pressure part of the turbine are subject to an extremely high level of oxidative attack. These blades are cast from specialized alloys in ceramic moulds which employ internal ceramic cores. One way in which the blades can be made more resistant to corrosion is by the inclusion of low levels of reactive metal elements such as yttrium and lanthanum in the blade alloy. During casting these reactive elements are easily lost from the alloy by reaction with both the core and shell of the mould.

This study tests several candidate core formulations for their ability to retain reactive element levels in the alloy after casting, and also explores the mechanisms of reactive element depletion. Through scanning electron microscope studies, a layer of reaction products from the oxidation of the reactive elements was found at the metal-ceramic interface after a simulated casting procedure. The thickness of this layer was found to correlate with the free energy of formation of the ceramic used, in that using a thermodynamically less stable ceramic led to the formation of a thicker layer and thus greater depletion of reactive elements. Electron dispersive X-ray spectroscopy (EDS) confirmed this result by finding lower levels of reactive elements in metal samples heated with less stable ceramics. The use of yttria (Y_2O_3) in the core materials was found to increase the retention of reactive elements in CMSX-4.

Acknowledgements

Thanks to my supervisor Stuart Blackburn for all his patient encouragement, support and hard work in getting me through the course. Thanks also to my co-supervisor Nick Green for his amazing knowledge of single-crystal castings, and repeatedly baffling me with thermodynamics; Chen Yuan for her experimental advice and helping me find my feet; Peter in the foundry, for running an unreasonable number of samples for me; and the lab technicians Jaswinder Singh, John Wedderburn and Katy Lewis, for continued use of my fingers.

Personal thanks to all the people named above and everyone in my group for making this year a thoroughly pleasant experience; the Lunchtime Club in Chem Eng for some much-needed unscientific conversation; and anyone else I've moaned at during the course. Special thanks to my sponsors, the EPSRC and to Richard Greenwood for his rash decision to let me come here in the first place.

Table of Contents

List of Figures

List of Tables

1. Introduction

1.1 Scope of the project

The upper physical limit on the efficiency and performance of a gas turbine is decided by its maximum operating temperature[1]. Turbine entry temperatures above 1650 °C are now achievable due to three main technologies: advanced alloys with high melting temperatures, the use of hollow, air-cooled blades, and thermal barrier coatings (TBC) which allow the surface temperature of the blade to be significantly higher than the melting point of the blade metal. The hot, high pressure air entering the turbine causes a large oxidative stress on the blades, so as many measures as possible must be taken to prevent oxidation and increase the lifetime of the blades. The addition of reactive rare earth metals such as yttrium, lanthanum and hafnium to the blade alloy increases the oxidation resistance of the metal and improves adhesion of the TBC[2]. A problem with the use of these reactive elements (RE) is that they are lost during the investment casting process used for blade manufacture, for example only 5% of added yttrium is retained in a cast blade using standard silica mould technology[3].

The ceramic moulds used to cast the blades consist of an outer shell and an internal core (see section 1.7) which creates a hollow space in the blade through which air can be passed for cooling during operation. The presence of a core in the mould has been shown to exacerbate reactive element loss on casting and to cause an uneven distribution of Y/La in the blade[4]. It is expected that the chemical composition of the cores used will affect the retention of Y and La in the blade alloy after casting.

This project assesses the suitability of several candidate formulations for use in the next generation of cores. It also investigates the interactions between core and metal and attempts to understand the reaction thermodynamics and kinetics. The effect of mould composition on the casting process, and indeed the nature of high-temperature interfacial interactions between metals and oxide ceramics, is a ripe area for research with very little data available and, to the author's knowledge, no widely accepted model which fully explains the nature of these interactions exists, although Ellingham diagrams[5] and other classical thermodynamic methods can be used as a first approximation.

1.2 Controlling La/Y loss

An alloy containing 6 ppm sulphur requires an addition of 30 ppm yttrium[6]. The ultimate aim of research would be to accurately reach this concentration during casting while limiting the initial quantities of reactive elements used. Minimising the use of yttrium and lanthanum is environmentally and economically beneficial as these are relatively rare[7] and expensive[8] metals (see Fig. 1).

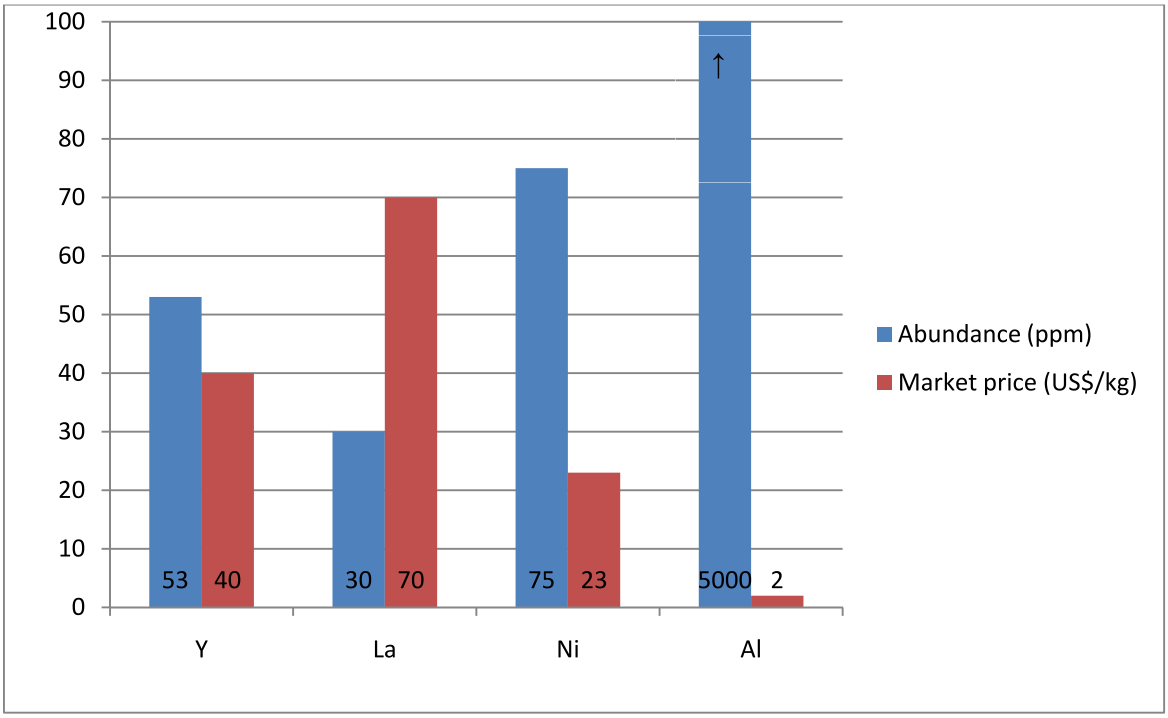

Figure 1: Crustal abundance and price of selected metals

At the moment the reactive elements are added in excess, so that the required amounts are left after casting. This method is wasteful and difficult to control.

Lowering the sulphur concentration in the alloy decreases the quantity of reactive elements needed. To this end superalloys are produced with the lowest possible sulphur content. For instance, CMSX-4 with <2 ppm sulphur[9] has been available since the start of the century and alloys are now being produced containing <1 ppm sulphur[10]. Lowering the sulphur content further using techniques such as hydrogen annealing is not economical.

Changing the chemical composition of the mould used in casting should have an effect on the quantities of Y and La lost, as it is believed that much of the loss is due to reaction with, or diffusion into the mould. It is the purpose of this thesis to investigate the effect of different ceramic compositions on the casting behaviour of RE additions.

1.3 Gas Turbines

1.31 How a jet engine works

Fig. 2 is a diagram of a typical gas turbine. The first stage is the compressor (shown in red), which increases the pressure of air entering the engine. The pressurised air is combined with fuel and burnt in the combustion chamber. The energy released in this reaction drives a turbine (shown in blue), which in turn drives the compressor pushing more air into the engine. Energy can be gathered from the engine in three ways: thrust from the exhaust air, torque from the shaft and, in the case of a turbofan engine, thrust from air bypassed over the rest of the engine by an oversized inlet fan.

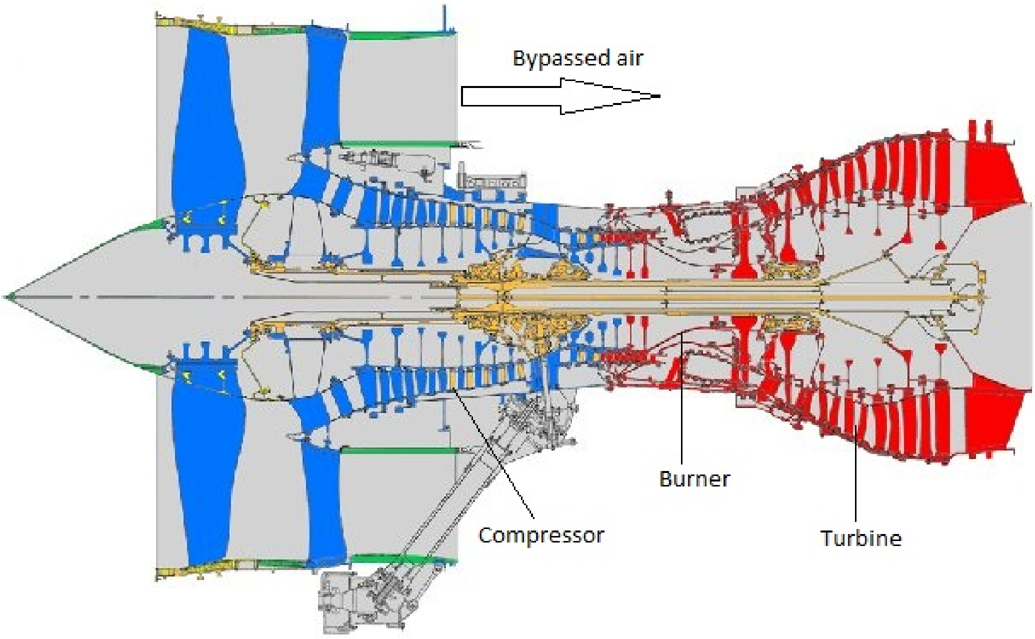

Figure 2: Cross-section of a turbofan engine. From Rolls-Royce PLC

1.32 Problems associated with the hot zone

The blades in the hottest part of the turbine (see Fig. 3), directly behind the combustion chamber, have to withstand the greatest stresses. These stresses take three forms: mechanical, thermal and chemical. The mechanical stresses are exacerbated by the high temperature so the blades must have excellent creep resistance, as well as resistance to thermal shock, brittle fracture and oxidation. The metallurgy of superalloys is designed to maximise these factors.

The turbine is cooled by passing air from the compressor through channels in the blades. This allows the engine to be run hotter than the melting point of the blade metal.

Figure 3: A typical high pressure turbine blade. The holes visible allow air to bleed from the hollow centre to the blade surface.

1.33 Methods to counter oxidation

The superalloys used to make turbine blades incorporate aluminium and chromium, both of which form layers of oxide scale on the surface of the blade metal, which protects the metal from further oxidation. The thermal barrier coating is an additional layer of oxide such as yttria-stabilised zirconia, which provides further protection against oxidation and also reduces conduction of heat into the blade metal.

The presence of yttrium and other reactive metals in the alloy increase the lifetime of blades both by increasing the oxidation resistance of the metal and improving adhesion to the thermal barrier coating.

1.4 Superalloys

The term "superalloy" refers to a group of alloys, first developed in the 1950s, with excellent creep properties and oxidation resistance close to their melting temperatures[11]. Superalloys have the best creep resistance of all metals above 800 °C, which makes them the material of choice for gas turbine blade applications. High temperature creep resistance is a primary requirement here since the blade must keep its aerodynamic shape at the highest possible operating temperature. Ceramics such as zirconia also exhibit excellent resistance to creep but are not used as the major component of turbine blades due to their susceptibility to brittle fracture. Superalloys are usually based on nickel and in addition contain ten or more alloying elements in various quantities. Cobalt-based superalloys also exist but are rarely used due to the high price of cobalt. Niobium based superalloys are in development[12] which could promote a leap to even higher operating temperatures.

1.41 History & development

The development of superalloys and of jet engines has been closely linked. Improvements in superalloy technology, along with the use of cooled blades and thermal barrier coatings, have helped to raise turbine entry temperatures by 700 °C in their 50 years of existence (see Fig. 4).

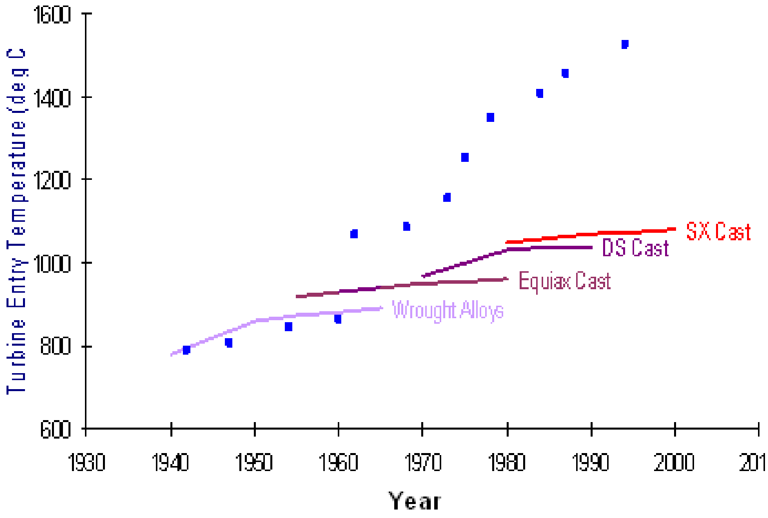

Figure 4: Increases in turbine entry temperature with new technology. The temperature jump 1960-1962 is due to the introduction of hollow blades.

Improvements in both alloy formulations and production technology have allowed great improvements in blade operating temperatures. The introduction of cast blades brought about an increase in blade life over the original wrought parts. Later, directionally solidified and single crystal castings allowed still greater blade lifetimes by the removal of grain boundaries. This in turn allowed improvements in alloy formulation by the removal of grain boundary strengthening agents such as boron and carbon. Later superalloys such as CMSX-4 include rhenium (Re) as a strengthening agent, with cutting-edge alloys increasing the Re content and also including ruthenium.

1.42 Roles of major elements

Nickel is used as the base of the alloy because it forms a stable face-centred cubic (FCC) structure from room temperature to its melting point, so during operation it will not undergo any phase transitions which would cause conformational and shape changes and might compromise the material properties. The FCC structure makes nickel both tough and ductile. Platinum group metals are also stable in this structure but their cost and density make them unsuitable for use.

The major phase present in Ni-based superalloys is the gamma (γ) phase which has the same FCC structure as pure nickel, but contains substitutions of elements with similar atomic radius such as cobalt, chromium, molybdenum and rhenium, which act to stabilise the phase. Present as a precipitate in this phase is the gamma-prime (γ') phase which acts to strengthen the alloy[13]. This has the formula Ni_3X, where X can be Al, Ti or Ta, and adopts the primitive cubic $L1_2$ structure. Carbide and boride phases may also be present if the alloy contains carbon or boron. These segregate to, and act to strengthen, grain boundaries. Their presence is therefore not required in single-crystal alloys such as CMSX-4.

1.43 CMSX-4

CMSX-4 is a 2nd generation single-crystal superalloy manufactured by the Cannon-Muskegon Co[14,15]. It has a solvus melting point of 1563-1593 K[16] and is used extensively by Rolls-Royce in their turbines. Standard CMSX-4[17] contains, by weight, 6.5 % chromium, 9 % cobalt, 0.6 % molybdenum, 6 % tungsten, 6.5 % tantalum, 3 % rhenium, 5.6 % aluminium, 1.0 % titanium and 0.1 % hafnium, the remainder being made up from nickel with traces of other elements.

1.5 Investment Casting

1.51 Basic process

Investment casting, or the lost-wax process, is one of the oldest manufacturing processes[18] and is still in use today as it allows the precise manufacture of very intricate metal pieces. The basic process involves either moulding or carving a wax pattern in the shape of the finished part. This pattern is then coated with clay or ceramic slurry. After some drying the wax is melted and poured out, then the mould is fired. Molten metal is poured into the mould. When this has cooled the mould is broken off leaving the casting, which may require some machining and/or hand-finishing.

A disadvantage of investment casting is that it is a one-time process which creates waste from spent moulds and wax, and is laborious with many stages to the process, and a total of three pieces (pattern, mould and casting) needing to be manufactured for the creation of one finished part.

1.52 Industrial process

The modern manufacturing process as it applies to turbine blades is mostly automated. Patterns are made by injection-moulding wax around ceramic cores, which give the shape of internal features in the final casting. The patterns are dipped by robot arm into a slurry composed of fine particles of ceramic precursor materials such as SiO_2, Al_2O_3 and $ZrSiO_4$ mixed with a binder system, followed by a stucco of coarser oxide particles. The hygroscopic stucco reduces drying stresses in the slurry[19]. The mould is dried and the process repeated several times to build up the mould in layers. A final coat of slurry is applied to seal the last layer of stucco in place. The piece is heated rapidly to a temperature above the wax melting point, usually in a steam autoclave, so the wax can be removed. Used wax can be reclaimed and used again. Normally reclaimed wax is used for the casting tree runners while only virgin wax is used for blades. The mould is heated again to a higher temperature to sinter the ceramic and burn out any remaining binder wax. Molten metal is poured into the mould. For nickel-based superalloys the casting temperature is around 1550 °C, and the process is carried out under high vacuum conditions to prevent oxidation of the alloy. When the metal has cooled and solidified the mould is broken off and the core removed by chemical leaching, usually with strong alkali.

Investment casting is used for blades because of the precision and finish achievable, because of the ease of use of cores, and the ability to directionally solidify the casting.

1.53 Directional Solidification and Single Crystal Castings

The process of directional solidification (DS) greatly improves the creep resistance of a superalloy by ensuring that all the grain boundaries are aligned longitudinally along the blade. This is achieved by cooling the cast part very slowly, starting at one end. The mould sits on a refrigerated plate which is withdrawn from the hot zone of the furnace at a rate of a few centimetres an hour, so that the solid/liquid interface moves along the length of the casting. This produces long, parallel crystals. Using certain alloys, monocrystalline (SX) castings can be produced via the same technique, which have the highest strength and creep resistance. This process involves the use of a “grain selector” or a seed crystal at the base of the casting which determines the direction of crystal growth.

1.6 Cores

1.61 Role of the core

Blades in the hot part of the turbine are internally cooled by allowing a bleed of relatively cold air from the compressor to flow in channels through the centre of the blade. These channels may run directly through the blade or, commonly in more modern engines, may run in a serpentine fashion to allow the cooling air to pick up more heat as it flows through the blade. The creation of this complex internal geometry requires the use of a core during casting. This is a piece of ceramic in the shape of the required internal channel (see Fig. 5) which sits in the mould during casting.

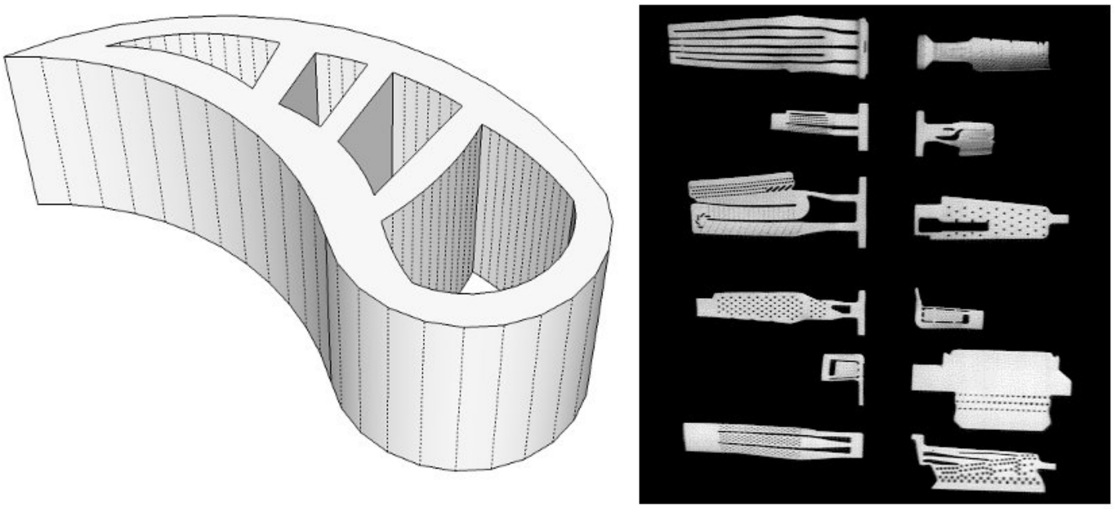

Figure 5: Cross-section of a typical blade (left) and typical core shapes (right)

One requirement of a good core material is that it will sinter well to have the required strength at the firing temperature, but become more fragile on cooling from the casting temperature, so the core can be removed more easily after casting. In silica cores this is induced by the α-β cristobalite phase transition[20]. Shape control on sintering is important, and this is facilitated by low shrinkage of the ceramic on firing. Other requirements are low thermal expansion coefficients which are even in all directions, enough mechanical strength in the green state to keep its shape before sintering, low reactivity with the casting metal, low cost and ability to be removed chemically after casting, preferably with as cheap and environmentally benign an agent as possible. For these reasons ceramics such as silica, zircon and alumina, or combinations of these, are commonly used. SiO_2 with additions of zircon or alumina is by far the most common.

1.62 Ceramic Injection Moulding

Cores of the complexity required in high-pressure turbine (HPT) blades are normally produced by ceramic injection moulding (CIM)[21], a process which allows complex part geometries to be economically and precisely mass-produced in a wide range of ceramic materials. CIM, also known as powder injection moulding (PIM) is a relatively modern technology, with much of the technology used adapted from polymer injection moulding. PIM techniques are also used with metal powders for the forming of alloy parts[22]. The process involves mixing a ceramic precursor powder with a binder system to form a feedstock of moderate apparent viscosity and high solids loading. This feedstock is then heated and pressurised into a mould or die of the required geometry. This geometry can include narrow sections and intricate shapes, but is limited by the need to remove the part from the die, which is usually of a two-part clamshell design, after injection. Currently methods are being developed which will allow these limitations to be exceeded[23], and these are expected to start to replace CIM industrially in a few years.

Forming ceramic components to close tolerances is challenging because parts can shrink by a factor of up to a third[24] during the drying and sintering process for a standard fully dense ceramic, which extenuates any defects in the green or unfired body and can also cause cracks and faults to appear. Cores generally shrink by under 5 % and a shrinkage factor of between 1-2 percent can be induced by formulation selection. While shrinkage can be limited by appropriate choice of powder, it is important to start with a green part of as near net shape as possible to minimise the effect of any shape changes on sintering. CIM has an advantage here over traditional ceramics forming methods such as slip casting and extrusion as the dimensions of the mould and green density can be closely controlled. Cores for investment casting are a major application of CIM. Other uses include the manufacture of spark plugs, turbocharger rotors and vanes. CIM could replace a great many ceramic forming processes, but the high price of dies limits its industrial uptake.

CIM feedstocks must be optimised for powder packing and thus density, apparent viscosity and green strength, as well as having the properties required after sintering. This requires optimisation of both the powder and binder system. For a non-porous material, the solids loading of the feedstock should be as high as possible, while preserving enough fluidity for injection at the moulding temperature.

Broad particle size distributions (PSDs) have been found to improve the mouldability and packing of powders[25]. A multimodal PSD is often used to fine-tune the powder properties. In this system several fractions, each of a narrow PSD, are combined to yield a powder containing a range of particle sizes, and often a range of particle morphologies. A fraction of fine particles is often included, which increases density as the small particles fill in gaps between larger particles, and also shortens sintering times due to the higher reactivity of small particles. Over-use of small particles, however, can cause problems with agglomeration and also give too much densification on sintering for core applications.

Binder systems have several related functions: to hold the powder together in the green state, to give the required viscosity during injection, to maintain an even dispersion of powder and avoid agglomeration and phase migration. In addition the binder must burn out evenly without creating deformations or faults in the part and have good fluidity when melted. The binder must also allow for the part to be removed from the mould without sticking.

Binder systems may either be based on polymers such as polyethylene, or organic waxes. Several components are usually combined to give the desired properties. Water soluble binders such as methylcellulose are used more rarely, which have the advantage of a shorter burn-out time, but can be tricky to use as they are gelled by heating and do not truly solidify before ejection.

High-shear mixing processes are considered to give the best flow characteristics when combining phases[26] as they break down agglomerates and encourage bonding between powder and binder. Vacuum mixing is often employed to remove any air in the feedstock, as gas expansion on heating can cause faults. After mixing, the feedstock is heated to the moulding temperature and injected. Injection can either be carried out by a plunger or a screw type device, similar to (or adapted from) a ram or screw extruder. Injection temperatures and pressures are very system dependent, but are often in the order of 100-120 °C and 50-80 MPa[27].

After injection of the feedstock, cooling and ejection of the injected part from the die, the binder must be removed from the system and the particles bonded together. These steps are most simply accomplished as a combined stage by thermal processing. Debinding is most effectively carried out at the lowest temperature feasible, as this allows fractions in the binder, which may vary considerably in volatility, to escape evenly without a build-up of vapour pressure leading to defects forming. Debinding times can range from several hours to several days[28]. After the binder has been removed the temperature is raised to allow the particles to sinter together. Sintering is a process by which solid particles can bond at a raised temperature below their melting points, the driving force for the process being the reduction of surface area. During the process particles move together, increasing density in the fired piece.

After sintering the completed part is inspected for defects and deformations, internally by X-ray projection and externally by laser measurement. Some machining may also be required before the core is ready for use, particularly to remove any moulding line flash and any flow channels which may have been incorporated to allow material to be injected smoothly into the mould but which are superfluous to the core's functionality.

1.7 Role of Y/La

Reactive metals such as yttrium, lanthanum and hafnium, when added to superalloys, have a marked effect on the lifetime of the alloy in use by increasing its resistance to oxidation[29,30]. It is thought that the "reactive element effect" works by improving adhesion of the protective oxide scale which forms on the outside of aluminium- and chromium-containing alloys. Although the mechanisms of the effect are not fully understood, according to Smialek[31], Smeggil[32] and others[33,34,35], a major contributor to the effect is the sequestering of sulphur by the reactive element, which traps sulphur in the matrix as compounds such as yttrium oxysulphide ($Y_2O_2S_2$). In the absence of reactive metal additions, sulphur has been shown to segregate to the boundary between metal and scale and decrease the interfacial adhesion, thus increasing the rate of scale spallation[36].

Yttrium and its oxides have also been shown to promote the formation of a continuous chromia scale in alloys which normally form weak or non-continuous scales[37].

1.8 Metal-Ceramic Interfaces

During casting a triple-phase boundary is formed between the solid ceramic, liquid metal and the furnace atmosphere. There are a variety of chemical interactions which can take place at a molecular level, including diffusion of the metal into the ceramic, ceramic elements into the metal, oxidation of the metal by the ceramic oxide, evaporation of the metal and reaction of the metal with the furnace atmosphere. Physical considerations include viscosity of the liquid metal and surface characteristics of the ceramic. Interactions of the metal with interfacial products of the reaction between ceramic and metal will also become important during the process.

The method used in this study is an adaptation of the sessile drop technique, as it is a simple way to study solid-liquid interactions. The sessile drop technique is commonly used to measure surface energies and works as follows:

A drop of a liquid of known surface tension is placed on a surface of the solid in question. The contact angle Θ between liquid and solid indicates the degree of wetting, as shown in Fig. 6.

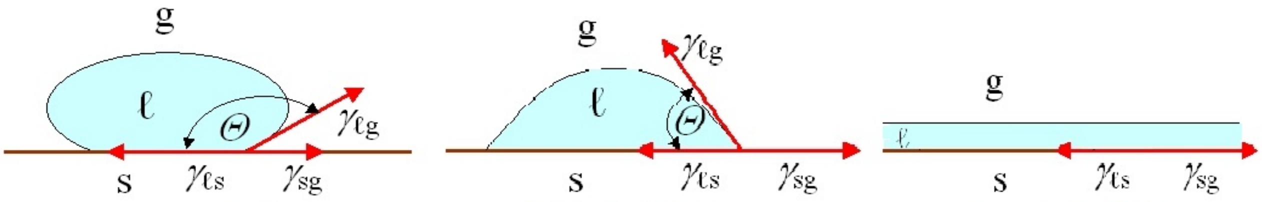

Non- wetting (Θ <90°)

Partial wetting (Θ >90°)

Complete wetting (Θ = 0°)

Figure 6: degrees of wetting defined by contact angle

For a pure liquid on a smooth surface of an inert solid, the surface energy can be calculated from the Young equation

$$\gamma_{SG} = \gamma_{SL} + \gamma_{LG}\cos\theta$$

(eqn. 1)

where γ_{XY} represents the surface energies between solid, liquid and gas. Roughness in the surface or impurities in the liquid cause deviation from the ideal behaviour described above, and surface adhesion will cause hysteresis in contact angle measurement depending on whether the drop is advancing or receding. High viscosity will tend to limit the spreading of a drop and thus give a higher value for contact angle than might be expected from the Young equation. CMSX-4 has a relatively low viscosity of 2 mPa.s at 1550 °C[38], around double that of water at 20 °C.

Reactive systems require a more detailed analysis, as there is a free energy change associated with the formation of reaction products which effectively changes the surface energy between solid and liquid. Once formed, these reaction products may remain as a tertiary phase between solid and liquid, towards which each of the other phases will have its own surface energy term. Reactive wetting is thus a very complex system, and several competing models are emerging to explain these types of metal-ceramic interfaces. Sinnott and Dickey[39] present a good review of thermodynamic and computational models based on atomistic theory for ideal, non-reactive systems and compare these to high resolution electron micrographs. A group led by Frage[40] has found that addition of titanium to various non-reactive metals improved their ability to wet a TiC substrate, which they attribute both to increased dissolution of the substrate in the liquid metal and to increased activity of the Ti-containing alloys. Surface energy was considered to have a negligible effect here. In their general review of reactive wetting, Kumar and Prabhu[41] note the much greater length of time that reactive systems take to reach their equilibrium contact angle than non-reactive systems due to the formation of a wettable reaction layer, and also the effects of surface roughness, heterogeneity in the substrate, and the effect of any atmosphere in the furnace, particularly if the atmosphere is reactive towards the liquid metal. They note several experiments in which the melting of solder in air led to reduced wetting compared to melting in an inert atmosphere, due to the formation of an oxide layer on the surface of the drop. Both this review and an excellent thesis by Arroyavé[42] call attention to a number of cases in which the addition of a more reactive element to an alloy increases its ability to wet a substrate; this effect is exploited in brazing applications.

Eustathopoulos[43,44,45] and his group have collected a great deal of data on the kinetics of wetting of ceramic and similar materials by liquid metals using the sessile drop technique under vacuum, similar conditions to those employed in the casting furnace. While they note that a consistent theoretical model is yet to be achieved, a trend can be drawn between the reactivity of a metal and its ability to wet a substrate as measured by contact angle, in that more reactive metals tend to exhibit increased wetting.

Thermodynamic studies[46] using Cu-Pd-Ti alloys on alumina and silica substrates of similar surface energies but differing reactivities found that the wetting behaviour depended much more on interfacial energies than on the reactivities of the substrates. However, the interfacial reaction layer formed was found to differ in thickness by an order of magnitude. Based on further studies[47] using CuSi alloy on reactive and non-reactive substrates, a high dependence of reaction rate on wetting was found. This was attributed to a system in which the metal does not initially wet the substrate, but reaction between metal and substrate forms an interfacial reaction layer which is wettable by the metal. The contact angle is thus decided by the degree of spreading of the reaction layer, rather than the theoretical surface energy between metal and substrate.

Valenza, Muolo and Passerone[48] have undertaken similar experiments using superalloys on several ceramic substrates, both analysing wetting behaviour and composition of the interface. In most of their metal-ceramic couples an equilibrium contact angle was reached shortly after melting and fragments of the substrate were found to adhere strongly to the metal drop after cooling. CMSX-486 (which is of a similar composition to CMSX-4 but with additions of hafnium and boron) gave contact angles of 81°and 84° with alumina and zirconia substrates. Similar values were found for the other substrates used. A reactive layer of hafnium oxide was found at the interfacial boundary. The group also note that the liquid drop moved erratically across the surface of the substrate, forming new solid-liquid interfaces continuously. This phenomenon was attributed to the changing morphology and surface energy of the interface as a reactive layer forms. A further reactive layer of alumina was found on the surface of CMSX-486 after melting with zirconia; this was attributed to preferential oxidation of aluminium in the alloy by oxygen present in the ceramic. Zirconia is known to be a good conductor of oxygen ions, a property which is often exploited in solid oxide fuel cells[49]. This property could give a kinetic driver for oxidation of aluminium by zirconia; there is no thermodynamic reason why zirconia should oxidise aluminium while alumina does not as their Gibbs free energies of formation are similar[50] (-380 and -382 kJ per mole O_2 respectively).

From this prior literature, it is clear that thermodynamics and kinetics of metal-ceramic interfaces are complex and not fully understood at this stage. However, a few common themes can be drawn. Wetting and reactivity are linked, at least for some binary and ternary alloy systems. The presence of a reactive layer at the interface is expected, which is likely to involve segregation to the surface of the more active elements in the alloy. The growth of this reaction layer will have an effect on interfacial energies and further reaction, and these effects will vary depending on the characteristics of the system in question.

For the purposes of this study, possible effects of reactive layer growth to consider will include the following:

Assuming that yttrium and lanthanum, by far the most reactive elements present in the alloy, will segregate to form the reactive layer (RL), and that this is a mechanism for the loss of these elements, a wider and thicker RL will be directly related to the amount of Y and La lost. A wider RL will give more surface area for mutual diffusion of ceramic and metal into each other, while a thicker layer is expected to lead to decreased diffusion. A wider reactive layer will give more available surface area for RL thickening. Viscous forces in the metal will affect the spreading characteristics of the drop, and also the rate at which reactive elements can migrate through the metal to react at the interface.

The kinetic factors affecting RL growth involve a mixture of chemical and physical drivers. Measurement of contact angle may or may not be a direct indicator of the progression of the reaction. Reactivity of the ceramic, surface characteristics of the substrate and morphology of the reactive layer as it grows are all expected to affect the reaction progress.

2. Methodologies

2.1 Substrate formulation

A range of ceramic materials, appropriate for use as cores and with varying chemical properties, were selected for analysis. An existing core formulation used in industry was required. For this purpose V200, a proprietary core material produced by Ross Ceramics and used extensively by Rolls-Royce in their castings, was selected. V200 is primarily silica (SiO_2) with minor additions of zircon and other materials.

Other formulations were chosen on the basis of reactivity and price. The relative thermodynamic stabilities[51] of metal oxides commonly used for ceramics are shown in Fig. 7. Lanthana is shown alongside as this is the expected reaction product from the reaction of lanthanum with the oxide of another metal.

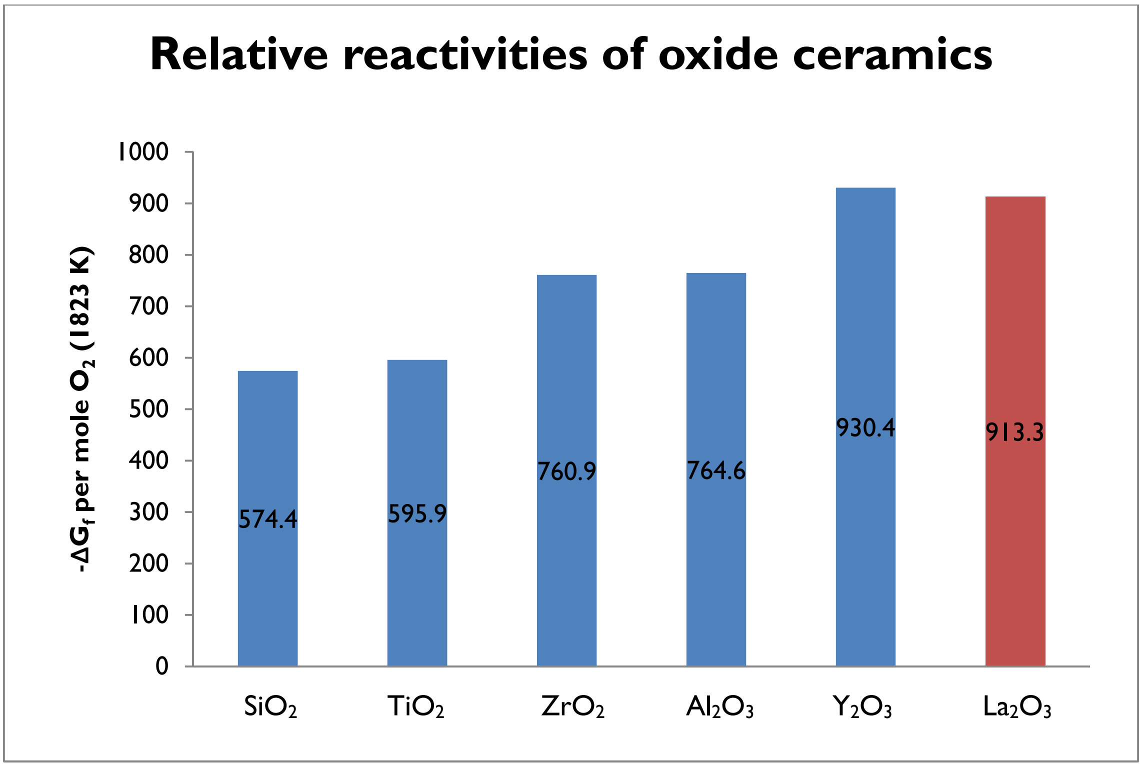

Figure 7: Gibbs energies of formation of metal oxides

Yttria (Y_2O_3) was chosen as it has the highest $-\Delta G_f$ per mole O_2 of all the oxides and so should be inert to reaction with any metal of equal or less reactivity than yttrium, i.e. all the elements in the alloy.

Alumina (Al_2O_3) was chosen as it has a $-\Delta G_f$ per mole O_2 in between those of silica and yttria. It was thought that not containing either of the metal elements being studied might have an effect. Alumina is also considerably cheaper than yttria, a consideration which would become important in an industrial context.

Finally an 80% alumina-20% yttria mix was prepared on the basis that this could have a similar low reactivity towards yttrium as pure Y_2O_3, but at a lower cost.

The powder systems used have all been previously developed and successfully injection moulded. The formulations used were as follows:

V200 – Supplied as a ready-formulated powder from Ross Ceramics

Yttria – Treibacher coarse yttria (125 – 180 μm) 70%

Treibacher 200 mesh yttria (<75 μm) 20%

Treibacher fine yttria (D_{50} = 2 μm) 10%

Alumina - Kumichal F230 Alumina ($D_{50} \approx 50$ μm) 70%

Kumichal F600 Alumina ($D_{50} \approx 25$ μm) 20%

Reactive alumina (<1 μm) 10%

Yttria/alumina - Kumichal F230 Alumina ($D_{50} \approx 50$ μm) 70%

Treibacher 200 mesh yttria (<75 μm) 20%

Reactive alumina (<1 μm) 10%

Particle size distributions for the formulations other than V200 are shown in Fig. 8.

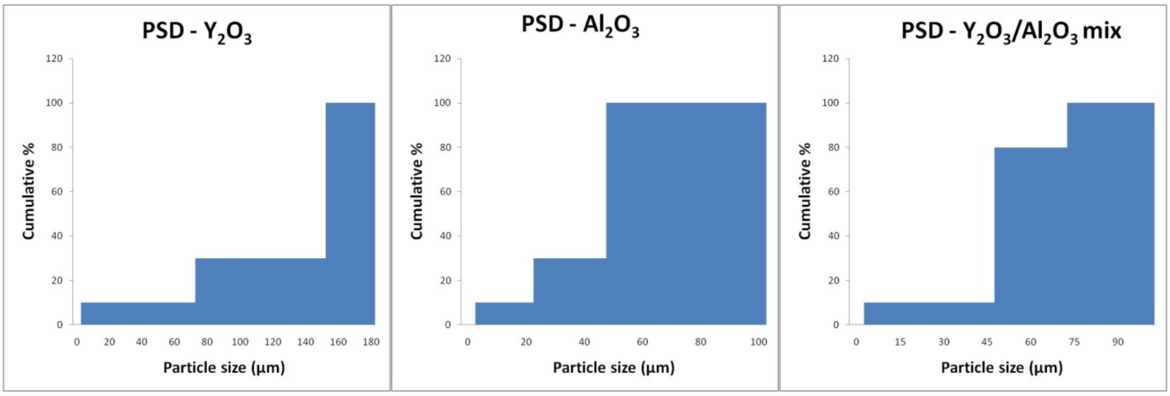

Figure 8: Particle size distributions

2.2 Substrate Preparation

The ceramic formulations were made into substrates for the experiment by dry powder pressing. This process is designed to give pieces with similar characteristics to injection moulded cores, but avoiding the complexity of the injection moulding process and without the need to create large batches of feedstock. It is expected that the dry pressing process will yield sintered parts of slightly lower density and greater porosity than injection moulding due to the lower pressure and lower shear involved. The process is also likely to yield pieces with marginally different surface characteristics to pieces formed by PIM.

A binder system was specially developed for pressing of the substrates (see section 3.1). The binder system used to prepare all the substrates used in the study consisted of 2% PEG-400, 2% PVA, 1% Dispex and 1% glycerol. Percentages were calculated using the mass of the powder as 100%. This will lead to different percentages of binder by volume between powders, however this factor was not of major importance in the preparation of successful substrates. Batches were prepared from 100g powder.

Substrates were required to have a flat surface large enough to support a drop of metal. To form the required geometry a uniaxial single acting press made by the University workshop was used, which yielded rectangular pieces measuring 40 mm x 20 mm x 3 mm.

To prepare the powder, the ceramic precursor particles were mixed with the binder system described above by hand, with 10 ml water added per 100 g powder to facilitate dispersal by creating an aqueous phase for mixing. The water was then evaporated at 70 °C and the resulting agglomerates pushed through a 600 μm sieve to yield a coarsely agglomerated powder. This powder was then placed in the die shown in Fig. 9 with a spatula and tapped to ensure even distribution, then the die was subjected to 700 KPa pressure in the press shown in Fig. 9. Pressures much lower than this did not compress the agglomerates enough to hold together, while higher pressures caused cracking of the green parts.

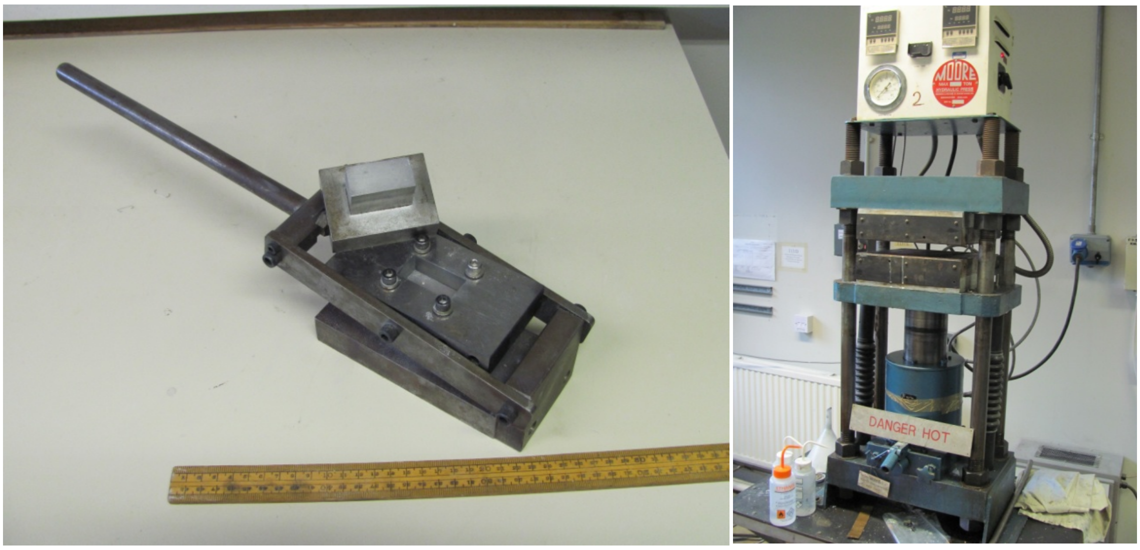

Figure 9: The die (left) and press (right) used in the experiments

The resulting pieces were then fired in air in a single-step debinding and sintering process according to the profile described in Fig. 10. This process was found adequate for the formation of thin parts within the tolerances required for use as a stable platform. The furnace used was a Lenton LTD 1700 ceramic box furnace.

A sintering temperature of 1550 °C (the same as the casting temperature) was chosen instead of the usual lower sintering temperature used in industry. This was done because, in the real casting process, some sintering of the mould occurs in the furnace as it is heated prior to the alloy being poured in.

Yttria was found not to sinter well at this temperature. Yttria sintering temperatures of over 2000 °C are common in industry[52]. The first few yttria samples fired were sintered at 1550 °C for 4 hours instead of the 1 hour process employed on the other materials; most of the yttria samples were fired at the maximum achievable temperature on the furnace used of 1700 °C for 1 hour. This temperature was not tested with the other formulations.

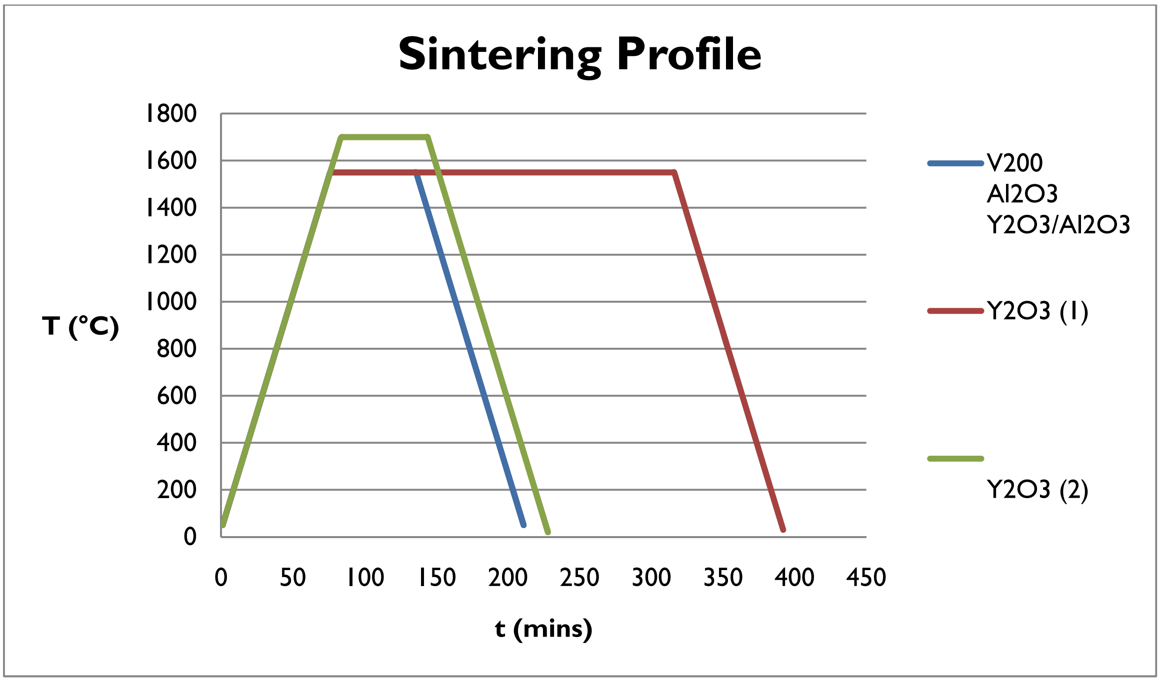

Figure 10: Temperature profiles for firing ceramics

2.3 Characterisation of substrates

2.31 X-Ray Tomography

The pressed substrates were compared to commercially injection moulded samples for internal structure and homogeneity by X-ray microtomography. This technique is similar to the computed tomography procedure used in medical imaging, but using smaller samples (on the millimetre scale) and harder X-rays to achieve higher resolution. X-ray projection images of a sample from are taken from multiple angles and, using an algorithm known as the Radon transform[53], compiled into a three-dimensional projection showing details of internal structure. Although X-ray microtomography has been shown to be as effective as mercury porosimetry in calculating porosity of samples when properly calibrated[54], a limitation of the technique is that manipulation of images can affect results. For instance, in the relatively homogeneous samples shown in Fig. 13, changing the contrast and threshold can drastically alter the observed pore size. The scans were carried out on a Skyscan 1072 machine with a resolution of 5 μm. The samples measured 5 mm x 5 mm x 2.5 mm, the source voltage used was 100 kV and the source current was 100 μA.

2.32 Density Measurement

Sections of the substrates were cut to a rectangular shape with a razor blade and their dimensions measured with a ruler. The mass of the sections was measured with a laboratory balance accurate to 0.001 g. Calculated volume was divided by mass to give the density of the sample, and this was divided by the composition's theoretical full density to give relative density.

2.4 Metal preparation

CMSX-4 superalloy doped with yttrium and lanthanum was cut into sections measuring 10 mm x 5 mm x 5 mm using a Struers Accutom-5 precision cutting machine and a silicon carbide cutting disc. Dimensions were chosen for the metal which, when melted, would form a drop which easily fits on the ceramic substrate. The alloy used contains 840 ppm Y and 870 ppm La. These are higher levels of the reactive element additions than those present in alloys for industrial use, to make the reactive elements easier to observe. Samples of pure yttrium were cut to similar dimensions by hand sawing, as the high speed of the cutting machine wheel caused the yttrium to overheat and oxidise.

2.5 Casting simulation

A Retech single crystal vacuum furnace (see Fig. 11) was used to melt the prepared metal drops on top of the substrates (Fig. 12). The furnace has a movable chilled ram below a hot zone maintained by a resistance heater. Under normal operation the casting metal is melted by an induction heater at the top of the furnace and poured into the heated mould; instead to keep the drop stable in this study each metal-ceramic couple was placed together on a ceramic stand on top of the ram and raised into the hot zone at 1550 °C for the required time. The Y and La doped CMSX-4 (henceforth referred to simply as CMSX-4) was melted on the V200, Al_2O_3, Y_2O_3 and Al_2O_3/Y_2O_3 substrates for 5, 15, 30 and 60 mins; yttrium was melted on V200 for 1, 5, 8, 10 and 12 mins.

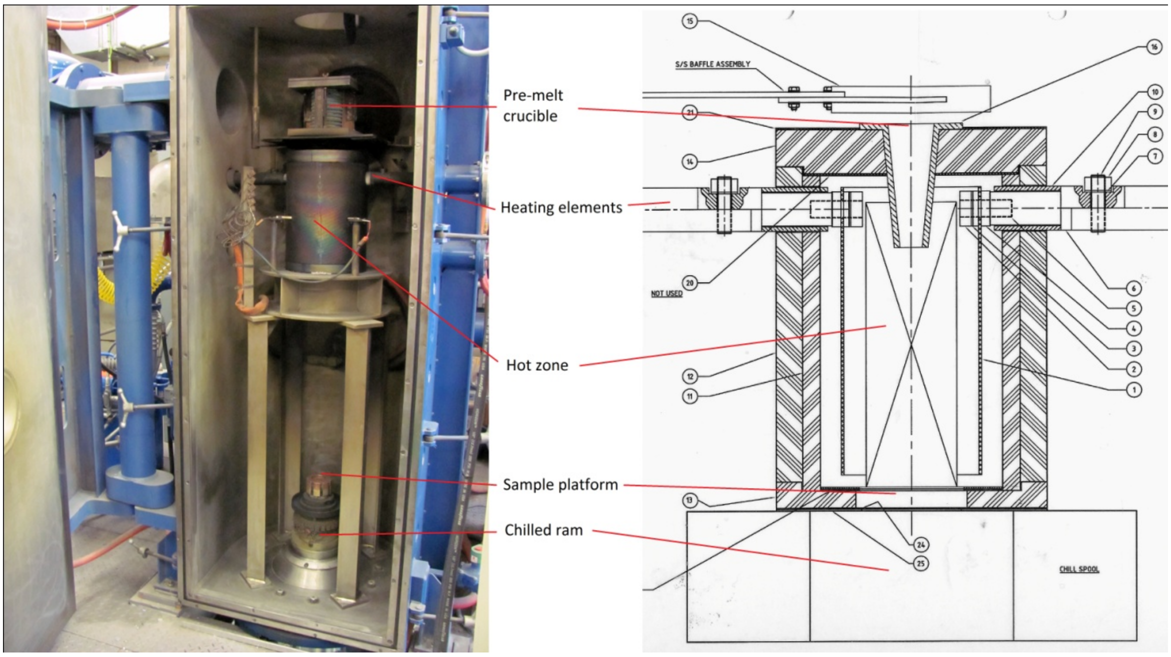

Figure 11: Photograph and diagram of the furnace used for melting the metal on the substrates

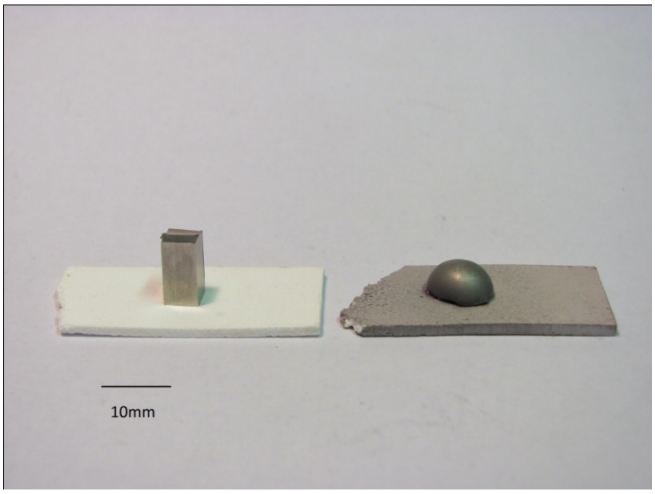

Figure 12: CMSX-4 samples on yttria substrates before and after melting

The furnace is capable of reducing pressure to 10^{-4} MPa. The furnaces currently used industrially are capable of achieving 10^{-6} MPa. It is therefore likely that more chemical interactions between the metal and furnace atmosphere will take place in this furnace than in the industrial process.

The process used is designed to replicate the conditions used in industrial casting while isolating the core material and removing the effect of metal-shell interactions. It has the added advantage that a full mould does not need to be built. Possible inaccuracies in the technique include the small size of the drop, which increases the surface area to volume ratio and could lead to greater loss of RE additions through diffusion, and the greater proportion of the metal surface which is free to the atmosphere than in a commercial mould.

2.6 Sample Preparation

After melting, the metal samples were prepared for inspection by scanning electron microscope (SEM). First they were removed from the substrate and cut in half along their vertical axis by Accutom-5 machine using a silicon carbide disc. The drops had to be mounted in Bakelite before cutting as they were too small to fit directly into the machine. After cutting the Bakelite was removed and the samples re-mounted in Bakelite revealing the internal face. The mounted samples were polished using the following regime:

Struers Piano disc with running water for 5 mins at 250 rpm

Struers Allegro disc with 6 µm liquid diamond for 10 mins at 125 rpm

Struers Largo disc with 3 µm liquid diamond for 10 mins at 125 rpm

Struers Chem cloth with 50% Struers OP-A acid alumina suspension in 50% water for 10 mins at 125 rpm.

Some of the ceramic substrates (V200 and Al_2O_3, both as-sintered and after heating with CMSX-4 for 5 mins) were mounted in epoxy and polished under the same regime, but using a Struers Dac cloth and 1 µm liquid diamond in the final stage.

2.7 Characterisation of samples

2.71 Scanning electron microscope

After polishing, the samples were scanned in a Philips XL-30 scanning electron microscope (SEM) in secondary electron (SE) mode at an accelerating voltage of 20 kV and a working distance of 10 mm. Samples were analysed for elemental content using electron dispersive X-ray spectroscopy (EDS) on the same machine under the same conditions.

The SE and EDS techniques analyse different types of emission produced when an incoming electron from the electron gun of the SEM interacts with the sample. There are several ways an electron can be scattered by a sample. One is an elastic collision, known as backscattering. Backscattered electrons can give clues to the elemental composition of a sample, as backscattering is more likely to occur with nuclei of high atomic number. In this study backscattered images were found to be too indistinct to be of use.

Inelastic collisions of electrons with a sample can result in three different types of emission: secondary electrons, Auger electrons and characteristic X-rays. If an incoming electron knocks a valence electron in the sample out of its orbital, this latter electron can be emitted with comparatively low energy and is known as a secondary electron (SE). SE images were chosen for most of the imaging in this study as they have the greatest clarity and detail.

If the incoming electron collides with an inner shell electron in the sample causing it to leave the orbital, electrons drop down from the outer shells to fill the gap leaving an excited ion. The ion then loses its excess energy by emitting an electron or a photon in the X-ray part of the spectrum. These emissions have a characteristic energy depending on which orbital the original electron was lost from and the nuclear charge of the atom. Emitted electrons are known as Auger electrons and can be used to characterise a sample, however fluoresced X-rays are more commonly used in spectroscopy. Two different types of detector are used to characterise a sample from fluoresced X-rays: energy dispersive X-ray spectroscopy (EDS) uses a semiconductor-based detector to convert the X-rays into electrical signals of voltage corresponding to the photon energy which are then analysed by a computer, while wavelength dispersive X-ray spectroscopy (WDX) passes the X-rays through a diffraction grating to select individual wavelengths. EDS is generally easier and cheaper, and can be used to map an area of a sample as well as a point source. WDX requires the acquisition and use of elemental standards for each element under investigation, but has lower detection limits and better accuracy than EDS.

2.72 Quantification of reactive element loss

Finding a technique which would easily and directly quantify the amounts of yttrium and lanthanum remaining in the CMSX-4 samples after casting was challenging due to the complexity of the alloy and the low concentrations of the elements in question. Techniques which were considered included:

Inductively coupled plasma mass spectrometry (ICP-MS): mass spectrometry would be the best technique to use as it gives a direct elemental analysis. ICP is the only commonly-used ionisation technique that can evenly vaporise a complex alloy. ICP-MS could not be used in this project due to lack of equipment.

X-ray fluorescence spectroscopy (XRF) was tested; the detection limit was too high to find Y and La at the concentrations present.

Wavelength dispersive X-ray spectroscopy (WDX) was tested; this only tests a point source on the sample and the concentration of Y and La was found to vary too much to give consistent results with this technique.

Wet chemical methods were considered; the alloy is too complex to analyse this way. Auger spectroscopy and electron energy loss spectroscopy were also considered but thought not to have any advantage over more standard techniques.

Electron dispersive X-ray spectroscopy (EDS) was found to be the only available technique which could accomplish the task, despite its relative inaccuracy at the concentrations present. The scanning technique employed went as follows:

Starting at the surface which had been in contact with the ceramic, but not including the reaction layer, and moving in a straight line toward the centre of the sample, 50 images were scanned of each sample at 3000 x magnification. Each image had an area of 20 μm x 15 μm, making the total area scanned 0.015 mm^2 for each sample.

Potential La/Y rich areas were identified from the SE image and the presence of Y and La ascertained using EDS. If Y or La was found, the dimensions of the Y/La containing area were measured using the on-screen ruler and the quantities of La and Y in atomic % were recorded using the INCA software for EDS. The area of each La/Y rich grain was calculated and multiplied by the % of element found to give an equivalent amount of substance for La and Y in each grain. These quantities were then summed to give the total quantity of each reactive element in each sample.

This technique will give an underestimate of the actual levels of RE present as it only measures the amount of La/Y which exsolves on cooling. Some of the RE additions will be dissolved in the alloy matrix and undetectable by EDS. It is assumed that the level of this dissolution is constant for the alloy, and thus the EDS technique will give a good comparison between samples.

Interaction volumes will also lead to an underestimate of La/Y quantities. The fluoresced X-rays picked up by the EDS detector may come from anywhere in a teardrop-shaped volume which extends below and around the surface scanned. The percentage measurement recorded for each element is thus an average quantity for the whole interaction volume, which may be significantly larger than the La/Y rich area being studied.

There is significant potential for error in this technique, from the factors mentioned above, errors in measurement of area and statistical error.

2.73 Measurement of reactive layers

The thickness of the reactive layers formed on the outside of each metal sample was measured using the on-screen ruler of the SEM in secondary electron mode. At the interface the scanning procedure was as follows:

An image was taken at the interface next to the triple point at 3000 x magnification; giving a screen width of 30 µm. 5 measurements of the reactive layer thickness were made at evenly spaced intervals across the visible reactive layer. The image was zoomed out, moved so it was centred on a point 1 mm further along the reactive layer as measured by the on-screen ruler, and zoomed back to 3000 x magnification for a further 5 measurements to be made. This procedure was repeated until the triple point at the other side of the interface was reached. If the thickness of the reaction layer was not well defined this part of the interface was ignored. In many samples shrinkage of the drop on cooling had made the reaction layer thickness unclear due to convolution of the surface at the centre of the drop (for an example, see Fig. 28). Ill-defined reaction layers could also possibly be due to the reaction layer sloughing off during the mounting process.

Several measurements of the reaction layer thickness at the free surface for each sample were made for comparison.

3. Results and Discussion

3.1 Binder Systems

In choosing a binder for the dry pressing of substrates, consideration was given to homogeneity after mixing, green strength, ease of removal from the press and defects found after sintering. Wet pressing was also tried with some pieces and found to lead to irregularities on release from the press.

The binder components tested were methylcellulose, polyvinyl alcohol (PVA), and different molecular grades of polyethylene glycol (PEG). PEG and PVA were combined in later binder systems as PVA acts as a plasticiser for PEG, as well as being a binder in its own right. Glycerol was added to the PVA and PEG containing systems as it acts as plasticiser for both these compounds. A commercial dispersing agent, Dispex-A40, was also added to all the binder systems.

Methylcellulose was found not to work well, with pieces being difficult to remove from the press and deforming easily in the green state. The best results were gained from mixtures of PVA and PEG. Table 1 details the binder systems tested with comments on their performance.

Table 1: Binder systems

Mix	PVA (%)	PEG400 (%)	PEG900 (%)	PEG2000 (%)	Methyl-cellulose (%)	Glycerol (%)	Dispex (%)	Result
1		5				0.5	1	Soft
2		5		3		0.5	1	Brittle
3		5	3			0.5	1	Reasonable binding
4			5			0.5	1	Not binding
5			10			0.5	1	Warped on debinding
6					5	0.5	1	Stuck to press
7					2	0.5	1	Weak binding
8					3	0.5	1	Not binding
9	2		2			0.5	1	Not binding
10	2	1	2			1	1	Reasonable binding
11	2	2				1	1	Good binding

Binder system 11 was chosen for all the substrates used in this study.

3.2 X-Ray Tomography

Fig. 13 shows microtomography images comparing slices through pressed and injection moulded ceramics.

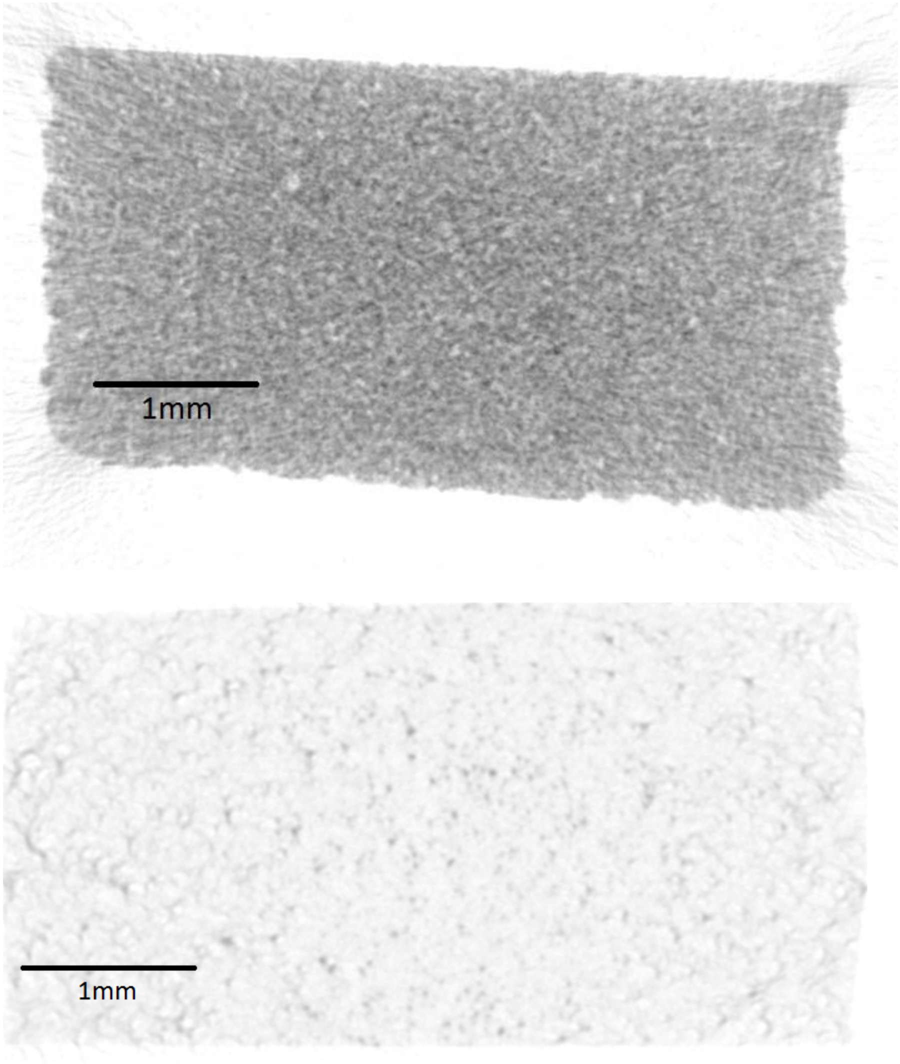

Figure 13: X-ray microtomography cross-sections of pressed alumina (top) and injected V200 (bottom)

The difference in brightness of the images is an artefact of the scanning process rather than a property of the samples themselves. It can be said that the ceramics are of similar homogeneity and internal structure, although a quantitative measure is not possible from this data.

3.3 Density of substrates

The density of the sintered substrates from measured mass and volume is shown in Table 2.

Table 2: Density of substrates

Substrate	Sample density (g/cm^3)	Theoretical density (g/cm^3)	Relative density
V200 (Injected)	1.6 ±0.15	2.2	0.74
V200 (Pressed)	1.5 ±0.15	2.2	0.72
Alumina	2.2 ±0.15	3.9	0.56
Yttria	3.7 ±0.15	5.0	0.74

Theoretical density data is from Goodfellow Ltd[55].The values for V200 show that powder pressing gives very similar density to injection moulding, at least for this formulation. The relative densities of V200 and yttria are similar while alumina is a little less dense; this could be due to a lower degree of particle packing on formation or to less densification on sintering.

3.3 Furnace Pressure

As can be seen from Fig. 14, the pressure in the furnace is stable at around 0.2 Pa until the sample is raised into the hot zone, at which point there is a large increase in pressure. Much of this can be attributed to vaporisation of water adsorbed to the ceramic; there may also be a contribution from degassing of more volatile metal species in the alloy. Degassing is not significant after the first minute of heating, which makes evaporation unlikely to be a major route of RE loss.

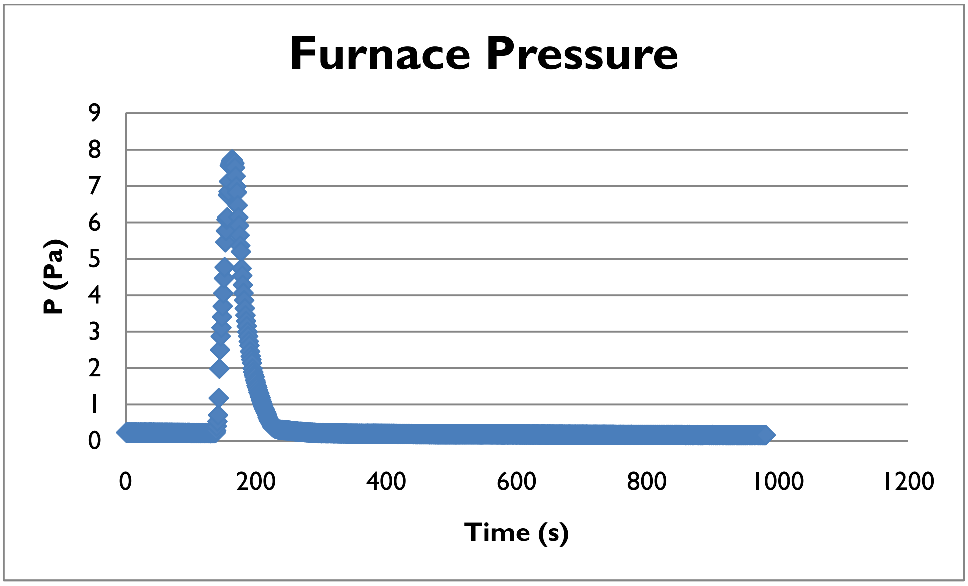

Figure 14: Furnace pressure-time graph for the heating of CMSX-4 on V200

3.5 Visual Observation

CMSX-4 did not wet or adhere to any of the ceramics, forming droplets which became generally more rounded with longer duration of heating and stabilised as round drops after 30-60 minutes. Yttrium did not adhere to, but exhibited a high level of spreading and wetting with all ceramics except Y_2O_3.

Yttrium appears to have fully melted between 2 and 5 mins (see Fig. 15). The sample melted for 5 mins exhibited a higher degree of spreading than the samples melted for longer periods; this could be because the substrate had a slightly convex character while the other samples were flat or slightly concave.

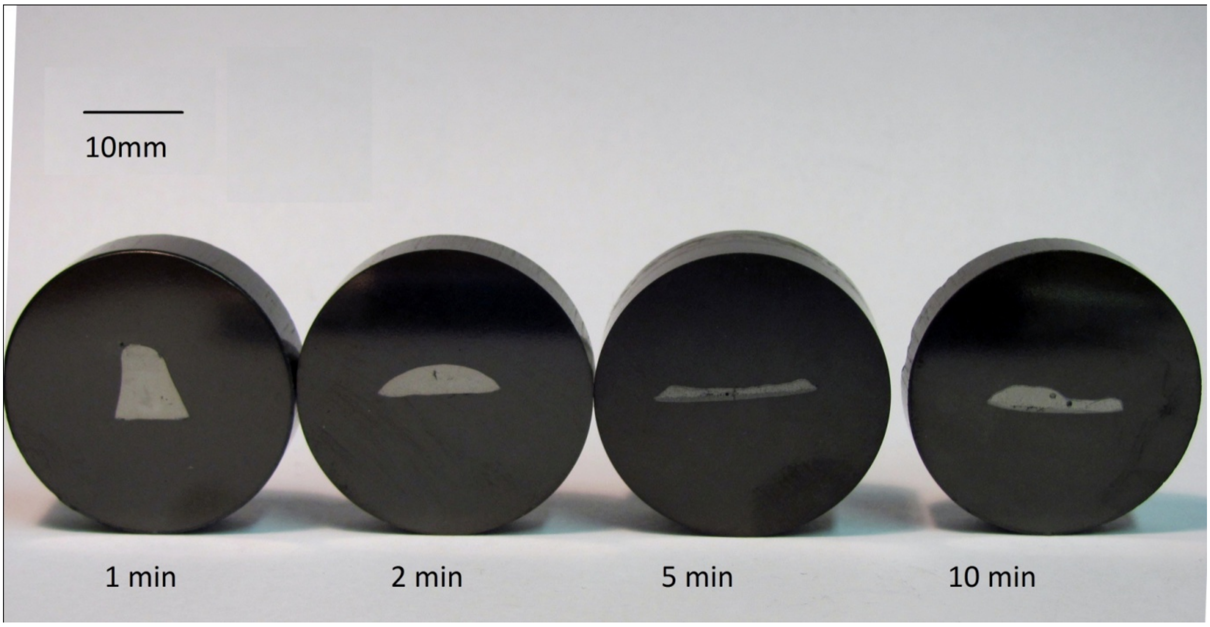

Figure 15: Spreading of yttrium samples after melting on V200 substrates

Figure 16: Discolouration and dissolution of substrates - V200 after heating with CMSX-4 (left) and yttrium (right); yttria after heating with CMSX-4 (centre)

Unlike the other substrates, to which yttrium did not adhere, the Y_2O_3 substrate fused to the yttrium sample. This piece of yttrium also appeared not to melt, keeping its cuboid shape relatively intact after casting had finished. A black glassy layer was present on the surface of the entire metal-ceramic couple, which was confirmed by X-ray diffraction as Y_2O_3. This compound could be a sub-stoichiometric form of yttria formed by mutual dissolution of yttria and yttrium. The Y- Y_2O_3 phase diagram[56] indicates that this partially oxidised form of yttrium is stable at a wide range of oxygen contents and undergoes a phase transition at 1465 K, which could account for the fused appearance of the compound.

The other substrates (V200, Al_2O_3, Y_2O_3/Al_2O_3 mix) had all been eaten away underneath yttrium as shown for V200 in Fig. 16, indicating two possible processes: diffusion of the ceramic into yttrium and a reaction taking place in liquid metal solution which consumes the ceramic.

Yttrium on Al_2O_3 has an open structure on the bottom of the metal as if it formed gas bubbles at the interface. Also, a pastel blue colour was observed on the surface of V200 after casting with pure Y (Fig. 16). This is possibly a product of the reaction of zircon ($ZrSiO_4$) in V200 with a vanadium[57] or similar impurity in yttrium.

A green discolouration was observed on the surface of V200 samples cast with CMSX-4 (see Fig. 16) which indicates the presence of Cr_2O_3 and therefore a degassing of chromium metal.

Dark imprints were observed on all the ceramic substrates in places where they had been in contact with the CMSX-4 samples. This indicates that metal elements diffuse into the ceramic very early on in the casting process.

All the Y_2O_3 samples turned black after melting in the furnace, whether or not a metal sample was present, as can be seen on the centre substrate in Fig. 16. No chemical change was observed by X-ray diffraction. This indicates a partial reduction of Y_2O_3 by the furnace atmosphere[58]. The related oxide zirconia (ZrO_2) is known to discolour to black with only minor loss of oxygen, although some authors[59] suggest that this is due to reduction of iron impurities in the ceramic. A small quantity of iron is likely to be present in the ceramics studied here, due to the steel die used to prepare the substrates. Alternatively the black colour could be from a layer of carbon transferred from the heating element of the furnace in the following reaction:

Water desorbed from the sample during heating reacts with the heater forming CO. Previous mass spectrometry experiments[60] have confirmed that this reaction occurs. CO is then reduced by the partially reduced ceramic.

$$H_2O + C \rightarrow CO + H_2$$

$$nCO + nY_2O_{3-n} \rightarrow nY_2O_3 + nC$$

This reaction is thermodynamically favoured for all the substrates tested, however the black colour was only observed on yttria indicating that the formation of a black sub-stoichiometric form of yttria is more likely.

3.2 SEM

Comparison of injection-moulded and pressed ceramics shows a similar internal structure, packing and density (Figs. 17 and 18). No difference could be observed between the ceramic samples which had been heated with metal and the as-sintered samples under SEM or EDS. This is attributed to the quantities of elements from the alloy which diffused into the ceramic being below the detection limit.

SEM (Figs. 19 and 20) and EDS (Fig. 21) analysis of the pure yttrium samples showed the presence of Y_2O_3 throughout the solidified metal in all the samples. Concentration of oxygen increased toward the substrate. This indicates a fast rate of diffusion of oxygen from the substrate into yttrium, and indicates that the reaction takes place in solution in the liquid metal. Silicon was also found to have dissolved from the substrate into yttrium.

Reactive layers were found on the surface of all the cast CMSX-4 samples (Figs. 22-25), which were found by EDS (Fig. 26) to contain significant quantities of the elements Y, La and O. These reactive layers were found on all surfaces of the drops; at the free surfaces the layers had an almost uniform thickness of 0.5-1.5 μm, with occasional growth up to 10 μm. Thicker, non-uniform layers were found on the bottom surfaces of the drop which had been at the metal-ceramic interface. On some of the drops, thickening of the layer was found on the free surface of the metal near to the triple point.

A kinetic explanation for the formation of the reactive layers is as follows: Y and La, as the most reactive elements in the alloy, segregate to the surface of the drop and scavenge any available oxygen to form Y_2O_3 and La_2O_3. At the free surface this occurs rapidly with air adsorbed on the surface of the drop. At the interface with the ceramic oxygen is liberated from the substrate to react on the surface of the metal. That the reaction product forms on the metal surface, rather than on the ceramic, indicates that oxygen can diffuse to the interface faster than yttrium and lanthanum, as would be expected for the smaller species. This is also an indication that little Y and La is lost at the interface by diffusion without reaction, as it would be oxidised by the substrate first.

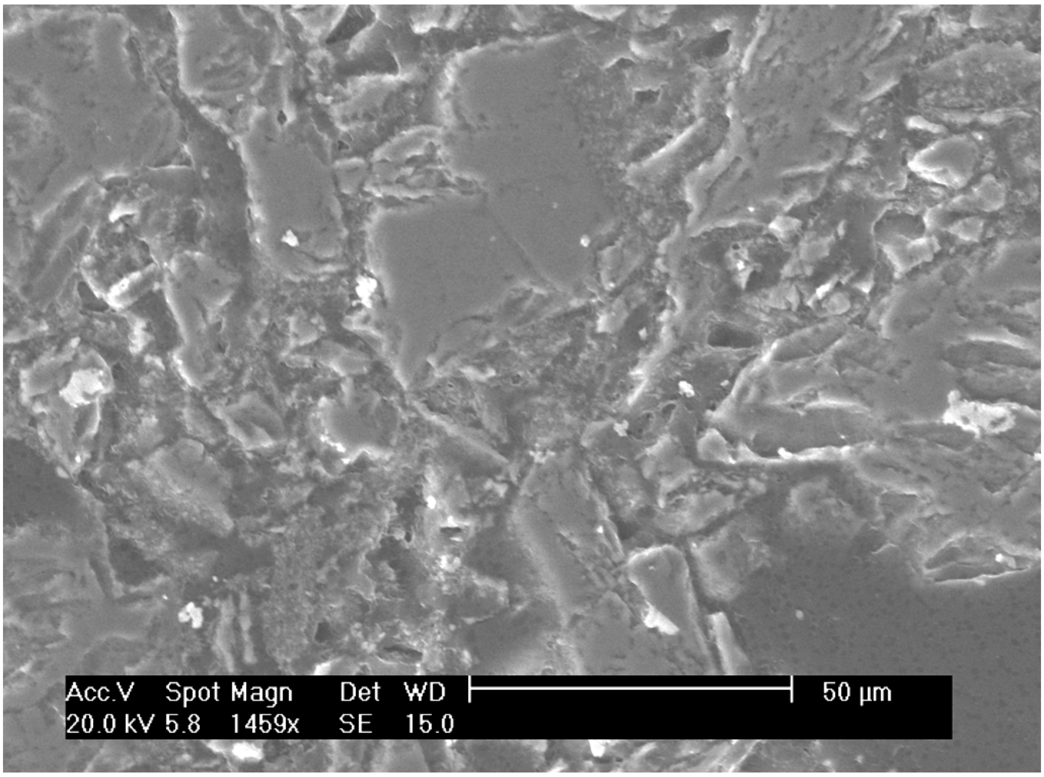

Figure 17: SEM image of pressed alumina showing packing

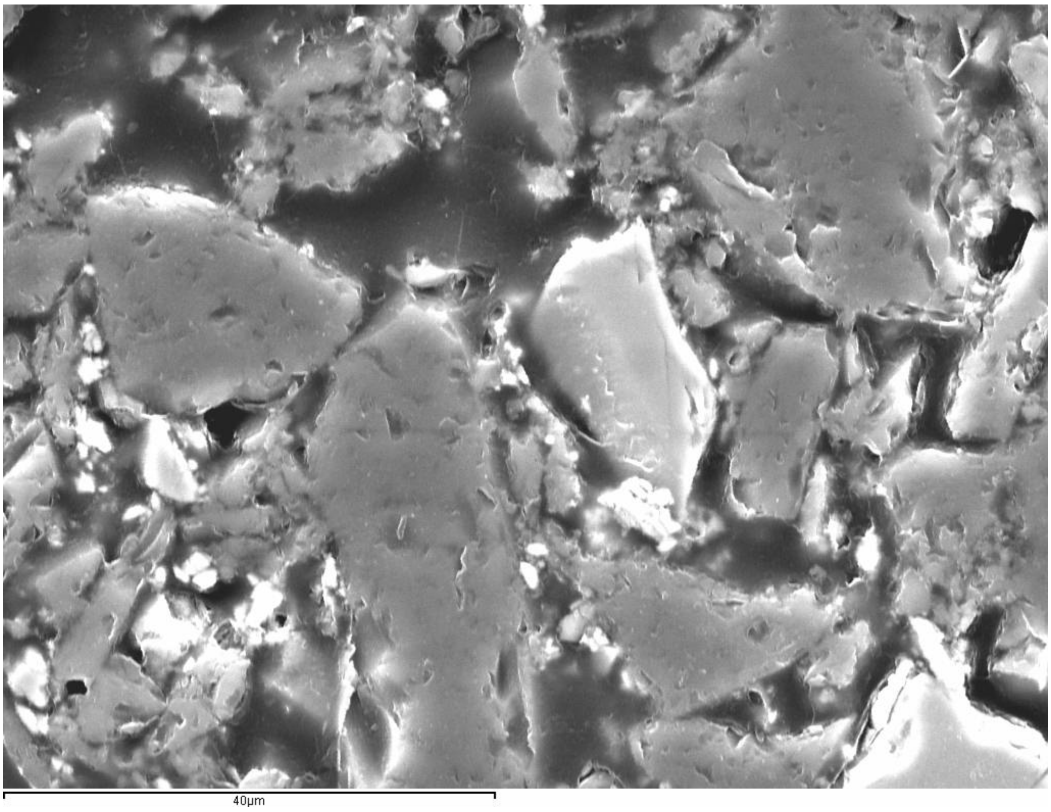

Figure 18: SEM image of injected V200 taken at 2000 x magnification in SE mode. Zircon particles appear lighter in colour than silica particles.

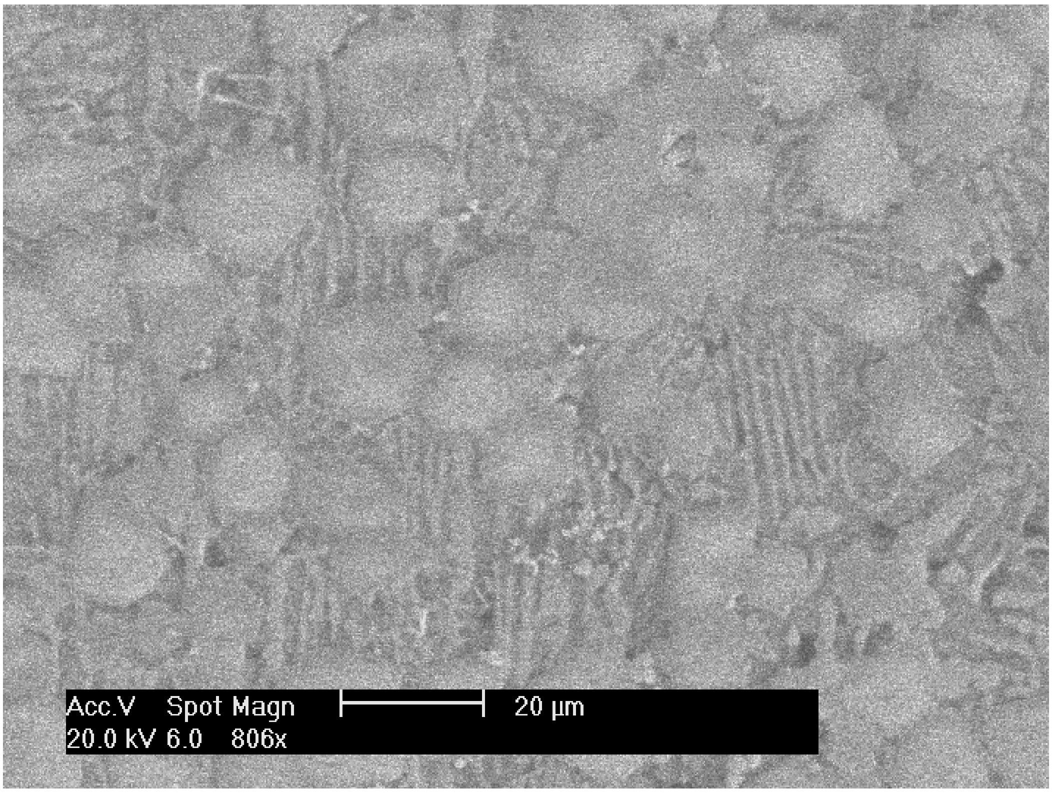

Figure 19: SEM image of the internal morphology of a sample of yttrium after melting on V200 for 5 mins

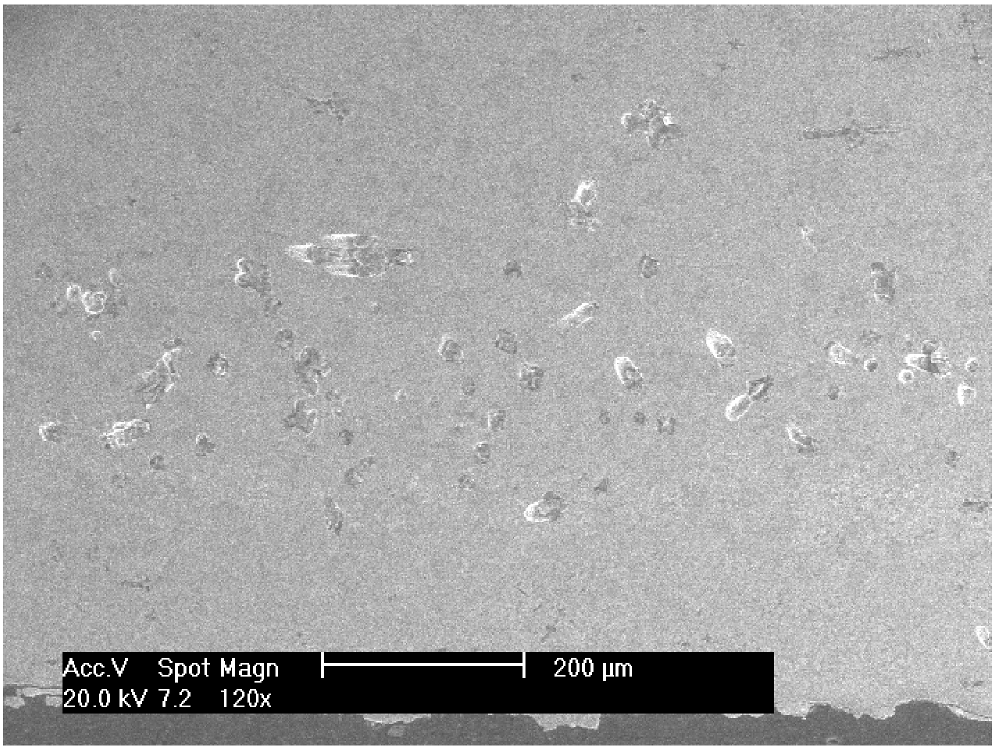

Figure 20: SEM image of an yttria sample after melting on a V200 substrate for 10 mins. Crystals of cubic yttria can be observed across the entire image.

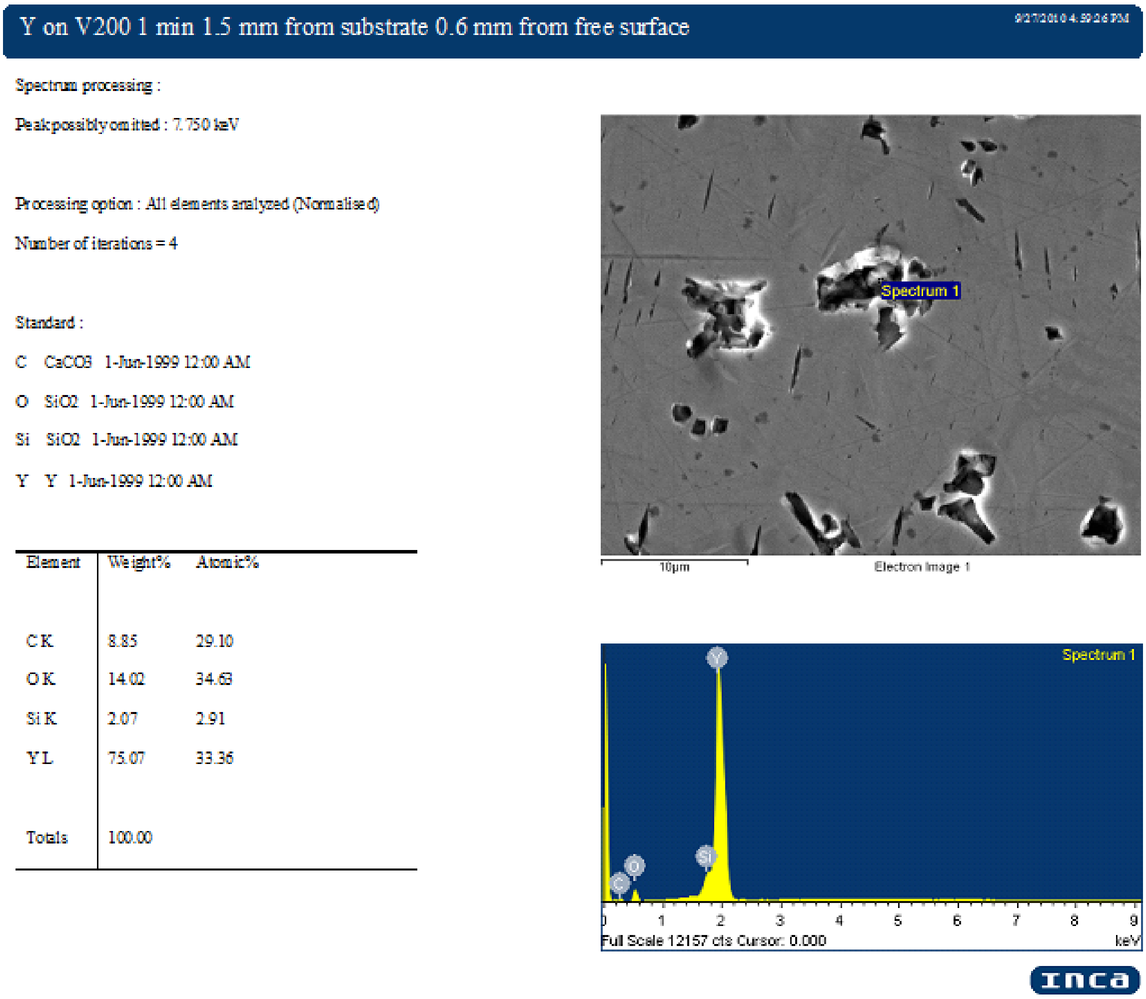

Y on V200 1 min 1.5 mm from substrate 0.6 mm from free surface

9/27/2010 4:59:26 PM

Spectrum processing :

Peak possibly omitted : 7.750 keV

Processing option : All elements analyzed (Normalised)

Number of iterations = 4

Standard :

C CaCO3 1-Jun-1999 12:00 AM

O SiO2 1-Jun-1999 12:00 AM

Si SiO2 1-Jun-1999 12:00 AM

Y Y 1-Jun-1999 12:00 AM

Element	Weight%	Atomic%
C K	8.85	29.10
O K	14.02	34.63
Si K	2.07	2.91
Y L	75.07	33.36
Totals	100.00	

Figure 21: EDS scan of yttrium melted on a V200 substrate for 1 min showing oxygen and silicon content

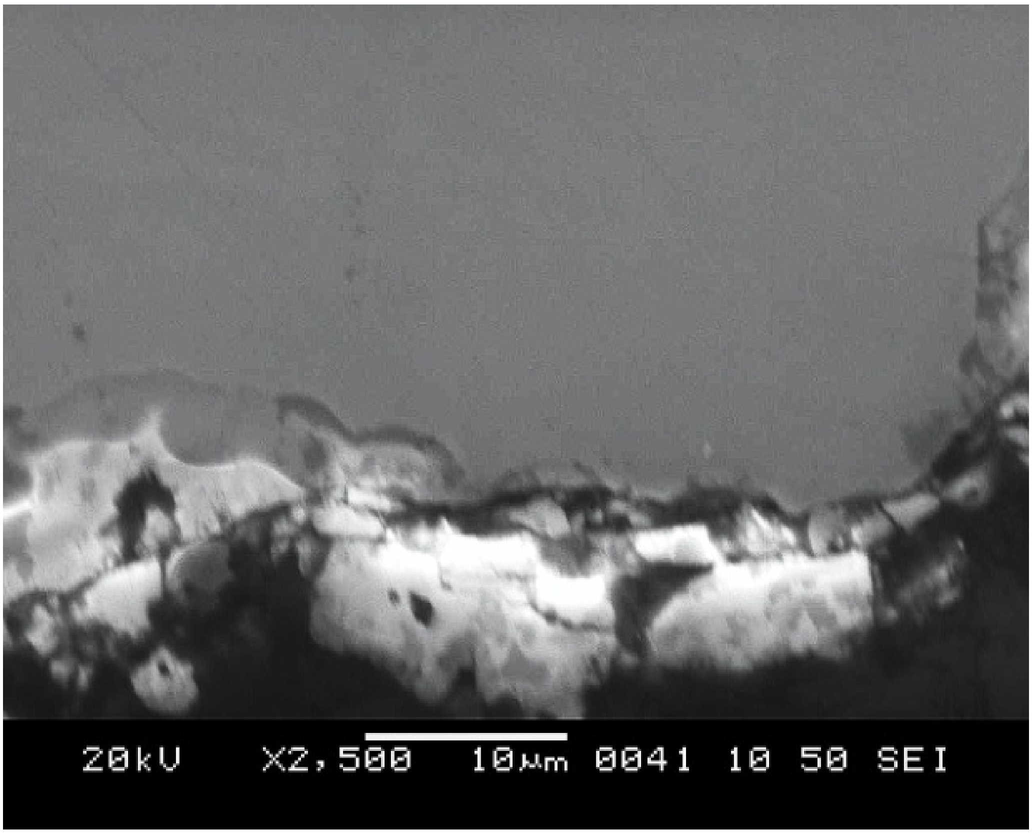

Figure 22: SEM image of CMSX-4 heated on V200 for 60 mins at 1450 °C showing interface reactive layer.

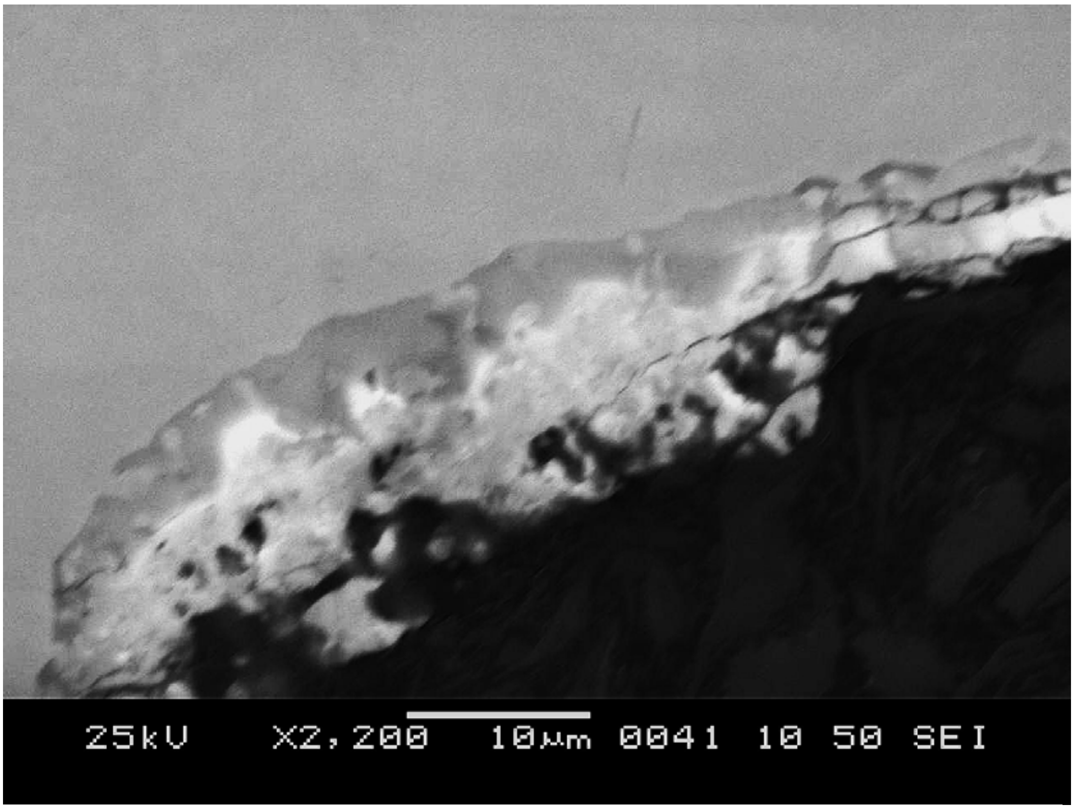

Figure 23: SEM image of CMSX-4 heated on V200 for 60 mins at 1450 °C showing interface reactive layer.

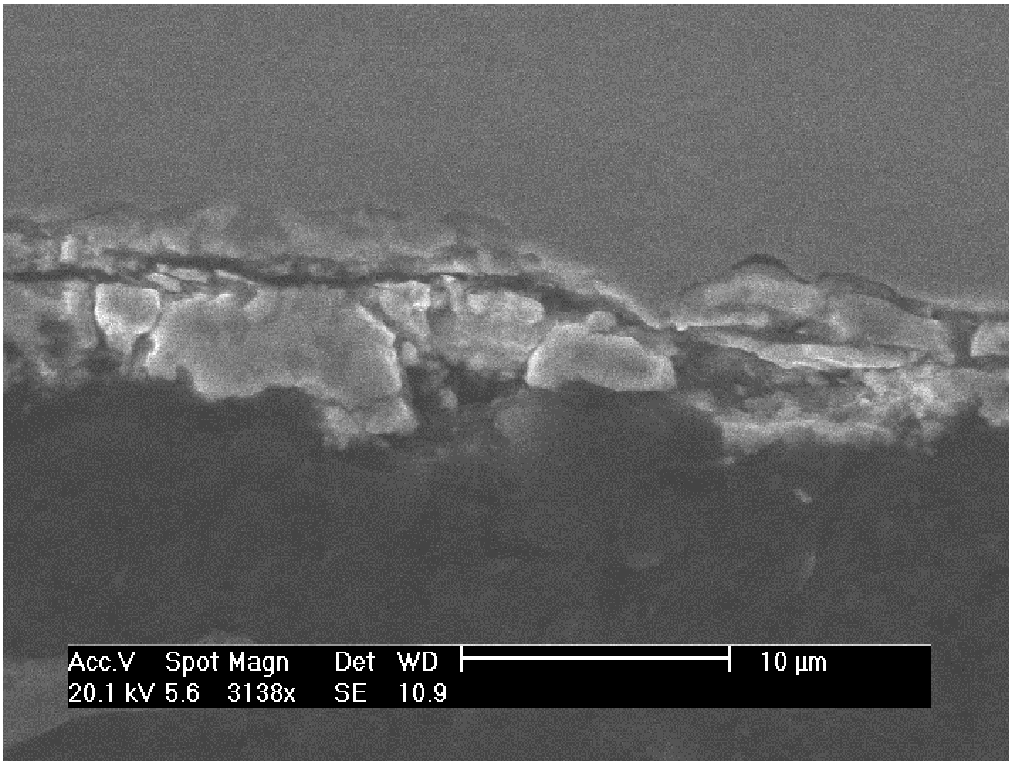

Figure 24: SEM image of CMSX-4 heated on V200 for 15 mins at 1500 °C showing interface reactive layer.

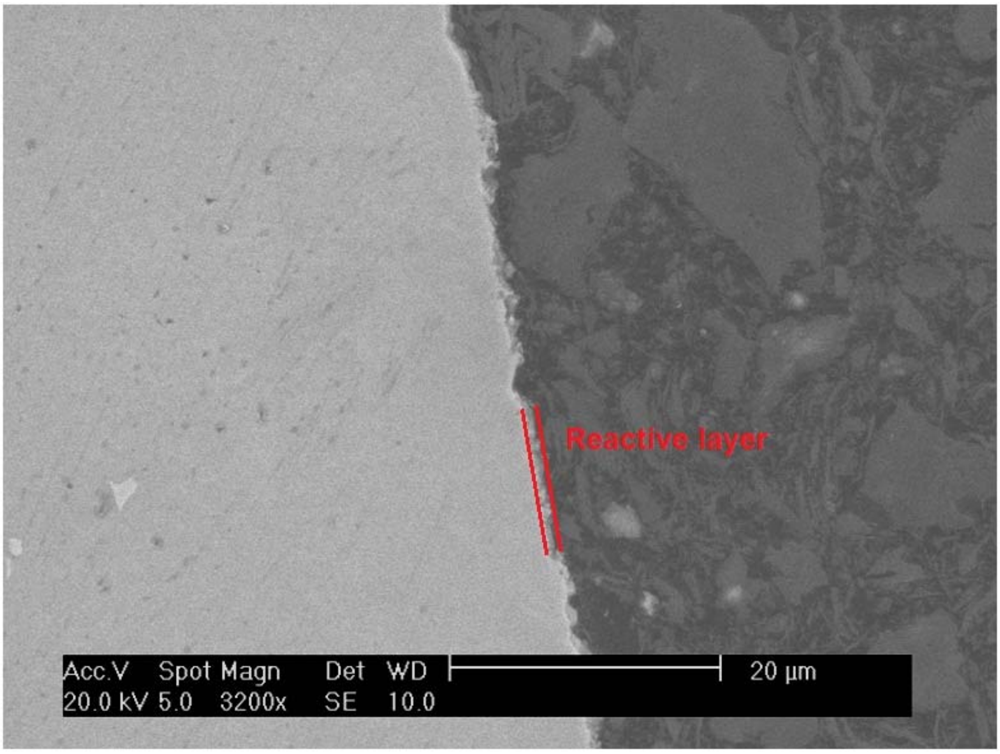

Figure 25: SEM image of CMSX-4 heated on alumina/yttria for 60 mins at 1550 °C showing free surface reactive layer.

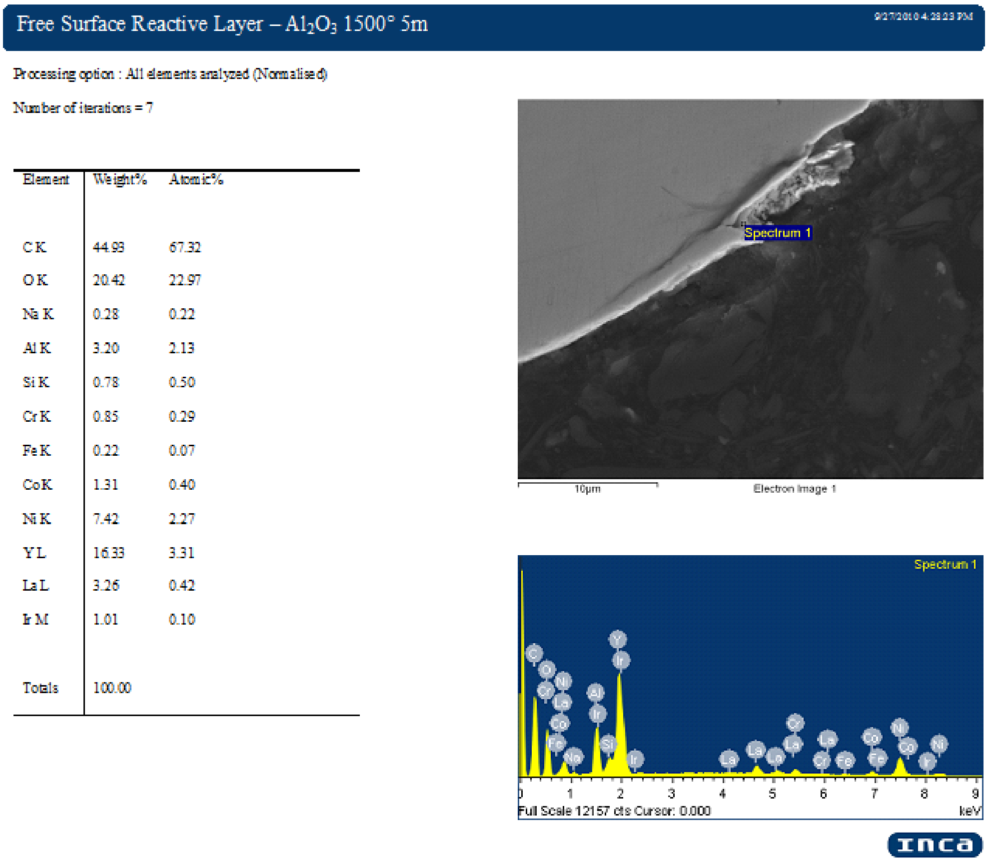

Free Surface Reactive Layer – Al_2O_3 1500° 5m

9/27/2010 4:28:23 PM

Processing option : All elements analyzed (Normalised)

Number of iterations = 7

Element	Weight%	Atomic%
C K	44.93	67.32
O K	20.42	22.97
Na K	0.28	0.22
Al K	3.20	2.13
Si K	0.78	0.50
Cr K	0.85	0.29
Fe K	0.22	0.07
Co K	1.31	0.40
Ni K	7.42	2.27
Y L	16.33	3.31
La L	3.26	0.42
Ir M	1.01	0.10
Totals	100.00	

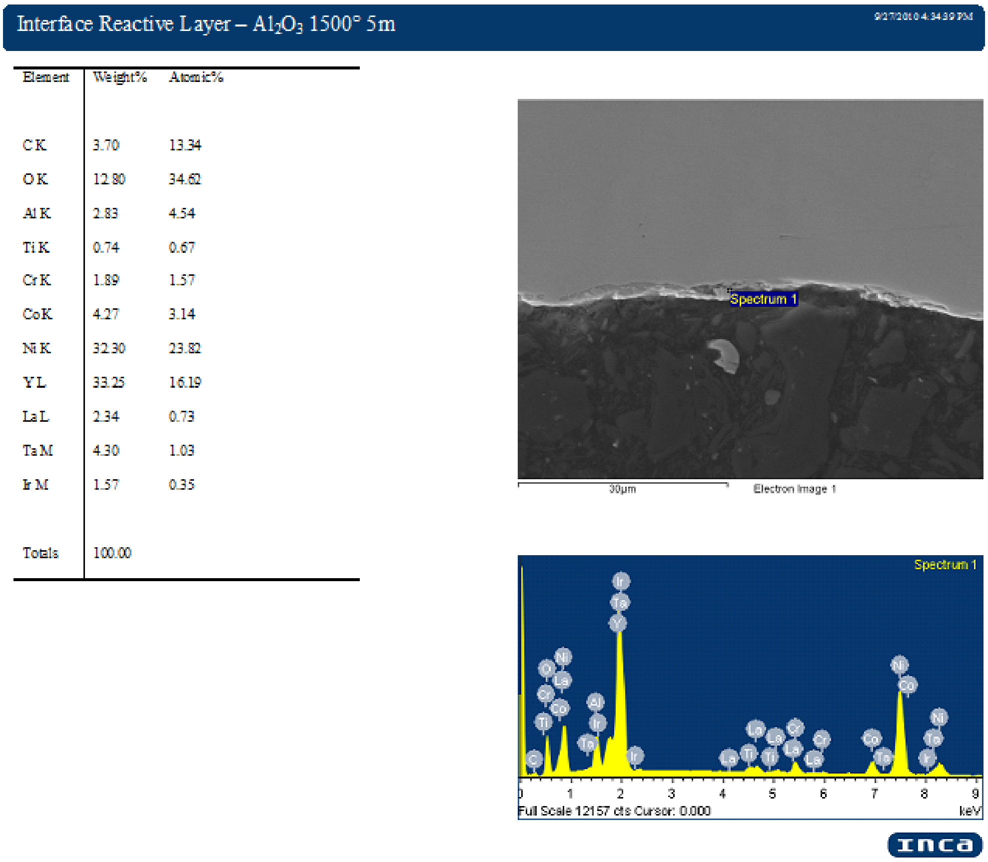

Interface Reactive Layer – Al_2O_3 1500° 5m

9/27/2010 4:34:39 PM

Element	Weight%	Atomic%
C K	3.70	13.34
O K	12.80	34.62
Al K	2.83	4.54
Ti K	0.74	0.67
Cr K	1.89	1.57
Co K	4.27	3.14
Ni K	32.30	23.82
Y L	33.25	16.19
La L	2.34	0.73
Ta M	4.30	1.03
Ir M	1.57	0.35
Totals	100.00	

Figure 26: EDS scans of reactive layers

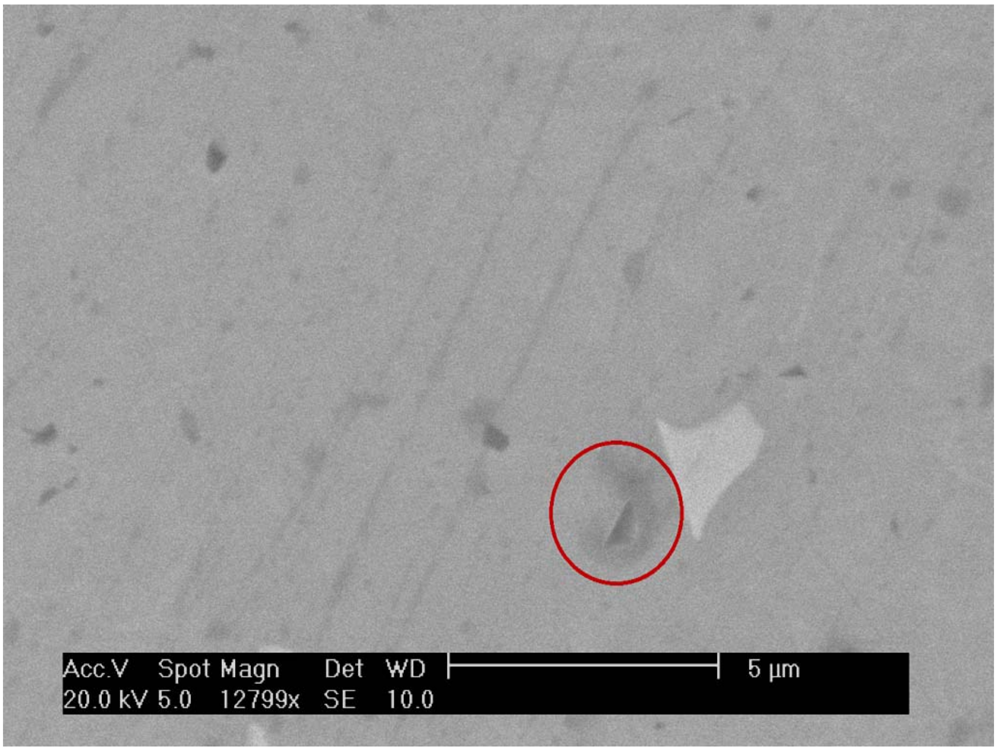

Figure 27: SEM image of CMSX-4 heated on alumina/yttria for 60 mins at 1550 °C showing eutectic phase (circled).

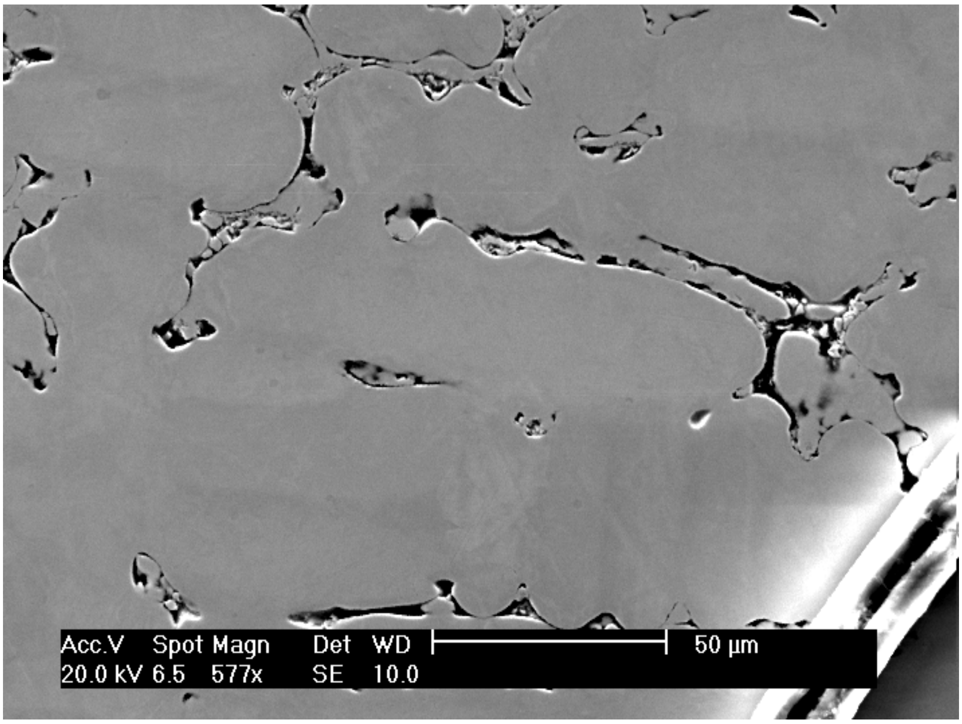

Figure 28: SEM image of CMSX-4 heated on yttria for 15 mins at 1550 °C showing porosity caused by shrinkage on cooling. None of the eutectic phase was found in this image.

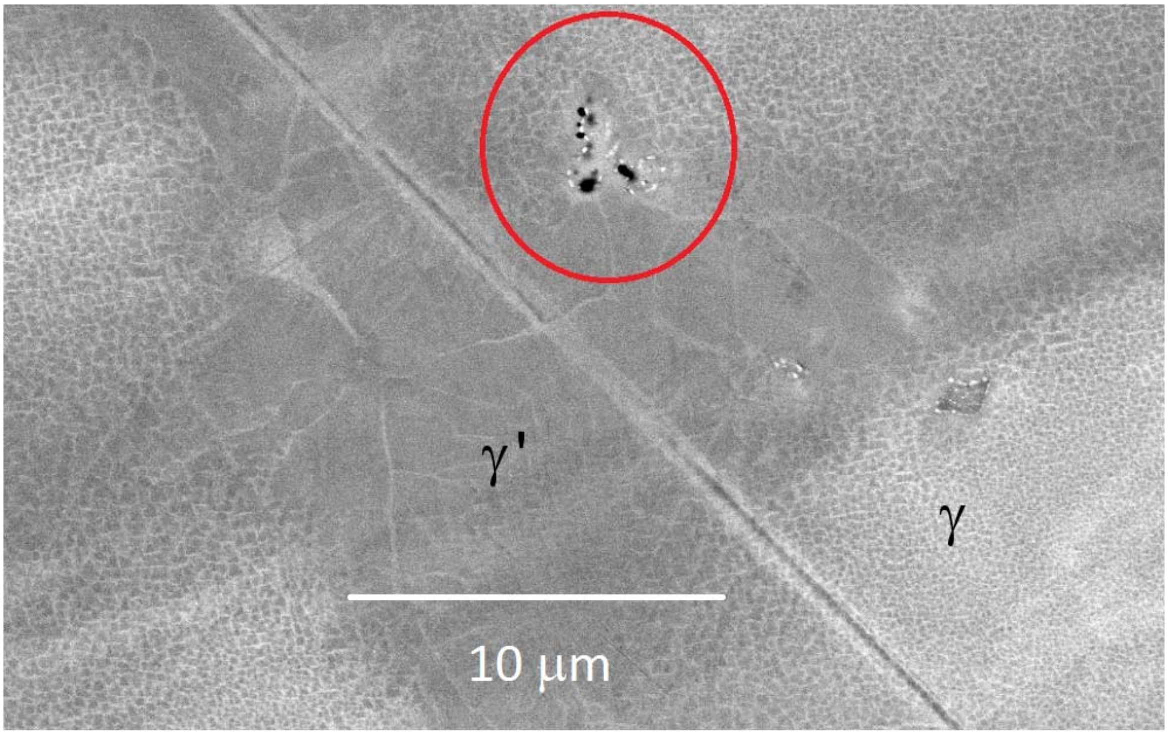

Figure 29: SEM image of Y/La rich eutectic approx. 3 microns in diameter (circled) in CMSX-4 matrix. This sample had been cast against an Al_2O_3 substrate for 5 mins.

In the bulk of the CMSX-4 alloy small grains in the order of 0.5-5µm in diameter were observed of a darker colour to the matrix which were confirmed by EDS as rich in Y and La (Figs. 27, 29, 30). Where one of these metals was found, the other was usually present. It has previously been confirmed that yttrium forms a low melting point eutectic with nickel[61] and it follows that what was observed here was this phase, having formed droplets as the last phase in the alloy to cool.

Fig. 29 was taken on a Jeol 7000 SEM and shows greater detail of the eutectic than the other images. The γ and γ' phases can also be observed in this image (see section 1.5). The images used to generate the data in section 3.4 were of the quality of figs. 27 and 28, which meant that there were many areas which were indistinguishable from the eutectic in the SE image which did not contain La or Y, the presence of which had to be verified using EDS.

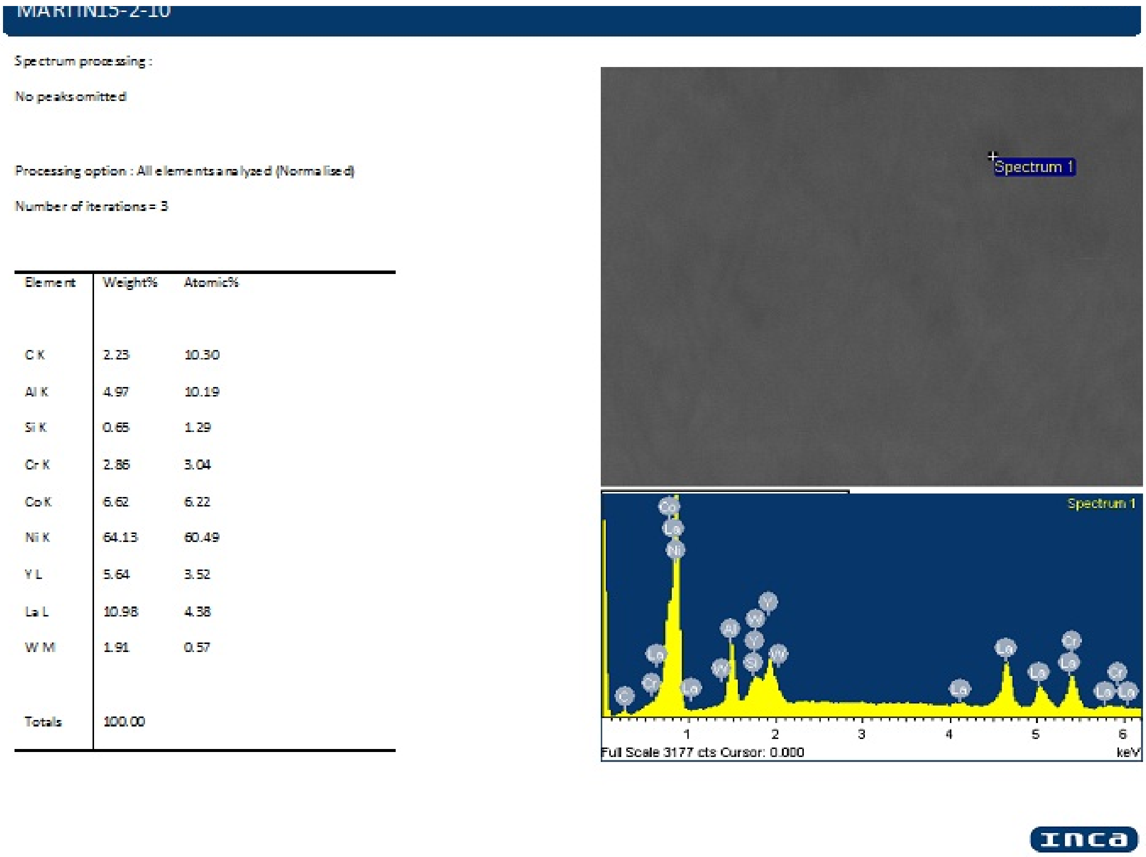

MARTIN15-2-10

Spectrum processing :

No peaks omitted

Processing option : All elements analyzed (Normalised)

Number of iterations = 3

Element	Weight%	Atomic%
C K	2.23	10.30
Al K	4.97	10.19
Si K	0.65	1.29
Cr K	2.86	3.04
Co K	6.62	6.22
Ni K	64.13	60.49
Y L	5.64	3.52
La L	10.98	4.38
W M	1.91	0.57
Totals	100.00	

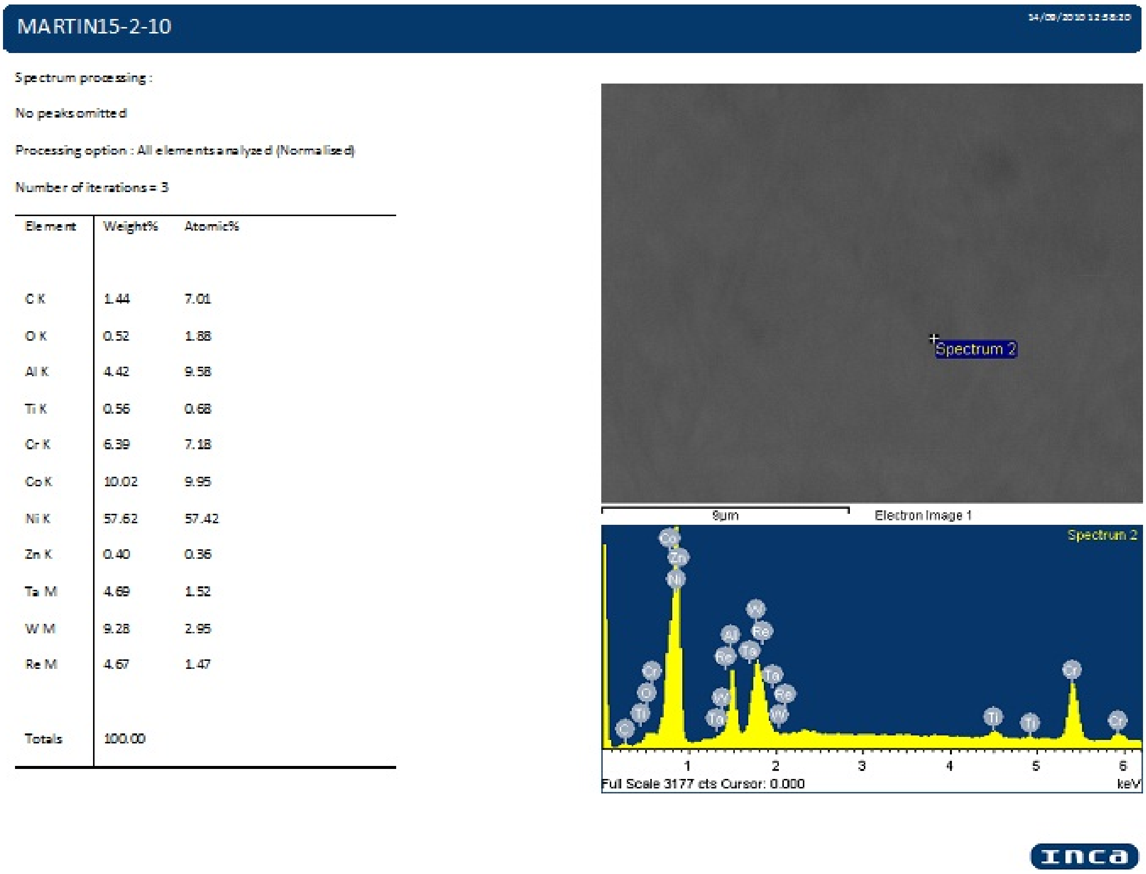

MARTIN15-2-10

Spectrum processing :

No peaks omitted

Processing option : All elements analyzed (Normalised)

Number of iterations = 3

Element	Weight%	Atomic%
C K	1.44	7.01
O K	0.52	1.88
Al K	4.42	9.58
Ti K	0.56	0.68
Cr K	6.39	7.18
Co K	10.02	9.95
Ni K	57.62	57.42
Zn K	0.40	0.36
Ta M	4.69	1.52
W M	9.28	2.95
Re M	4.67	1.47
Totals	100.00	

Figure 30: Sample EDS scans from CMSX-4 heated on yttria for 5 mins at 1550 °C

3.3 Quantification of reactive element loss

Fig. 30 shows an example SEM image from CMSX-4 heated on a Y_2O_3 substrate for 5 mins taken at approximately 200 μm from the interface. EDS spectra have been taken at two candidate eutectic areas in the image, one containing Y/La and one not. Images like these, for samples melted for 5 mins with each substrate, were used to compile Table 3.

Table 3 shows the following information: The first column numbers the spots, the second indicates which image of the 50 scanned the spot was found in. The images which did not contain any areas of eutectic are not shown in the table. The next columns give the dimensions of the spots found to contain Y and La. If a spot was closer to a circular shape then its area was calculated from its diameter, while if the spot was more rectangular then its width and height were measured. The area calculated from these dimensions is shown next, then these areas as percentages of the total 15000 μm^2 scanned. The summed percentages for each sample are displayed in Fig. 31.

The right-hand columns show the percentages of Y and La shown on the EDS scans for each spot. The area of each spot was multiplied by these percentage values, divided by the total area scanned and multiplied by a factor of 100 to give the amount of RE present as parts-per-million (ppm) of all the substances present in the sample area scanned. These ppm values are summed for each sample and displayed in Fig. 32.

This technique only measures La and Y present above their dissolution limits in the alloy. A proportion of the quantities present of these elements are dissolved in the alloy and are thus unaccounted for by this technique. For the purposes of this study the dissolution limits are assumed to be constant between samples.

Table 3: Amount of eutectic remaining in samples after melting

V200

Area	Image	Width (µm)	Height (µm)	Dia (µm)	Area (µm)^2	% of Total Area	% Y	% La	Proportion Y in sample (ppm)	Proportion La in sample (ppm)
1	13			0.3	0.07	0.0005		0.8	0.00	0.04
2	15			1.0	0.79	0.0052	4.0	1.7	2.09	0.89
3	16			1.0	0.79	0.0052		1.0	0.00	0.52
4	36	1.5	2.0		3.00	0.0200	3.5	3.0	7.00	6.00
5	41			1.0	0.79	0.0052	4.0	3.0	2.09	1.57
6	41			2.0	3.14	0.0209		0.8	0.00	1.68
7	42	1.0	0.8		0.80	0.0053	2.0	1.4	1.07	0.75
8	43	2.0	1.0		2.00	0.0133	2.4	1.7	3.20	2.27
9	46			0.8	0.50	0.0034		0.7	0.00	0.23
Total					11.87	0.0791			15.46	13.95

Y_2O_3

Area	Image	Width (µm)	Height (µm)	Dia (µm)	Area (µm)^2	% of Total Area	% Y	% La	Proportion Y in sample (ppm)	Proportion La in sample (ppm)
1	2	2.0	1.0		2.00	0.0133	6.0	1.0	8.00	1.33
2	2	1.0	0.5		0.50	0.0033		3.0	0.00	1.00
3	4			1.0	0.79	0.0052	1.5	4.0	0.79	2.09
4	6	2.0	4.0		8.00	0.0533	7.0	1.0	37.33	5.33
5	13	0.5	1.0		0.50	0.0033	3.0	3.0	1.00	1.00
6	14	6.0	2.0		12.00	0.0800	3.5	3.5	28.00	28.00
7	16	2.0	1.0		2.00	0.0133	3.0	3.0	4.00	4.00
8	17			0.5	0.20	0.0013		0.5	0.00	0.07
9	20			0.5	0.20	0.0013	1.5	1.0	0.20	0.13
10	21			0.5	0.20	0.0013	3.0	3.0	0.39	0.39
11	24			1.0	0.79	0.0052	2.5	1.2	1.31	0.63
12	25	3.0	1.5		4.50	0.0300	5.0	4.0	15.00	12.00
13	26			1.5	1.77	0.0118	3.0	2.0	3.53	2.36
14	27			1.0	0.79	0.0052	4.0	4.0	2.09	2.09
15	31			2.0	3.14	0.0209	4.0	4.0	8.38	8.38
16	35			1.5	1.77	0.0118	3.5	4.4	4.12	5.18
17	38			0.5	0.20	0.0013		1.4	0.00	0.18
18	39	0.5	1.0		0.50	0.0033		1.1	0.00	0.37
19	42	2.0	0.5		1.00	0.0067	1.7	1.7	1.13	1.13
20	43			1.5	1.77	0.0118	3.3	3.3	3.89	3.89
21	45			0.5	0.20	0.0013	1.3	1.6	0.17	0.21
Total					42.78	0.29			119.34	79.77

Al_2O_3

Area	Image	Width (µm)	Height (µm)	Dia (µm)	Area (µm)^2	% of Total Area	% Y	% La	Proportion Y in sample (ppm)	Proportion La in sample (ppm)
1	4	2.0	0.5		1.00	0.0067	3.0	3.0	2.00	2.00
2	5	3.0	1.0		3.00	0.0200		1.0	0.00	2.00
3	14	0.5	0.5		0.25	0.0017	3.0	3.0	0.50	0.50
4	24			1.0	0.79	0.0052		0.4	0.00	0.21
Total					5.04	0.03			2.50	4.71

Y_2O_3/Al_2O_3

Area	Image	Width (µm)	Height (µm)	Dia (µm)	Area (µm)^2	% of Total Area	% Y	% La	Proportion Y in sample (ppm)	Proportion La in sample (ppm)
1	1	2.0	1.5		3.00	0.0200	6.0	5.0	12.00	10.00
2	1			0.5	0.20	0.0013		6.0	0.00	0.79
3	2	1.0	3.0		3.00	0.0200	4.0	7.0	8.00	14.00
4	9			1.0	0.79	0.0052	5.0	3.0	2.62	1.57
5	14			0.5	0.20	0.0013		1.4	0.00	0.18
6	30	1.5	4.5		6.75	0.0450	4.0	4.0	18.00	18.00
7	36			0.5	0.20	0.0013	2.3	1.6	0.30	0.21
8	37	0.5	1.0		0.50	0.0033		1.0	0.00	0.33
9	37			0.5	0.20	0.0013		1.7	0.00	0.22
10	43			1.5	1.77	0.0118		2.1	0.00	2.47
11	48			2.0	3.14	0.0209	5.3	4.5	11.10	9.42
Total					19.73	0.13			52.02	57.20

Control (Raw alloy)

Area	Image	Width (µm)	Height (µm)	Dia (µm)	Area (µm)^2	% of Total Area	% Y	% La	Proportion Y in sample (ppm)	Proportion La in sample (ppm)
1	1	2.0	2.0		4.00	0.0267	2.0	2.0	5.33	5.33
2	4	3.0	0.5		1.50	0.0100	2.9	2.0	2.90	2.00
3	4	1.0	0.5		0.50	0.0033	3.5	2.1	1.17	0.70
4	16	2.0	4.0		8.00	0.0533	5.0	3.6	26.67	19.20
5	18	0.5	0.5		0.25	0.0017		0.9	0.00	0.15
6	29	1.0	6.0		6.00	0.0400	6.3	4.3	25.20	17.20
7	30			0.5	0.20	0.0013	3.2	2.2	0.42	0.29
8	30			0.5	0.20	0.0013	3.2	2.2	0.42	0.29
9	30			0.5	0.20	0.0013	3.3	2.8	0.43	0.37
10	30			0.5	0.20	0.0013	3.3	2.8	0.43	0.37
11	30	3.0	1.5		4.50	0.0300	5.3	3.7	15.90	11.10

12	31	2.0	1.0		2.00	0.0133	6.9	4.4	9.20	5.87
13	34			0.8	0.44	0.0029	10.5		3.09	0.00
14	36			0.5	0.20	0.0013	7.2		0.94	0.00
15	40			0.5	0.20	0.0013	5.8	3.1	0.76	0.41
16	40			0.5	0.20	0.0013	5.0	3.5	0.65	0.46
17	41			1.0	0.79	0.0052	5.8	3.6	3.04	1.88
18	45			0.5	0.20	0.0013	2.8	2.6	0.37	0.34
19	46	0.5	2.0		1.00	0.0067	5.4	3.1	3.60	2.07
20				1.0	0.79	0.0052	0.0	2.2	0.00	1.15
Total					31.33	0.21			100.52	69.17

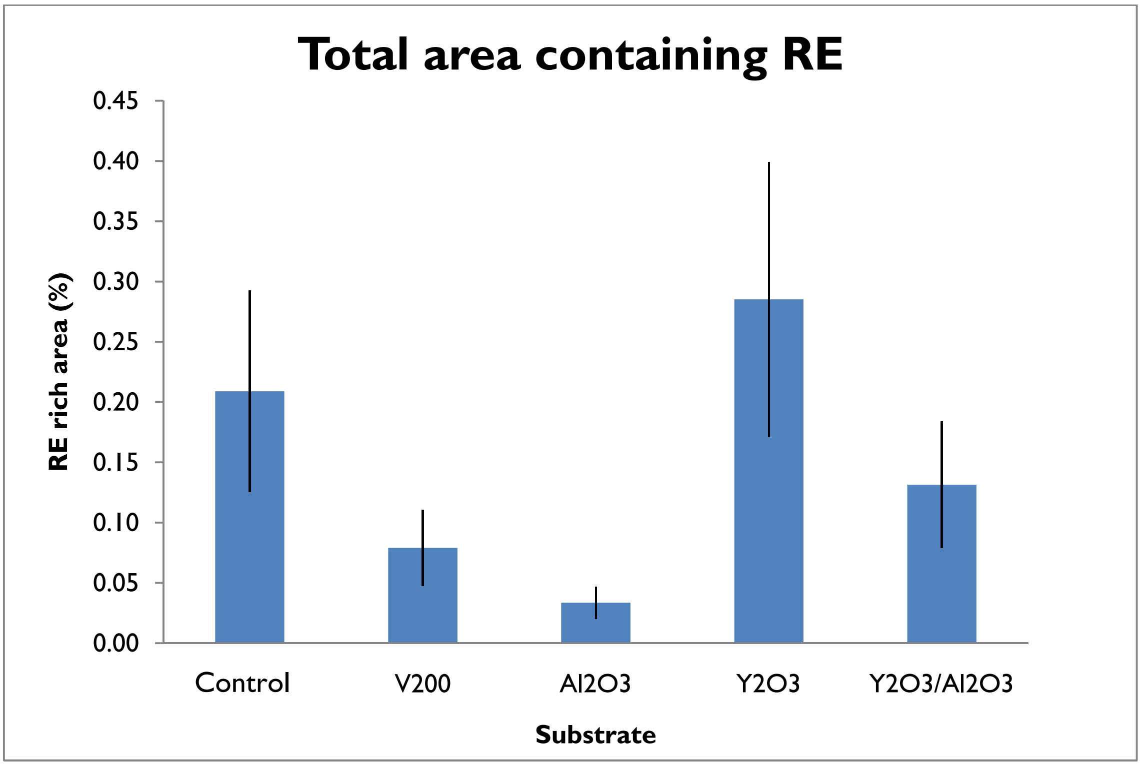

Figure 31: area of eutectic found before and after melting

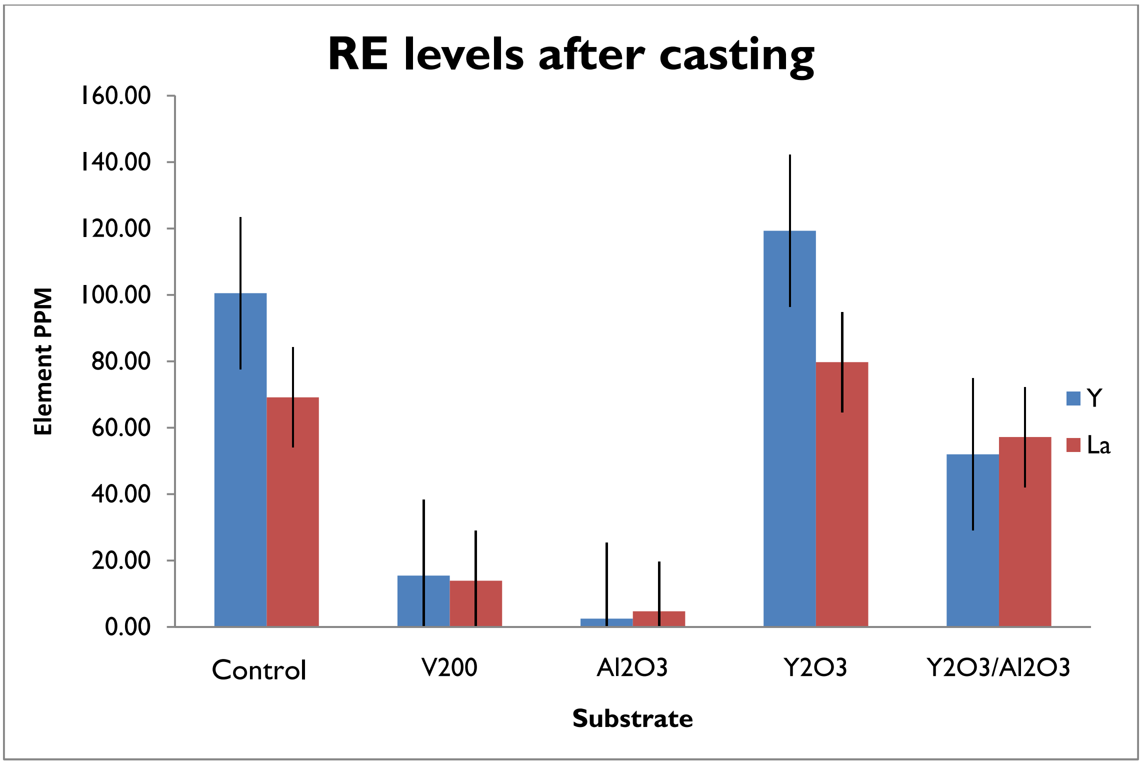

Figure 32: area of eutectic with Y and La quantified by EDS

The fact that the reactive element levels in the sample melted against yttria are higher than in the control (CMSX-4 as received) either shows that there is a large experimental error, or that some yttrium has migrated from the substrate into the alloy. This latter case is unlikely, as yttrium is already present over its solution limit, meaning there is an osmotic pressure out of the alloy, and lanthanum is also present in larger quantities than in the control. Despite the uncertainty, the yttria-containing ceramics have clearly outperformed the silica and alumina substrates in retaining reactive elements in the alloy. Simple thermodynamics would predict reactive element retention in the same order as the Gibbs free energies of formation of the substrates, that is Y_2O_3 > Y_2O_3/Al_2O_3 >Al_2O_3 > SiO_2. The greater retention of reactive elements by SiO_2 than Al_2O_3 indicates either that the thermodynamics are more complex, or that there is a large experimental error.

To give some indication of a trend, the amounts of RE found can be plotted against energies of formation. $-\Delta G_f$ values for each substrate are shown in Table 4. The values have been normalised to the value for V200 to give a comparison with existing core technology. The amounts of total eutectic, yttrium and lanthanum have been normalized to the amount found in the raw alloy.

Table 4: Normalised RE levels

			Relative amount		
Substrate	-ΔGf per mole O_2	Normalised -ΔGf per mole O2	Eutectic	Y	La
V200	574.4	1.00	0.38	0.15	0.20
Alumina	764.6	1.33	0.16	0.02	0.07
Mix	781.2	1.36	0.63	0.52	0.83
Yttria	930.4	1.62	1.37	1.19	1.15

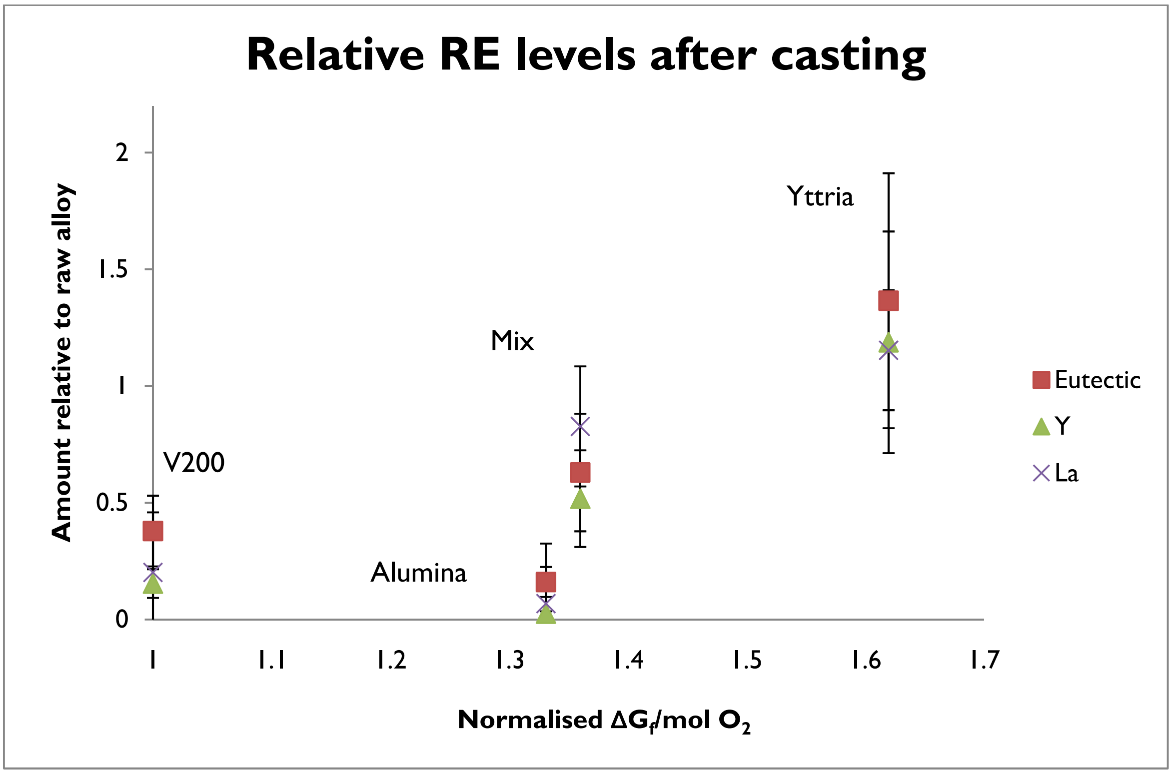

Figure 33: Retention of reactive elements against $-\Delta G_f$ of substrate

When retention of reactive elements is plotted against thermodynamic stability of substrate (Fig. 33), there is a broad correlation indicating that, as may be expected, less of the reactive elements are retained after heating with a more reactive substrate. The values for alumina are anomalously low. This could be due to experimental error, or to the formation of a thermodynamically-favoured mixed oxide such as $YAlO_3$[62].

3.31 Errors in quantification

Error bars for Figs. 31-33 have been calculated using standard error. The method employed to determine concentration has many sources of error, including:

i. Much of the Y and La additions dissolve in the alloy matrix. This technique only measures that which will not dissolve, so all results are an underestimate of the total measurement.
ii. EDS is inaccurate at low concentrations, so there is an error in quantification of the amounts of Y and La in the eutectic.
iii. The eutectic was not easily observed on the microscope used, showing up as a slightly darker shade of grey, so some smaller areas may have been missed.
iv. There is a statistical error involved, as only a small area was scanned compared to the entire surface available, and the whole volume of the drop.
v. Errors are involved in calculating the area of the eutectic phase, as the areas were rarely of a regular shape and their edges not clearly defined.
vi. EDS takes a measurement from an interaction volume which is larger than most of the areas found and penetrates under the surface of the sample.

In the light of all these errors, the technique can only be used to indicate a trend and is not reliable enough to give a true quantitative result. The technique was also laborious and is not recommended for future use.

3.4 Measurement of reactive layers

Full data for the measurement of reactive layers are given in the Appendix. Average thicknesses for each sample are shown in Table 5.

Table 5: Average measured reactive layer thicknesses

Mean interface RL thickness (μm)

1550 °C

Time/mins	5	15	30	60
Al_2O_3	3.07	4.10	8.68	7.29
V200	2.17	3.14	17.87	11.34
Y_2O_3	2.40	1.31	1.36	1.54
Al_2O_3/Y_2O_3	3.68	2.77	8.325	14.22

1500 °C

Time/mins	5	15	30	60
Al_2O_3	2.14	10.75	6.45	9.47
V200	8.20	7.72	9.46	10.34
Y_2O_3	1.28	2.57	1.06	1.57
Al_2O_3/Y_2O_3	2.44	4.37	4.83	9.23

1450 °C

Time/mins	5	15	30	60
Al_2O_3	2.04	2.06	4.03	4.97
V200	3.34	1.96	11.17	9.57
Y_2O_3	0.94	1.08	1.15	1.27
Al_2O_3/Y_2O_3	2.93	2.75	2.62	4.36

Mean free surface RL thickness (μm)

1550 °C

Time/mins	5	15	30	60
Al_2O_3	0.90	0.80	0.88	0.97
V200	0.84	1.09	6.41	0.94
Y_2O_3	1.67	0.79	2.93	1.10
Al_2O_3/Y_2O_3	1.90	1.58	0.88	1.17

1500 °C

Time/mins	5	15	30	60
Al_2O_3	1.22	1.19	2.57	0.42
V200	1.46	1.63	1.13	0.86
Y_2O_3	0.96	0.80	0.87	0.88
Al_2O_3/Y_2O_3	1.00	0.72	1.40	0.71

1450 °C

Time/mins	5	15	30	60
Al_2O_3	1.00	1.28	1.03	1.51
V200	1.26	1.65	0.77	0.89
Y_2O_3	0.80	1.01	0.73	1.34
Al_2O_3/Y_2O_3	2.44	0.69	0.85	0.84

Figs. 34-39 show these thicknesses plotted against time to indicate any reaction layer growth.

Error bars have been calculated using standard error.

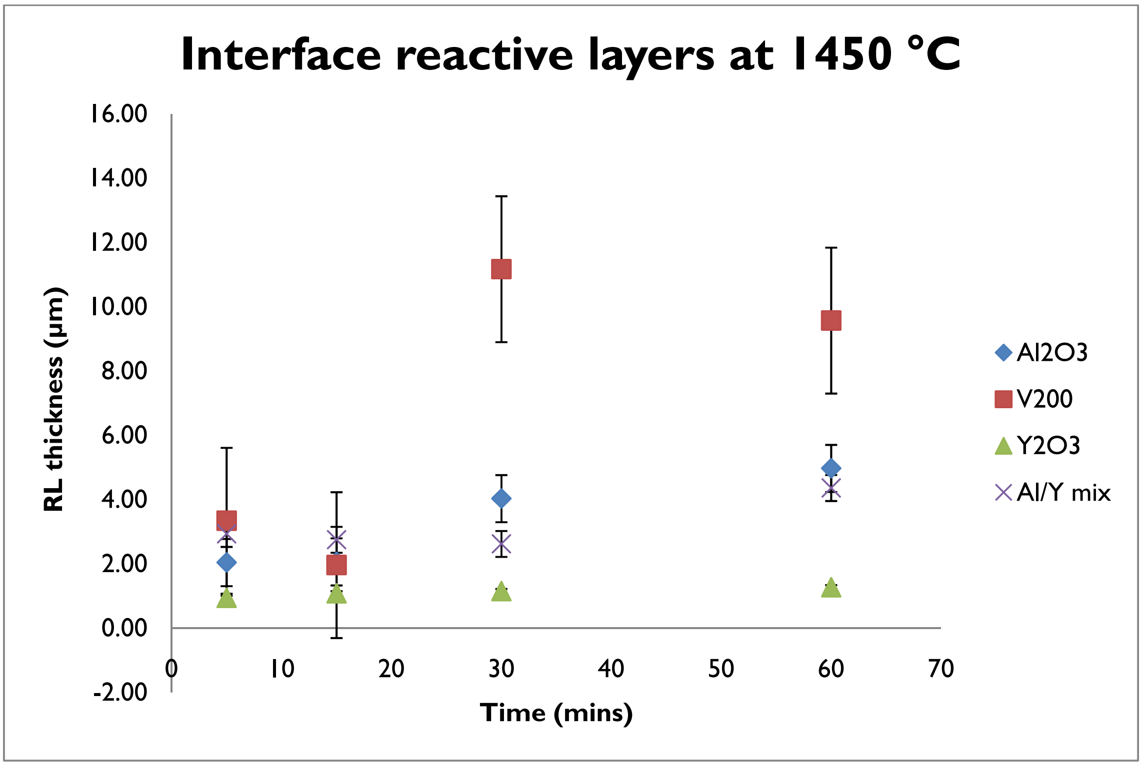

Figure 34: Growth of interface reactive layers at 1450 °C

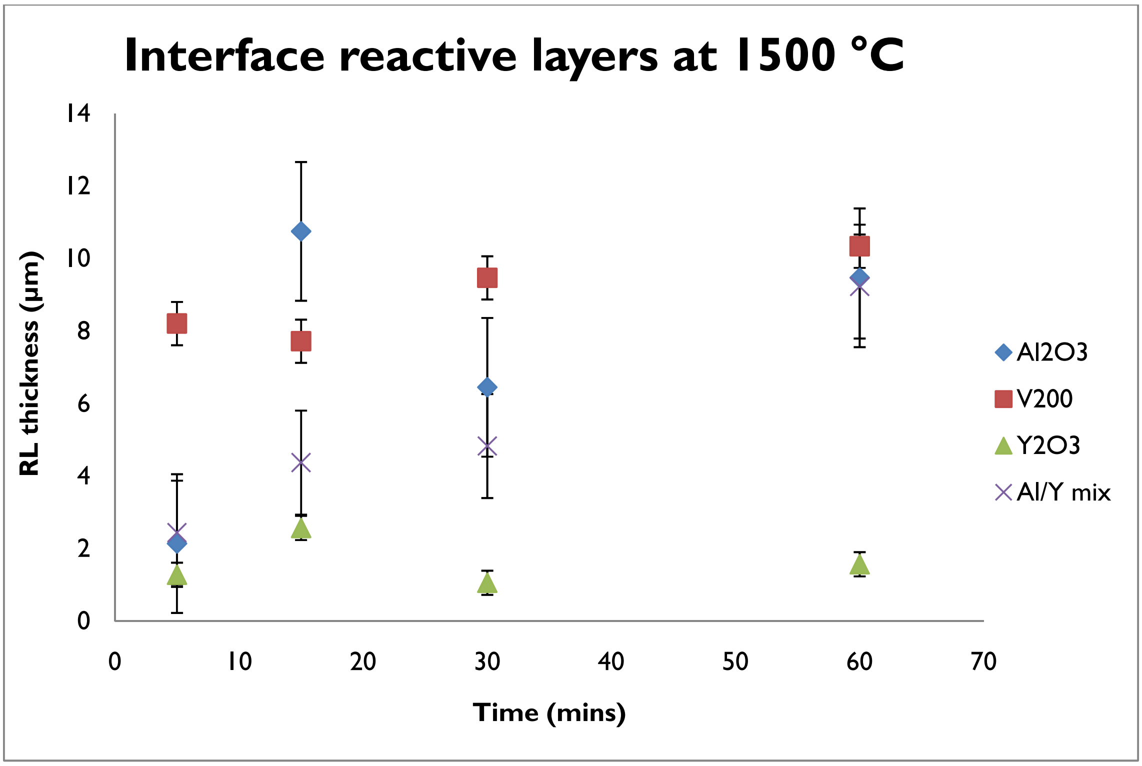

Figure 35: Growth of interface reactive layers at 1500 °C

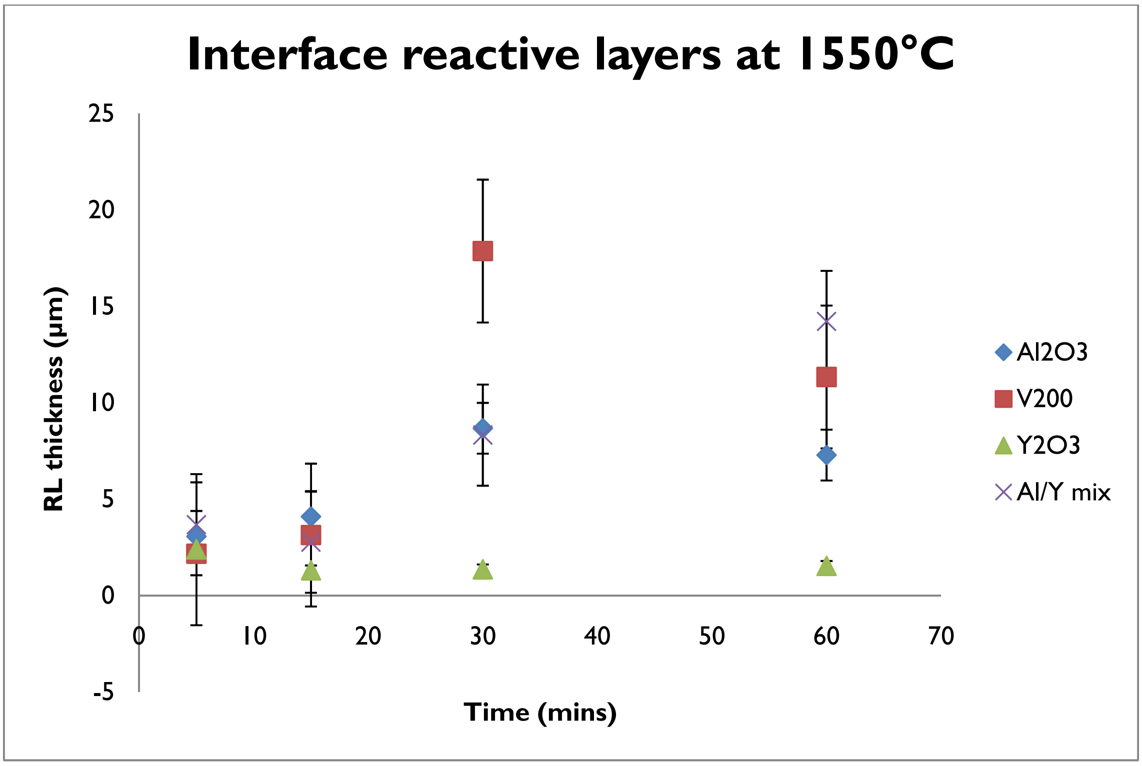

Figure 36: Growth of interface reactive layers at 1550 °C

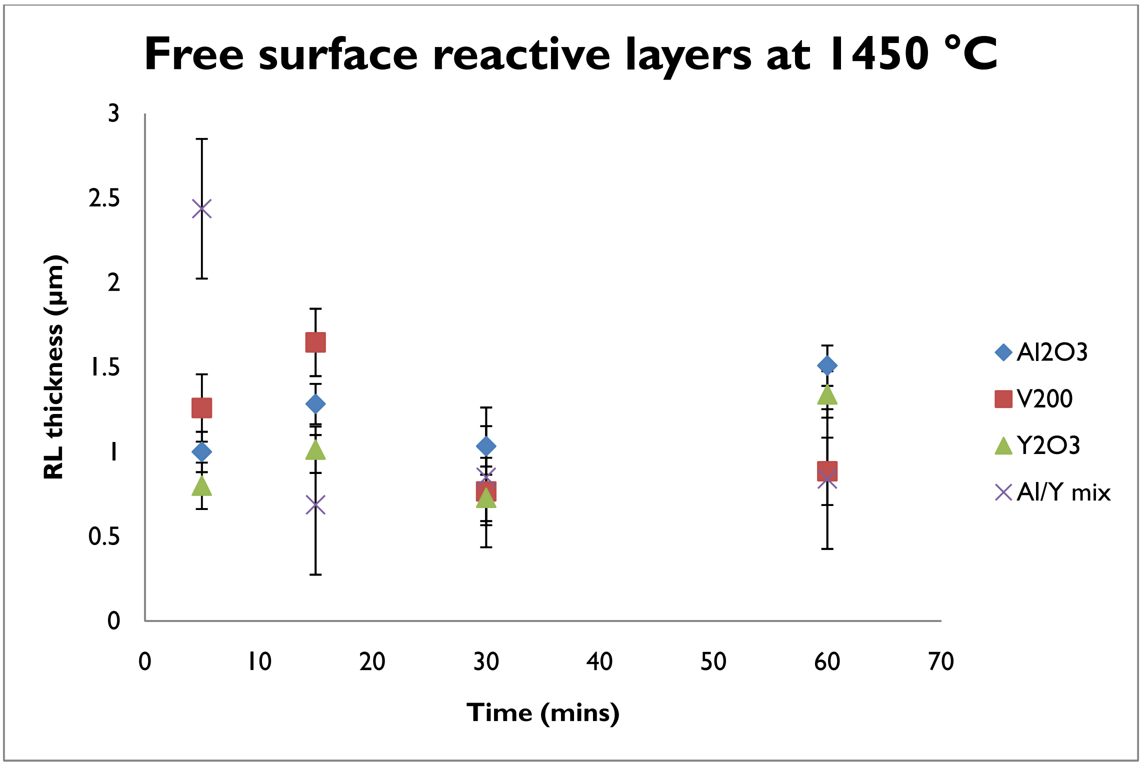

Figure 37: Growth of free surface reactive layers at 1450 °C

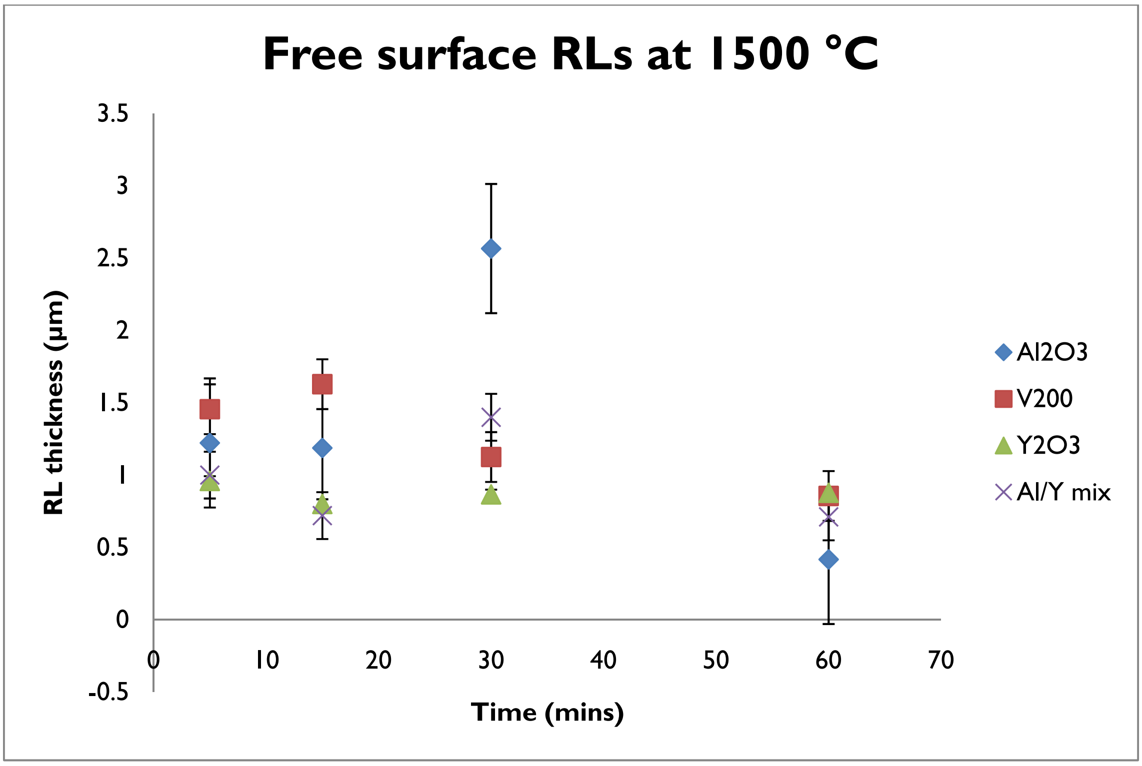

Figure 38: Growth of free surface reactive layers at 1500 °C

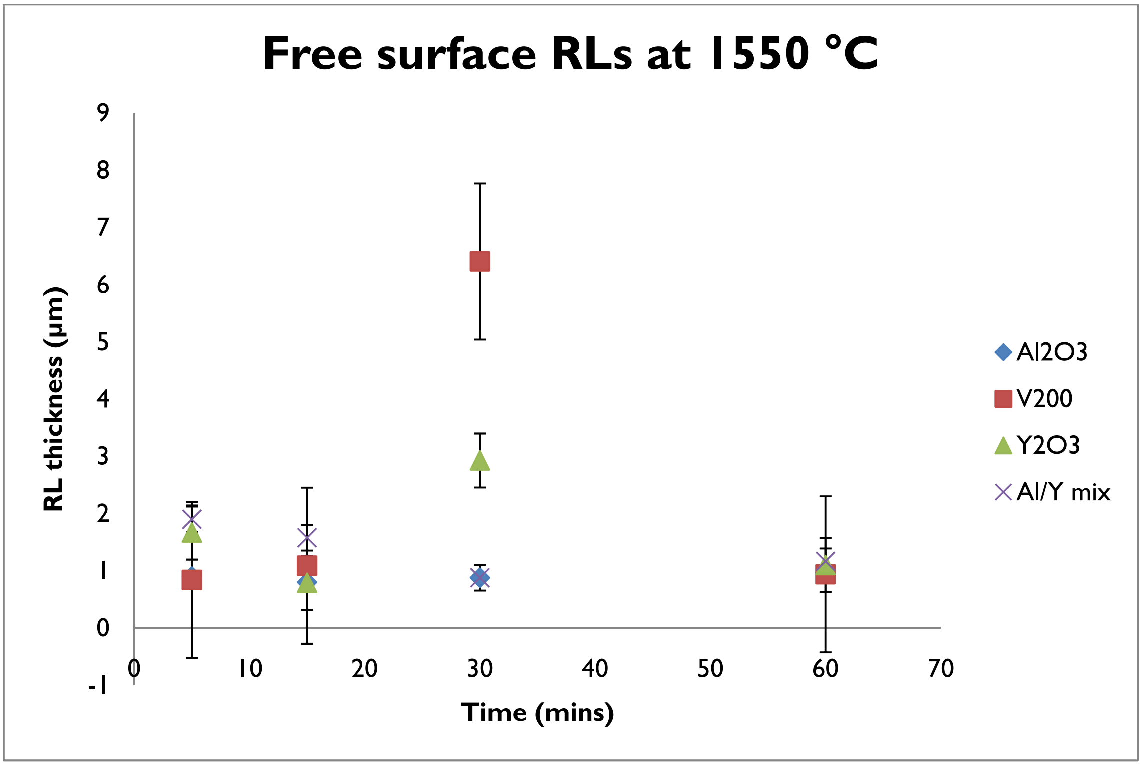

Figure 39: Growth of free surface reactive layers at 1550 °C

Although there is a lot of scatter in the measurements, average interface RL thickness for each sample plotted against time shows steady growth over time for all the substrates except yttria. There may also be slow growth over time at the free surface, although the reactive layer thicknesses appear relatively constant. It is difficult to observe a clear trend here. The vast majority of the measurements at the free surface were between 0.5 and 2 µm.

At the interface, the thickness of the RL varies with substrate in the order SiO_2 >Al_2O_3 > Y_2O_3/Al_2O_3 >Y_2O_3. This is as would be expected from the -$\Delta G_f°$ values for the ceramics and correlates roughly with the result found from the EDS measurements. The discrepancy between the SiO_2 and Al_2O_3 results between the two techniques is likely to indicate a significant error in either or both processes.

The reactive layers formed next to yttria substrates did not grow over time and are of comparable thickness to those formed at the free surface. This indicates that there is no net reaction between CMSX-4 and yttria and any reaction product is from the reduction of the furnace atmosphere and any residual oxygen adsorbed in the system. Yttria would not be expected to react with yttrium or lanthanum as there is no thermodynamic driving force for these reactions, Y_2O_3 having a slightly higher $-\Delta G_f^\circ$ of 1482 kJ mol^{-1} than La_2O_3 at 1370 kJ mol^{-1}. [63]

As well as these thermodynamic considerations, there could be a degree of kinetic control in the reactions leading to RL formation. This means there could be kinetic barriers to reaction which affect RE loss. Section 3.5 attempts to model the reaction kinetics in terms of activation energies.

3.5 Reaction Kinetics

In this analysis it is assumed that there is no contribution from other active metals in the alloy and the reactive layer is formed by the following reactions:

$$2Y + 3[O] \rightarrow Y_2O_3$$

$$2La + 3[O] \rightarrow La_2O_3$$

[O] represents an oxygen species liberated from the ceramic and could be an oxygen radical or a more complex intermediate. For the reaction to proceed, oxygen must be liberated involving partial reduction of the ceramic. The free oxygen species and the reactive metal species must then simultaneously migrate to the boundary of the metal before they can combine.

3.51 Gravimetric analysis

The reactions that form the reactive layer on CMSX-4 have the potential to be very complex, so to simplify the case samples of pure yttrium have been reacted with V200 substrates under the same conditions and the progress of the reaction monitored by gravimetric analysis.

The yttrium samples were heated to 1550 °C and were weighed before and after reaction. Any gain in mass was attributed to the reaction of silica with yttrium:

$4Y + 3SiO_2 \rightarrow 2Y_2O_3 + 3Si$

It was assumed that all the silicon dissolved into yttrium, as the SEM studies (Figs. 19-21) showed the presence of both oxygen and silicon in the drop after reaction. Any evaporation of the sample was ignored, as was diffusion of yttrium into the substrate and any silicon not dissolved in yttrium.

Yield is defined as $\frac{moles\ product\ formed}{moles\ which\ could\ have\ formed\ from\ starting\ materials}$ (eqn. 2)

which in this reaction is equivalent to $\frac{moles\ Y\ in\ product}{moles\ Y\ at\ start}$ (2.1)

$$mols\ Y\ (product) = \frac{2}{3} \times mols\ O$$

(2.2)

$$mols\ O = \frac{M(O)}{M_r(O)}$$

(2.3)

$$M\ (O) = \left(\frac{2\ M_r(O)}{M_r(SiO_2)}\right)(M - M_0)$$

(2.4)

$$mols\ Y\ (start) = \frac{M}{M_r(Y)}$$

(2.5)

$$\text{yield} = \frac{\frac{2\left(\frac{2\ M_r(O)}{M_r(SiO_2)}\right)(M - M_0)}{3M_r(O)}}{\frac{M}{M_r(Y)}}$$

(2.6)

M and M_0 represent final and initial mass of the drop respectively and M_r represents molar mass. Table 6 shows the masses of the drops with yields calculated from equation 2.6. Fig. 40 shows yield plotted against reaction time. Error bars are shown with standard error.

Table 6: Gravimetric analysis of the oxidation of Y by V200

t/min	M_0	M	Moles Y (Start)	moles Y (Prod)	moles Y unreacted	% yield
1	1.200	1.229	0.013	0.001	0.013	4.8
2	1.237	1.299	0.014	0.001	0.013	9.9
5	1.334	1.482	0.015	0.003	0.012	21.9
8	1.404	1.513	0.016	0.002	0.013	15.3
10	1.270	1.382	0.014	0.002	0.012	17.4
12	1.125	1.228	0.013	0.002	0.010	18.1

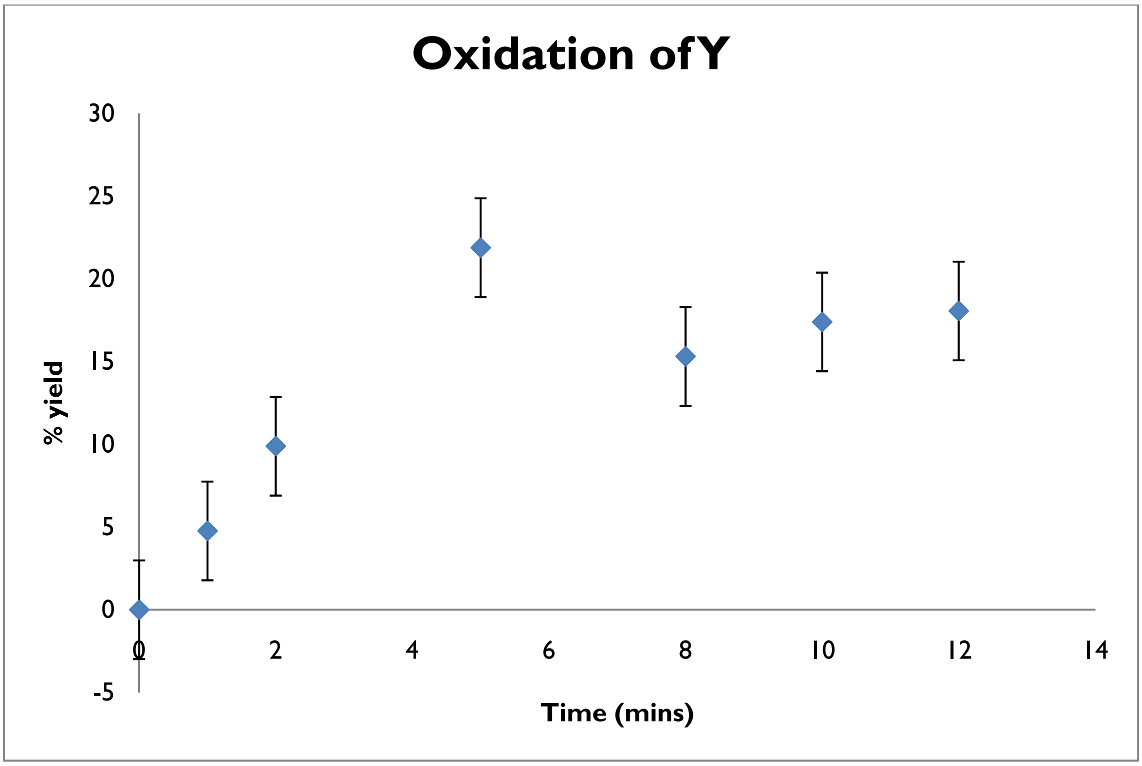

Figure 40: Gravimetric analysis of the reaction of yttrium with V200

Plotting these yields as percentages against reaction time shows a slight decrease in reaction rate over time as reactants are consumed. The outlying point at 5 mins is attributed to the greater spreading of this drop than the others giving a greater surface area for reaction.

The rate equation for the reaction is

$$\frac{d[Y_2O_3]}{dt} = k[Y]^m[SiO_2]^n$$

(eqn. 3)

where m and n are the orders of reaction in Y and SiO_2 respectively and k is the rate constant. At the reaction interface, it can be assumed that both reactants are in excess and the steady state approximation[64] can be used. This means that the concentrations of any intermediates do not change and an overall reaction order can be calculated from

$$\frac{d[A]}{dt} = k[A]^i$$

(eqn. 4)

where A represents all reactants. Integrating this rate law over the course of the reaction will allow a graph to be plotted from which the order and rate constant can be calculated.

$$\frac{d[A]}{[A]^i} = kdt$$

(4.1)

$$\int_{[A]_0}^{[A]} \frac{d[A]}{[A]^i} = \int_{t_0}^{t} kdt$$

(4.2)

$$\left[\frac{[A]}{[A]^{i-1}}\right]^{[A]_0} - \left[\frac{[A]}{[A]^{i-1}}\right]^{[A]} = -kt$$

(4.3)

$$\frac{1}{{[A]_0}^{i-1} - [A]^{i-1}} = -kt$$

(4.4)

for i > 1. For i=1 the integral is

$\ln[A]_0 - \ln[\mathrm{A}] = -kt.$

(4.5)

Let $y = \frac{1}{[A]_0{}^{i-1} - [A]^{i-1}}$ for i≠1 and $y = \ln[A] - \ln[A]_0$ for i=1. From the above analysis, a plot of y against t should be a straight line of gradient –k. A trial and error technique can be used to estimate i, whereby values of y are calculated for different values of i and t. The value of i for which a plot of y against t gives the closest fit to a straight line is the closest approximation to the real order of reaction. Values of -y for various i are calculated in table 7. [A] is taken to be the moles of Y remaining unreacted, where $[A]_0$ is the moles of Y in the drop before reaction. The values are normalised to the value at t=1 min to allow them to be plotted together. The normalised values are plotted against t in Fig. 41.

Table 7: Calculated definite integrals for orders of reaction up to 4

Integrated Rate Laws

	i=0		i=0.5		i=1		i=1.5	
Time	$1/A^{-1}-1/A_0^{-1}$		$1/A^{-0.5}-1/A_0^{-0.5}$		$\ln(A/A_0)$		$1/A^{4}-1/A_0^{4}$	
(mins)		normalised		normalised		normalised		normalised
1	0.00	1.00	0.00	1.00	-0.049	1.00	0.21	1.00
2	0.00	2.14	-0.01	2.13	-0.104	2.13	0.45	2.13
8	0.00	3.76	-0.01	3.58	-0.166	3.40	0.69	3.24
10	0.00	3.86	-0.01	3.89	-0.191	3.91	0.84	3.94
12	0.00	3.55	-0.01	3.80	-0.199	4.08	0.93	4.37

	i=2		i=2.5		i=3		i=4	
Time	$1/A-1/A_0$		$1/A^{1.5}-1/A_0^{1.5}$		$1/A^{2}-1/A_0^{2}$		$1/A^{3}-1/A_0^{3}$	
(mins)		normalised		normalised		normalised		normalised
1	3.71	1.00	48.48	1.00	563	1.00	6.42E+04	1.00
2	7.89	2.13	103.00	2.12	1196	2.12	1.36E+05	2.12
8	11.45	3.09	142.71	2.94	1582	2.81	1.64E+05	2.56
10	14.75	3.98	194.48	4.01	2282	4.05	2.66E+05	4.14
12	17.42	4.70	244.67	5.05	3057	5.43	4.04E+05	6.29

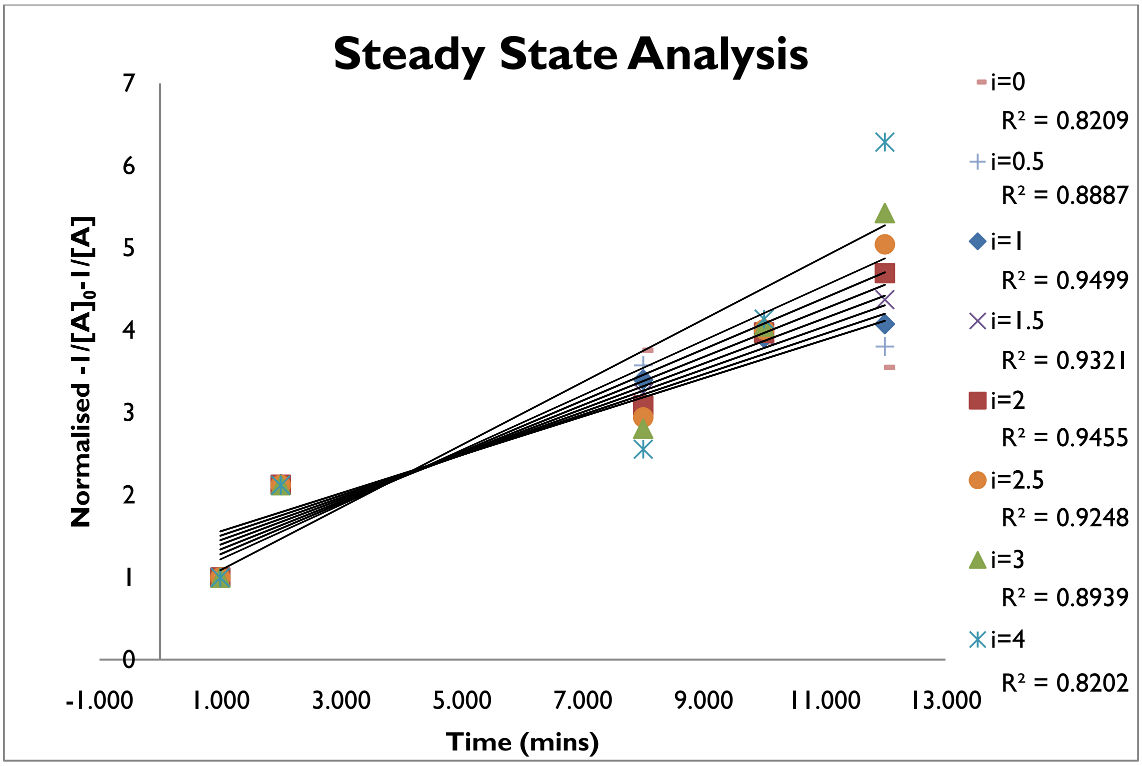

Figure 41: Integrated rate laws plotted against time

For each value of i, the plot of y against t has been fitted to a straight line. The R^2 value indicates how well the data fit the line, with 1 being a perfect fit and 0 being complete scatter. Ignoring the outlying point at 5 mins, the order of reaction which gives the line of best fit is i=1. The R^2 value for i=2 is very similar, meaning that second-order kinetics are a possibility. First-order kinetics mean that one step in the reaction is rate-limiting, while second-order indicates multiple rate-limiting steps. The rate-limiting step here could be the breaking of the bonds in the substrate lattice, or the diffusion of silica into yttrium. From first principles the CMSX-4 reaction is more likely to be diffusion-limited, with the rate-limiting step being the migration of La and Y through the alloy to the interface for reaction.

3.52 Activation Energies

Activation energy for a reaction can be estimated from the change in reaction rate with temperature using the Arrhenius equation[65]

$$\mathrm{k} = \mathrm{Ae}^{-\mathrm{Ea/RT}}$$

(eqn. 5)

where A is the pre-exponential factor (theoretical activity at infinite temperature), Ea is activation energy, R is the ideal gas constant, T is temperature and k is the rate constant.

Taking the formation of the reaction layer on CMSX-4 as a single reaction and assuming the reaction rate is diffusion-limited, pseudo-first order kinetics can be applied. This assumes that the substrate is in excess (i.e. there is always some available to react) and the only rate-limiting factor is migration of reactive elements to the interface. The rate equation at steady state is

$$\frac{d(RL)}{dt} = \frac{d[A]}{dt} = k[A]dt$$

(4.6)

The integrated rate law is

$$\ln[A] - \ln[A]_0 = kt$$

(4.7)

The rate of consumption of reactants is equal to the rate of product formation, so reaction layer thicknesses can be used in place of [A] to find k. Taking [A] to be the RL thickness at time t, and $[A]_0$ to be zero, it follows from equation 4.7 that a plot of ln [A] against t will have a gradient equal to k.

Calculated values for ln (RL thickness) are shown in Table 8. These values are plotted against time in Figs. 42-45.

Table 8: Calculated rate law integrals for each substrate

Al2O3		ln(RL thickness)		
t/mins	5	15	30	60
1450	0.71	0.72	1.39	1.60
1500	0.76	2.37	1.86	2.25
1550	1.12	1.41	2.16	1.99

V200		ln(RL thickness)		
t/mins	5	15	30	60
1450	1.21	0.67	2.41	2.26
1500	2.11	2.04	2.25	2.34
1550	0.77	1.14	2.88	2.43

Y2O3		ln(RL thickness)		
t/mins	5	15	30	60
1450	-0.06	0.08	0.14	0.24
1500	0.25	0.94	0.06	0.45
1550	0.88	0.27	0.31	0.43

Al/Y mix		ln(RL thickness)		
t/mins	5	15	30	60
1450	1.08	1.01	0.96	1.47
1500	0.89	1.48	1.57	2.22
1550	1.30	1.02	2.12	2.65

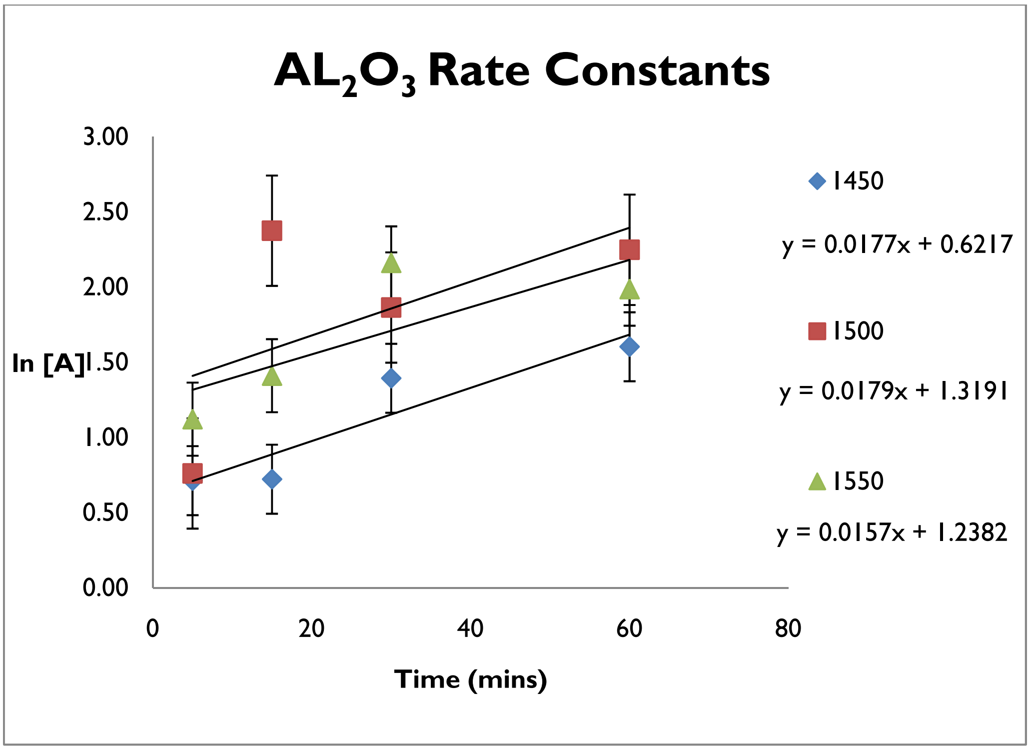

Figure 42: Integrated rate law plot for Al_2O_3

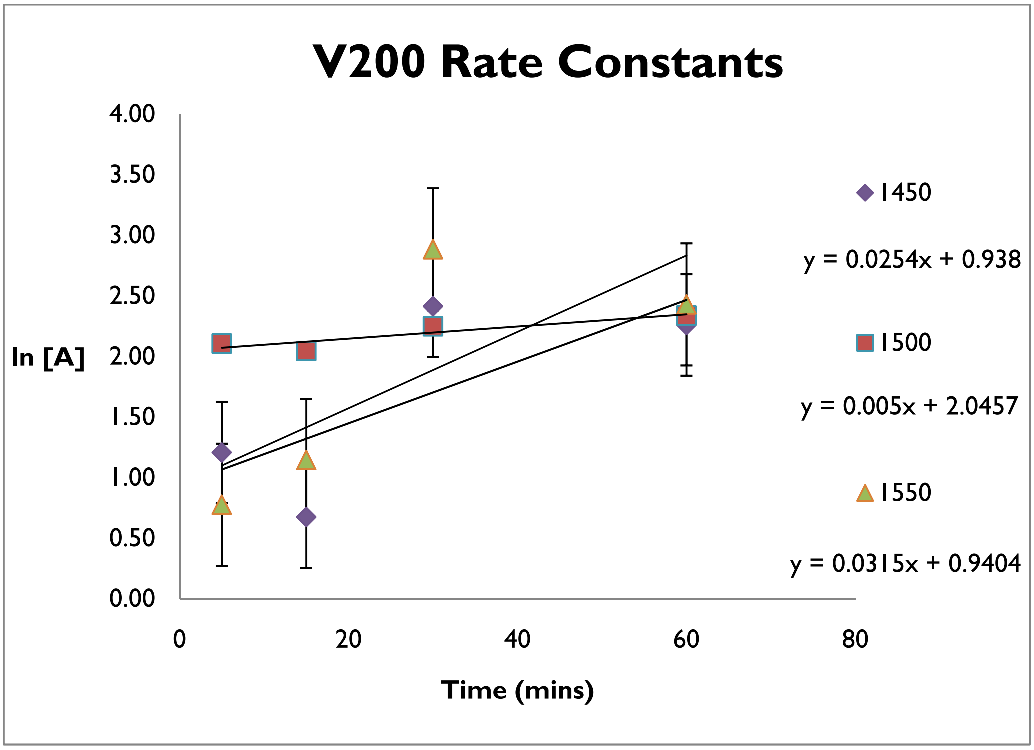

Figure 43: Integrated rate law plot for V200

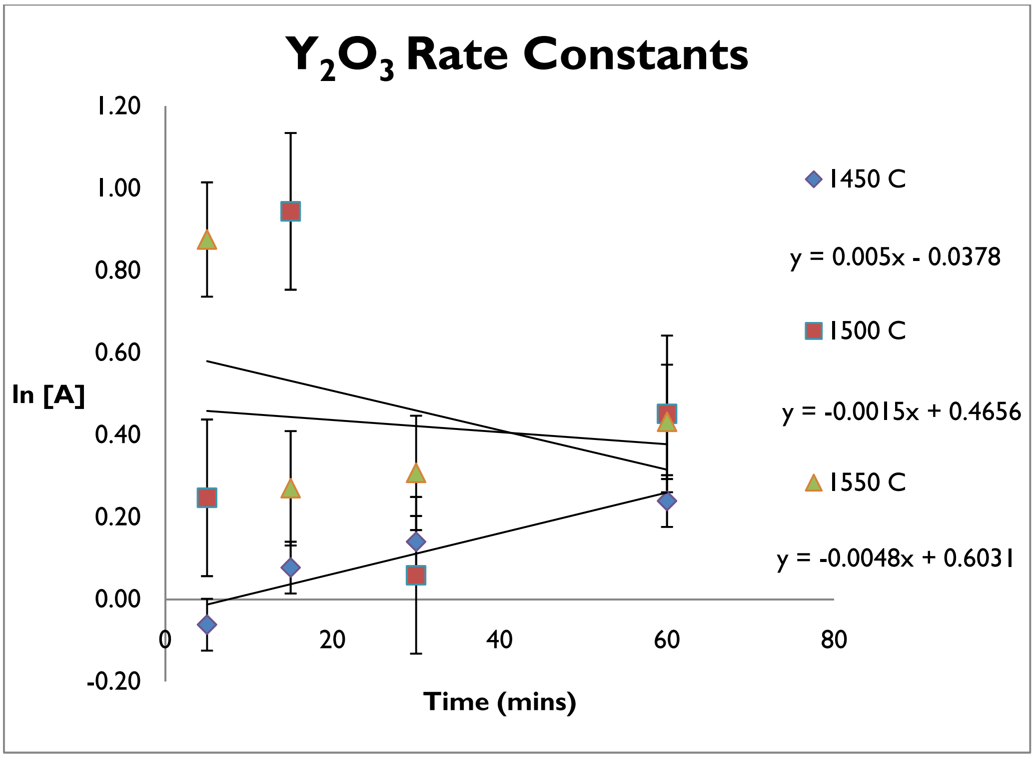

Figure 44: Integrated rate law plot for Y_2O_3

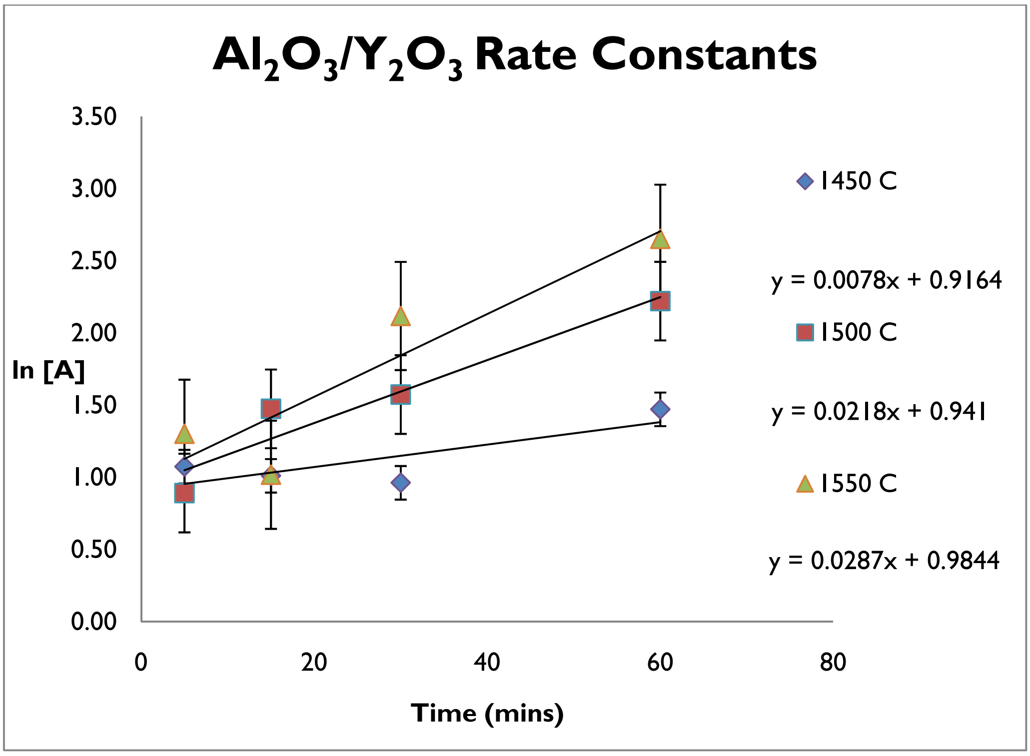

Figure 45: Integrated rate law plot for Al_2O_3/Y_2O_3 mix

Values of k are taken as the gradients of these graphs. According to equation 5, a plot of ln k against ln 1/RT will have a gradient equal to -Ea. This plot is shown as Fig. 46, from the data in Table 9.

Table 9: Rate constants

		Al2O3		V200		Y2O3		Al/Y mix	
T	1/RT	k	ln k	k	ln k	k	ln k	k	ln k
1450	8.3E-05	1.8E-02	-4.03	2.5E-02	-3.67	5.0E-03	-5.30	7.8E-03	-4.85
1500	8.0E-05	1.8E-02	-4.02	5.0E-03	-5.30	-1.5E-03		2.2E-02	-3.83
1550	7.8E-05	1.6E-02	-4.15	3.2E-02	-3.46	-4.8E-03		2.9E-02	-3.55

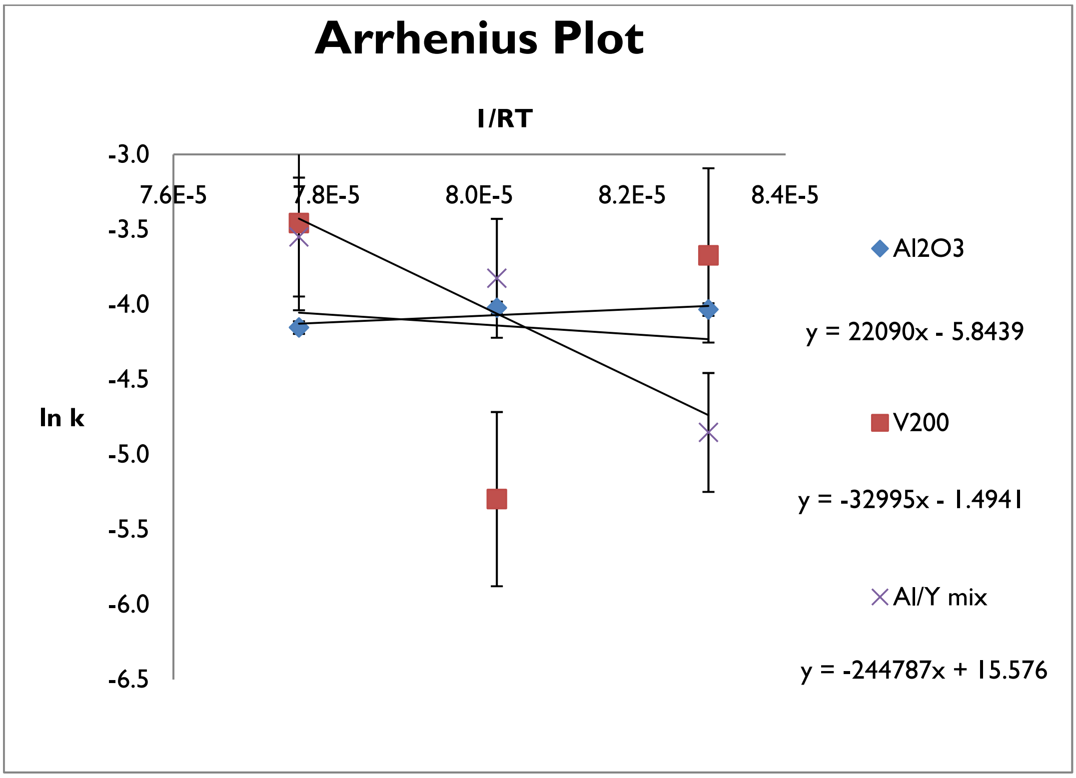

Figure 46: Activation energy plots using the Arrhenius parameters

Values for Y_2O_3 could not be plotted as the calculated rate constants are negative at two temperatures i.e. the RL gets thinner over time. This factor is another indication that there is no reaction leading to the growth of a reactive layer between CMSX-4 and the yttria substrate.

Fig. 46 gives an activation energy for the formation of the reactive layer with alumina of -22 kJ mol^{-1}, with V200 (silica) of 33 kJ mol^{-1} and with the alumina/yttria mix of 244 kJ mol^{-1}. The degree of scatter in the V200 results and the negative activation energy (which is impossible) found for alumina indicate that these results are not reliable. It could be argued from these results that the higher activation energy found for the alumina/yttria mix than V200 indicates a larger barrier to reaction and thus a degree of kinetic control in the reaction, however this is a very tenuous point considering the degree of spread in the data.

Another possibility is that the reaction rate is so limited by diffusion that it is not significantly dependent on temperature at the timescales and temperature ranges considered here.

3.53 Errors in kinetic analysis

There are several sources of error in the process including:

i. Errors in reactive layer measurement. The RL was found to vary in thickness across a sample, which leads to significant statistical error. Many areas were left unmeasured due to the boundaries being indistinct. Each sample was only cut once; the thickness of the observed RL may vary depending on whether the drop was cut straight through the centre or slightly away.

   The reasons for this non-uniform behaviour are unclear: some of the RL may have been lost during handling, or during mounting due to the pressure exerted by the Bakelite press. The RL may also grow unevenly; this could be due to roughness in the surface of the substrate or to uneven diffusion of reactive elements to the surface of the metal. The RL may also be compressed and folded, or fall off, as the drop shrinks on cooling. The amounts of reaction products formed would be more accurately measured by the total volume of reaction layer, however this quantity is difficult to measure due to uneven RL growth.

ii. Errors in gravimetric analysis. The effect of drop spreading was ignored apart from one outlying point. Evaporation of the drop was ignored. It was assumed that all the silicon in the silica which reacted dissolved in the drop and all the yttrium remained in the drop.

iii. Errors in the steady state analysis. There is uncertainty in the order of reaction, and this may have been calculated from inaccurate data. The order of reaction was only fitted to the nearest 0.5 – repeated iteration would give a more precise result, assuming that the original data was accurate.

iv. Simplification of the model. Formation of the reactive layer was attributed only to oxidation of lanthanum and yttrium and the process modelled as only one reaction. There are more reactions taking place simultaneously and all these reactions may have complex mechanisms, meaning that RL growth may not correlate well with rate of loss of Y/La. Pseudo-first order kinetics may not apply to the growth of the RL as a whole, even if they can be applied to the reaction forming yttrium and lanthanum oxides within the RL.

v. The temperature dependence of reaction rate may not be significant at the reaction times and temperatures used, meaning that activation energies cannot be calculated accurately from the Arrhenius equation under these conditions.

In light of these considerations, it is unclear whether any trend can be drawn from the above data. More repeats must be taken at a greater number of reaction times to lessen the effect of scatter in the results, and the correct order of reaction for Y/La reacting in CMSX-4 found. It could also be the case that differences in activation energies between substrates have little effect on the rates of growth of the reactive layers studied here.

4. Conclusions and Future Work

4.1 Summary of Results

Several core formulations have been investigated to see whether their chemistry has any effect on the loss of yttrium and lanthanum dopants from CMSX-4 superalloy in a simulated casting procedure.

Using EDS, the Y and La inclusions were found to exsolve together above their dissolution limits as a low melting point eutectic. This eutectic phase was found in similar quantities after heating with yttria to those found in the raw alloy. Lower quantities were found after heating with silica and alumina ceramics, with a mixed alumina-yttria substrate was found to retain levels in between yttria and silica.

Reactive layers of Y and La oxides were found to form on the surface of the metal drops tested after melting. Thin layers were found at the free surface, while at the metal-ceramic interface the layers were thicker and found to grow with increased reaction time. The thickness of the reaction layer was linked to the thermodynamic stability of the ceramic substrate, with yttria appearing unreactive and thicker reactive layers forming with ceramics of lower Gibbs free energies of formation.

By gravimetric analysis, the oxidation of yttrium by a predominantly silica substrate appeared to show first-order kinetics. Based on the same kinetic model, activation energies were calculated for the formation of the reactive layer with each substrate tested. These values were too unreliable to draw any definite results from.

4.2 Conclusions

In light of these results, it can be concluded that the chemistry of core ceramics does indeed have a significant effect on the loss of reactive elements from superalloys in a casting environment. The major mechanism of this loss appears to be by reaction with the ceramic. There may also be a small contribution from evaporation.

The thermodynamic stability of the ceramic is the main factor that has been found to affect Y/La retention in the alloy, with higher ceramic $-\Delta G_f$ values leading to a greater degree of retention. No reactive element loss was observed using yttria substrates, while the addition of 10 % yttria to an alumina substrate improved reactive element retention. The adaptation of existing core formulations to include yttria is thus recommended.

4.3 Future Work

There was a large degree of experimental error in all the results in the study. To reduce these errors, the experiment could be repeated at each time and temperature used and for different reaction times, but the time limits imposed have prevented this. A larger area could be scanned to reduce statistical error in the EDS measurements, and all these measurements could be repeated on a microscope with higher resolution to improve identification and measurement of the eutectic phase.

The use of larger metal drops would decrease their surface area: volume ratio, lessening the effect of drop shrinkage on the reactive layer and allowing a more reliable measurement of reactive layer thickness due to the larger reactive layer formed.

Cutting the drops at several places across their width would allow a more comprehensive RL measurement, although this would be difficult with the size of drops employed here.

A system whereby the metal-ceramic couple could be kept together after melting and cooling would remove any errors due to the reactive layer being lost during handling and mounting. This would preserve the integrity of the entire reactive layer and allow any effects on RL growth due to the surface morphology of the substrate to be studied. A possible system would be to use an injected boat instead of a flat substrate, then cut and mount the metal and ceramic together.

The use of ICP-MS would verify the results found with EDS, and would likely give a more reliable result.

Investigating the use of a mixed silica-yttria ceramic is recommended, as this could combine existing core technology with the lower reactivity of yttria.

It would be useful to measure the contact angles of the drops to see if their wetting behaviour has any correlation with La/Y loss.

Repeating the results in a furnace capable of achieving the higher vacuum levels used in industry could affect the data, and so should be evaluated.

Creating a fully enclosed system would more closely emulate the industrial system and would remove any effects of having a large free surface. For example, using an injected cup shaped crucible with a lid would eliminate the free surface.

To calculate the activation energies correctly, a more accurate way of finding orders of reaction for the formation of the reactive layer must be used. This could be done by monitoring the change in concentration of Y and La in the bulk metal over time using ICP-MS.

5. References

---

[1] 'Carnot Cycle - Engineers Edge' <http://www.engineersedge.com/thermodynamics/carnot_cycle.htm> [accessed 26 September 2010].

[2] D. P. Whittle and J. Stringer, 'Improvements in High Temperature Oxidation Resistance by Additions of Reactive Elements or Oxide Dispersions', *Philosophical Transactions of the Royal Society of London. Series A, Mathematical and Physical Sciences*, 295 (1980), 309 -329 <doi:10.1098/rsta.1980.0124>.

[3] D. A. Ford, 'Future Trends in Investment Casting – Drivers for Development', in (presented at the World Technical Forum, Brno, 2009) <http://www.google.co.uk/search?q=ford+future+trends+in+investment+casting&ie=utf-8&oe=utf-8&aq=t&rls=org.mozilla:en-GB:official&client=firefox-a> [accessed 26 September 2010].

[4] D. A. Ford, K. P. L. Fullagar, H. K. Bhangu, M. C. Thomas, P. S. Burkholder, P. S. Korinko, K. Harris, J. B. Wahl, 'Improved Performance Rhenium Containing Single Crystal Alloy Turbine Blades Utilizing PPM Levels of the Highly Reactive Elements Lanthanum and Yttrium', *Journal of Engineering for Gas Turbines and Power*, 121 (1998), 138-143.

[5] David V. Ragone, *Thermodynamics of Materials* (John Wiley & Sons Inc, 1995).

[6] D. A. Ford, K. P. L. Fullagar, H. K. Bhangu, M. C. Thomas, P. S. Burkholder, P. S. Korinko, K. Harris, J. B. Wahl, 138-143.

[7] S.R. Taylor, 'Abundance of Chemical Elements in the Continental Crust: A New Table', *Geochimica Et Cosmochimica Acta*, 28 (1964), 1273-1285 <doi:doi: DOI: 10.1016/0016-7037(64)90129-2>.

[8] 'Metal-Pages - Rare Earths Prices', 2010 <http://www.metal-pages.com/metalprices/rareearths/> [accessed 15 September 2010].

[9] T. M. Simpson and A. R. Price, 'Oxidation Improvements of Low Sulfur Processed Superalloys', in *Superalloys 2000* (presented at the 9th International Symposium on Superalloys, Champion, PA, USA, 2000), pp. 387-392.

[10] P. Withey, 'Private Correspondance'.

[11] Roger C. Reed, *The Superalloys: Fundamentals and Applications*, 1st edn (Cambridge University Press, 2008).

[12] Tanaka Ryohei, 'Niobium-Base Superalloys. The Backgrounds and Realization of High Strength Alloy.', *Metals Sciece & Technology*, 76 (2006), 153-160.

[13] H. T. Lee and S. W. Lee, 'The Morphology and Formation of Gamma Prime in Nickel-Base Superalloy', *Journal of Materials Science Letters*, 9 (1990), 516-517 <doi:10.1007/BF00725861>.

[14] R. W. Broomfield, D. A. Ford, J. K. Bhangu, M. C. Thomas, D. J. Frasier, P. S. Burkholder, K. Harris, G. L. Erickson, J. B. Wahl, 'Development and Turbine Engine Performance of Three Advanced Rhenium Containing Superalloys for Single Crystal and Directionally Solidified Blades and Vanes', *Journal of Engineering for Gas Turbines and Power*, 120 (1998), 595.

[15] E. Ricci, D. Giuranno, R. Novakovic, T. Matsushita, S. Seetharaman, R. Brooks, L. A. Chapman, P. N. Quested, 'Density, Surface Tension, and Viscosity of CMSX-4® Superalloy', *International Journal of Thermophysics*, 28 (2007), 1304-1321 <doi:10.1007/s10765-007-0257-0>.

[16] B. Laux, S. Piegert and J. Rosler, 'Advanced Braze Alloys for Fast Epitaxial High-Temperature Brazing of Single-Crystalline Nickel-Base Superalloys', *Journal of Engineering for Gas Turbines and Power*, 132 (2010), 032101-7 <doi:10.1115/1.3159376>.

---

[17] L. Felberbaum and others, 'Thermal Fatigue of Single-Crystalline Superalloy CMSX-4®: A Comparison of Epitaxial Laser-Deposited Material with the Base Single Crystal', *Materials Science and Engineering A*, 299 (2001), 152-156 <doi:10.1016/S0921-5093(00)01378-2>.

[18] Fred R. Sias, *Lost-Wax Casting: Old, New, and Inexpensive Methods* (Woodsmere Press, 2006).

[19] S. Jones and C. Yuan, 'Advances in Shell Moulding for Investment Casting', *Journal of Materials Processing Technology*, 135 (2003), 258-265 <doi:10.1016/S0924-0136(02)00907-X>.

[20] Dorian M. Hatch and Subrata Ghose, 'The α-β Phase Transition in Cristobalite, SiO2', *Physics and Chemistry of Minerals*, 17 (1991), 554-562.

[21] Beebhas C. Mutsuddy and Renée G. Ford, *Ceramic Injection Molding* (Chapman and Hall, 1995).

[22] Y. Li, B. Huang and X. Qu, 'Viscosity and Melt Rheology of Metal Injection Moulding Feedstocks', *Powder Metallurgy*, 42, 86-90.

[23] J.P. Kruth, 'Material Incress Manufacturing by Rapid Prototyping Techniques', *CIRP Annals - Manufacturing Technology*, 40 (1991), 603-614 <doi:10.1016/S0007-8506(07)61136-6>.

[24] M.J. Edirisinghe and J.R.G. Evans, 'Review: Fabrication of Engineering Ceramics by Injection Moulding. I. Materials Selection', *International Journal of High Technology Ceramics*, 2 (1986), 1-31 <doi:10.1016/0267-3762(86)90002-0>.

[25] Z. P. Xie, Y. Huang and J. G. Wu, 'Effects of Powder Characteristics and Grinding Processes on Fluidity of Ceramic Injection Moulding Mixtures', *Journal of Materials Science Letters*, 14 (1995), 1165-1167 <doi:10.1007/BF00423394>.

[26] O. Draper, S. Blackburn, G. Dolman, K. Smalley, A. Griffiths, 'A Comparison of Paste Rheology and Extrudate Strength with Respect to Binder Formulation and Forming Technique', *Journal of Materials Processing Technology*, 92-93 (1999), 141-146 <doi:doi: DOI: 10.1016/S0924-0136(99)00160-0>.

[27] T. Zhang, S. Blackburn and J. Bridgwater, 'The Orientation of Binders and Particles During Ceramic Injection Moulding', *Journal of the European Ceramic Society*, 17 (1997), 101-108 <doi:10.1016/S0955-2219(96)00070-2>.

[28] M. Trunec and J. Cihlár, 'Thermal Debinding of Injection Moulded Ceramics', *Journal of the European Ceramic Society*, 17 (1997), 203-209 <doi:10.1016/S0955-2219(96)00108-2>.

[29] B. A. Pint, 'Progress in Understanding the Reactive Element Effect Since the Whittle and Stringer Literature Review', in *John Stringer Symposium on High Temperature Corrosion: Proceedings from Materials Solutions Conference 2001, 5-8 November 2001,* (Indianapolis, IN, USA, 2003), p. 9.

[30] Whittle and Stringer, 309 -329.

[31] James L. Smialek and Gregory N. Morscher, 'Delayed Alumina Scale Spallation on Rene'N5+Y: Moisture Effects and Acoustic Emission', *Materials Science and Engineering A*, 332 (2002), 11-24 <doi:10.1016/S0921-5093(01)01712-9>.

[32] A. Funkenbusch, J. Smeggil and N. Borstein, 'Reactive Element-Sulfur Interaction and Oxide Scale Adherence', *Metallurgical and Materials Transactions A*, 16 (1985), 1164-1166 <doi:10.1007/BF02811687>.

[33] J. Jedlinski, G. Borchardt, M. Konopka, M. Nocun, 'The Effect of Reactive Elements on the Oxidation Behaviour of Fe23Cr5Al Alloys at High Temperatures : I. Kinetics and Thermal Cycling', *Solid State Ionics*, 101-103 (1997), 1147-1155 <doi:10.1016/S0167-2738(97)00302-0>.

[34] B.G. Mendis, K. J. T Livi, K. J. Hemker, 'Observations of Reactive Element Gettering of Sulfur in Thermally Grown Oxide Pegs', *Scripta Materialia*, 55 (2006), 589-592 <doi:10.1016/j.scriptamat.2006.06.017>.

---

[35] H. M. Tawancy, 'On the Role of Yttrium During High-Temperature Oxidation of an Ni-Cr-Al-Fe-Y Alloy', *Metallurgical Transactions A*, 22 (1991), 1463-1465 <doi:10.1007/BF02660678>.

[36] D. G. Lees, 'The Influence of Sulphur on the Adhesion and Growth Mechanisms of Chromia and Alumina Scales Formed at High Temperatures: The 'sulphur Effect'', *Proceedings of the Royal Society of London. Series A: Mathematical, Physical and Engineering Sciences*, 459 (2003), 1459 -1466 <doi:10.1098/rspa.2002.1107>.

[37] P. Y. Hou and J. Stringer, 'The Effect of Reactive Element Additions on the Selective Oxidation, Growth and Adhesion of Chromia Scales', *Materials Science and Engineering A*, 202 (1995), 1-10 <doi:10.1016/0921-5093(95)09798-8>.

[38] K. Higuchi, H-J. Fecht and R. K. Wunderlich, 'Surface Tension and Viscosity of the Ni-Based Superalloy CMSX-4 Measured by the Oscillating Drop Method in Parabolic Flight Experiments', *Advanced Engineering Materials*, 9 (2007), 349-354 <doi:10.1002/adem.200600277>.

[39] Susan B. Sinnott and Elizabeth C. Dickey, 'Ceramic/Metal Interface Structures and Their Relationship to Atomic- and Meso-Scale Properties', *Materials Science and Engineering: R: Reports*, 43 (2003), 1-59 <doi:10.1016/j.mser.2003.09.001>.

[40] N. Frage, N. Froumin, M. Aizenshtein, L. Kutsenko, D. Fuks and M. P. Dariel, 'Reactive Wetting in Titanium Carbide/Non-Reactive Metal Systems', *Current Opinion in Solid State and Materials Science*, 9, 189-195 <doi:10.1016/j.cossms.2006.02.008>.

[41] Girish Kumar and K. Narayan Prabhu, 'Review of Non-Reactive and Reactive Wetting of Liquids on Surfaces', *Advances in Colloid and Interface Science*, 133 (2007), 61-89 <doi:10.1016/j.cis.2007.04.009>.

[42] Raymundo Arróyave, 'Thermodynamics and Kinetics of Ceramic/Metal Interfacial Interactions' (unpublished Thesis, Massachusetts Institute of Technology, 2004) <http://dspace.mit.edu/handle/1721.1/16625> [accessed 16 July 2010].

[43] K. Landry and N. Eustathopoulos, 'Dynamics of Wetting in Reactive Metal/Ceramic Systems: Linear Spreading', *Acta Materialia*, 44 (1996), 3923-3932 <doi:10.1016/S1359-6454(96)00052-3>.

[44] O. Dezellus and N. Eustathopoulos, 'Fundamental Issues of Reactive Wetting by Liquid Metals', *Journal of Materials Science*, 45 (2010), 4256-4264 <doi:10.1007/s10853-009-4128-x>.

[45] K. Landry, C. Rado and N. Eustathopoulos, 'Influence of Interfacial Reaction Rates on the Wetting Driving Force in Metal/Ceramic Systems', *Metallurgical and Materials Transactions A*, 27 (1996), 3181-3816.

[46] L. Espie, B. Drevet and N. Eustathopoulos, 'Experimental Study of the Influence of Interfacial Energies and Reactivity on Wetting in Metal/Oxide Systems', *Metallurgical and Materials Transactions A*, 25 (1994), 599-605 <doi:10.1007/BF02651601>.

[47] K. Landry, C. Rado and N. Eustathopoulos, 3181-3816.

[48] F. Valenza, M.L. Muolo and A. Passerone, 'Wetting and Interactions of Ni- and Co-Based Superalloys with Different Ceramic Materials', *Journal of Materials Science*, 45 (2009), 2071-2079 <doi:10.1007/s10853-009-3801-4>.

[49] Stephen J. Skinner and John A. Kilner, 'Oxygen Ion Conductors', *Materials Today*, 6 (2003), 30-37 <doi:10.1016/S1369-7021(03)00332-8>.

[50] C. J. Smithells, W. F. Gale and T. C. Totemeier, *Smithells Metals Reference Book* (Butterworth-Heinemann, 2004).

[51] C. J. Smithells, W. F. Gale and T. C. Totemeier.

---

[52] L. B. Borovkova, E.S. Lukin, D. N. Poluboyarinov, N. N. Snegireva, ‘Sintering and Some Properties of Yttrium Oxide Obtained by Decomposing the Carbonate and Hydroxide of Yttrium’, *Refractories*, 12 (1971), 780-785 <doi:10.1007/BF01285627>.

[53] ‘Radon Transform -- from Wolfram MathWorld’, 2010 <http://mathworld.wolfram.com/RadonTransform.html> [accessed 23 September 2010].

[54] L. Farber, G. Tardos and J. N. Michaels, ‘Use of X-Ray Tomography to Study the Porosity and Morphology of Granules’, *Powder Technology*, 132 (2003), 57-63 <doi:10.1016/S0032-5910(03)00043-3>.

[55] ‘Goodfellow’, 2010 <https://www.goodfellow.com/homees.aspx> [accessed 22 September 2010].

[56] V. Swamy, H. J. Seifert and F. Aldinger, ‘Thermodynamic Properties of Y2O3 Phases and the Yttrium-Oxygen Phase Diagram’, *Journal of Alloys and Compounds*, 269 (1998), 201-207 <doi:10.1016/S0925-8388(98)00245-X>.

[57] M. Trojan, ‘Synthesis of a Blue Zircon Pigment’, *Dyes and Pigments*, 9 (1988), 221-232 <doi:10.1016/0143-7208(88)85012-5>.

[58] V. Swamy, H. J. Seifert and F. Aldinger, ‘Thermodynamic Properties of Y2O3 Phases and the Yttrium-Oxygen Phase Diagram’, *Journal of Alloys and Compounds*, 269 (1998), 201-207 <doi:10.1016/S0925-8388(98)00245-X>

[59] J. S. Moya, R. Moreno and J. Soria, ‘Black Color in Partially Stabilized Zirconia’, *Journal of the American Ceramic Society*, 71 (1988), C479-C480 <doi:10.1111/j.1151-2916.1988.tb07555.x>.

[60] N. Green, ‘Private Correspondance’.

[61] P. Zhou, J. Yu, X. Sun, H. Guan and Z. Hu, ‘Role of Yttrium in the Microstructure and Mechanical Properties of a Boron-Modified Nickel-Based Superalloy’, *Scripta Materialia*, 57 (2007), 643-646 <doi:10.1016/j.scriptamat.2007.06.003>.

[62] Sanjay Mathur, Hao Shen, Rasa Rapalaviciute, Aivaras Kareiva and Nicole Donia, ‘Kinetically Controlled Synthesis of Metastable YAlO3 Through Molecular Level Design’, *Journal of Materials Chemistry*, 14 (2004), 3259-3265.

[63] C. J. Smithells, W. F. Gale and T. C. Totemeier.C. J. Smithells, W. F. Gale and T. C. Totemeier.

[64] Peter W. Atkins and Julio de Paula, *Atkins' Physical Chemistry, 7th Ed.*, Seventh Edition (Oxford University Press, 2002).

[65] Peter W. Atkins and Julio de Paula, *Atkins' Physical Chemistry, 7th Ed.*, Seventh Edition (Oxford University Press, 2002).